Dissertation zur Erlangung des Doktorgrades

der Fakultät für Chemie und Pharmazie

der Ludwig-Maximilians-Universität München

Application of advanced surface patterning techniques to study cellular behavior

Themistoklis Zisis

Aus Cholargos, Griechenland

2022

Dissertation zur Erlangung des Doktorgrades

der Fakultät für Chemie und Pharmazie

der Ludwig-Maximilians-Universität München

Application of advanced surface patterning techniques to study cellular behavior

Themistoklis Zisis

Aus Cholargos, Griechenland

2022

Erklärung

Diese Dissertation wurde im Sinne von §7 der Promotionsordnung vom 28 November 2011 von Herrn Prof. Dr. Stefan Zahler betreut.

Eidesstattliche Versicherung

Diese Dissertation wurde eigenständig und ohne unerlaubte Hilfe erarbeitet.

München, den 31.03.2022

_____

Themistoklis Zisis

Dissertation eingereicht am:	**22.02.2022**
1. Gutachterin/ 1. Gutachter:	**Prof. Dr. Stefan Zahler**
2. Gutachterin/ 2. Gutachter:	**Prof. Dr. Angelika Vollmar**
Mündliche Prüfung am:	**24.03.2022**

To my Grandfather

<u>Σπυρίδων Τιμόθεος Μαρίνης</u>

1927-1998

CONTENTS

ABSTRACT

Surface manipulation for the fabrication of chemical or topographic micro- and nanopatterns, has been central to the evolution of *in vitro* biology research. A high variety of surface patterning methods have been implemented in a wide spectrum of applications, including fundamental cell biology studies, development of diagnostic tools, biosensors and drug delivery systems, as well as implant design. Surface engineering has increased our understanding of cell functions such as cell adhesion and cell-cell interaction mechanics, cell proliferation, cell spreading and migration.

From a plethora of existing surface engineering techniques, we use standard microcontact printing methods followed by click chemistry to study the role of intercellular contacts in collective cancer cell migration. Cell dispersion from a confined area is fundamental in a number of biological processes, including cancer metastasis. To date, a quantitative understanding of the interplay of single cell motility, cell proliferation, and intercellular contacts remains elusive. In particular, the role of E- and N-Cadherin junctions, central components of intercellular contacts, is still controversial. Combining theoretical modeling with *in vitro* observations, we investigate the collective spreading behavior of colonies of human cancer cells (T24). The spreading of these colonies is driven by stochastic single-cell migration with frequent transient cell-cell contacts. We find that inhibition of E- and N-Cadherin junctions decreases colony spreading and average spreading velocities, without affecting the strength of correlations in spreading velocities of neighboring cells. Based on a biophysical simulation model for cell migration, we show that the behavioral changes upon disruption of these junctions can be explained by reduced repulsive excluded volume interactions between cells. This suggests that in cancer cell migration, cadherin-based intercellular contacts sharpen cell boundaries leading to repulsive rather than cohesive interactions between cells, thereby promoting efficient cell spreading during collective migration.

Despite the remarkable progress in surface engineering technology and its applications, a combination of pattern properties such as stability, precision, specificity, high-throughput outcome and spatiotemporal control is highly desirable but challenging to achieve. Here, we introduce a versatile and high-throughput covalent photo-immobilization technique, comprising a light-dose dependent patterning step and a subsequent functionalization of the pattern via click chemistry. This two-step process is feasible on arbitrary surfaces and allows for generation of sustainable patterns and gradients. The method is validated in different biological systems by patterning adhesive ligands on cell repellent surfaces, thereby constraining the growth and migration of cells to the designated areas. We then implement a sequential photopatterning approach by adding a second switchable pattering step, allowing for spatiotemporal control over two distinct surface patterns. As a proof of concept, we reconstruct the dynamics of the tip/stalk cell switch during angiogenesis. Our results show that the spatiotemporal control provided by our “sequential photopatterning” system is essential for mimicking dynamic biological processes, and that our innovative approach has a great potential for further applications in cell science.

In summary, this work introduces two novel and versatile paradigms of surface patterning for studying different aspects of cell behaviour in different cell types. The reliability of both setups is experimentally confirmed, providing new insight into the role of cell-cell contacts during collective cancer cell migration as well as the tip/stalk switch behaviour during angiogenesis.

CHAPTER 1

General Introduction

Manipulation of surfaces to acquire control over cellular processes has been a cornerstone for studying cell functions in health and disease [1]. Surface engineering for the production of micro- and nanopatterns using chemical or topographic cues has been implemented in a wide range of applications, from fundamental cell biology research, generation of cell-based biosensors and diagnostic microarrays to drug delivery systems, tissue engineering and

implant design [2]. Studying the response of the cells upon interaction with substrate surfaces dates back to 1912, when cell shape and migratory behaviour was found to be dependent on substrate (in that case spider web) morphology and topography [3].

Topographical patterning involves the fabrication of micro- or nanostructures (such as ridges or pores) on a surface for cell-surface interaction [4]. Chemical patterning on the other hand is defined as the distribution of biomolecules on a surface to create micro- or nanoscale motifs for cell adhesion [5]. Both types of surface patterning have been used to study cell adhesion, cell morphology, intercellular communication, collective or individual cell migration, cell proliferation, cell differentiation, gene expression and apoptosis [1]. In the following paragraphs I will describe the existing patterning techniques and their most important applications.

1.1 Topographical Patterning

Topographical patterning refers to the textural manipulation of surfaces that can be used for mimicking various extracellular microenvironments, which are not smooth but rather textured. Topographical patterning is independent of the use of biomolecules, in contrast to chemical patterning which requires cell-adhesive molecules to regulate cell adsorption on surfaces of desired geometries. Topographical patterning is usually classified in two categories, according to the presence or absence of directional order: anisotropic and isotropic, respectively. Anisotropic patterning refers to the generation of directional structures such as ridges or grooves on a surface (example in Fig. 1 A). Cell adhesion on anisotropic topographical patterns is known to induce changes in cell-shape [6] and cytoskeletal orientation [7], focal adhesion and cell alignment [8]. Isotropic patterning involves architectures without directional order, such as rings, pits, pillars or pores (example in Fig. 1 B). Cell responses to isotropic patterns are less consistent and depend on the size of the pattern and the cell type. In case of fibroblasts, their proliferation increased on the patterned surface compared to a planar control [9]. On the other hand, Curtis et al., reported decreased human fibroblast adhesion on

the patterned surface than on control surfaces [10]. Progenitor cells also showed higher proliferation on the patterned surface compared to control [11] while macrophages exhibited a reduced spreading on the patterned surface compared to control [12]. In experiments involving endothelial cells, the onset of endothelial spreading and cell polarization was 40% faster on surfaces with gratings (grooves of 1 mm-width and 1mm-depth) compared to flat surfaces [13]. The presence of pores, of micrometer [14] or nanometer-scale size [15, 16] on a substrate surface can significantly increase cell adhesion and proliferation. Surface roughness on submicron scale has also differential effects on cell adhesion, morphology and growth. For osteoblast-like MG63 cells, it was shown that their numbers were lower on a surface with submicron-scale roughness compared to flat surfaces [17]. On the contrary, cell attachment/detachment and proliferation of human bone marrow cells were enhanced as the roughness of the substrate surface increased [18]. Finally, substrate mechanical properties (elasticity, hardness) affect cell adhesion and morphology or activity. For example, adhesion of mesenchymal stem cells [19] and NIH3T3 fibroblasts [20] is enhanced with the use of harder matrices.

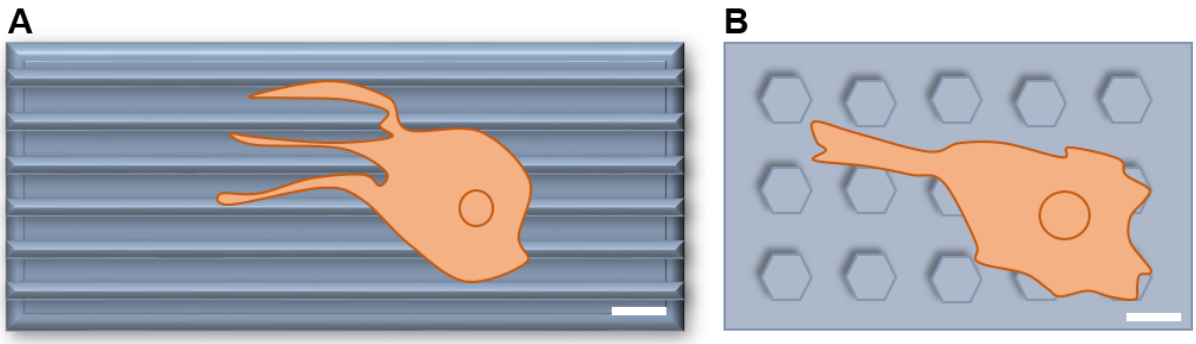

Figure 1: Schematic illustration of topographical patterns. A) Example anisotropic pattern consisting of grooves. B) Example isotropic pattern consisting of hexagonal pillars. Scale bars: 10 μm.

1.2 Chemical Patterning

Chemical Patterning refers to the production of motifs on a substrate that display a chemical contrast and are formed by a chemical reaction [21]. Chemical patterning has been extensively used to study cell adhesion and its effects on different cell functions and behaviors. It is known

since 1964 that cell-substrate interactions occur at small (100 Å) adhesion sites whereas most of the cell surface remains further away from the substrate [22]. It was then reported that generating hydroxyl groups on a polymer-coated surface increased cell attachment, underscoring the necessity of specific chemical groups being available on the substrate [23]. This is due to interactions with certain proteins on the cell surface called Cell Adhesion Molecules (CAMs), which belong to immunoglobulin- or integrin (receptor)- families, selectins and cadherins [24].

The extracellular matrix (ECM) is a key component in chemical patterning applications for studying cell adhesion. ECM comprises the chemical and physical microenvironment, where cells anchor or receive guidance cues. Integrins on the cell surface adhere to ECM components and influence the cytoskeletal organization [25, 26]. Some of the extracellular ligands for cell adhesion are fibronectin, vitronectin and different collagen types [27]. Thus, for cell adhesion experiments the printing of the aforementioned ECM proteins on glass [28] or polystyrene [29] surfaces as well as flexible polymeric surfaces [30, 31] has been implemented.

For the development of 2D surfaces that mimic certain aspects of the cellular microenvironment, the combination of bio-adhesive and non-bio-adhesive properties has been extremely valuable (schematic representation in Fig. 2). Various surface functionalization methods exist to enable this combination, allowing the adhesion of biomolecules in a tailored manner [32, 33]. Combining the above-mentioned topographical and chemical modification techniques, multi-functional surfaces with cell adhesive and non-adhesive chemical contrasts and distinct topographic features can be generated, to target and restrict the cell-surface interaction to the region of a desired motif/structure, leaving the background cell free. Such synthetic biological setups can enhance our understanding of the complex behaviors that characterize biological systems [5, 34-37].

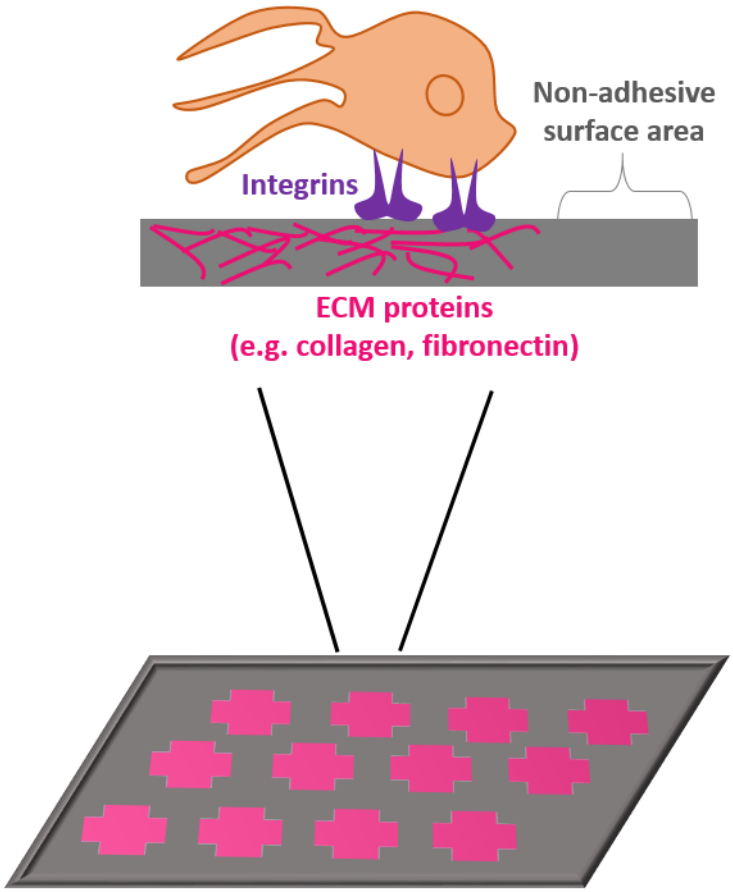

Figure 2: Schematic representation of a non-adhesive surface that has been modified to contain cell-adhesive areas (pink crosses in the picture, with ECM proteins printed on the surface). Cells adhere to the surface via integrins (purple), which bind to the ECM ligands.

1.3 'Bottom-up' vs 'Top-down' approaches for surface fabrication

Surface fabrication methods are often classified according to their directionality from smaller to larger scale and vice versa as bottom-up vs top-down techniques, respectively [34]. While bottom-up methods begin with individual components such as atoms, molecules and colloids that can self-assemble to generate micro or nanostructures on surfaces, top-down methods start out with a bulk material, which after special processing is transformed to acquire micro or nanoscale elements.

A bottom-up approach that has proven to be very useful in this field is the self-assembled monolayers (SAMs). SAMs are spontaneous assemblies of molecules formed upon adsorption of a solution or gas phase to a surface [38]. For example, SAMs are formed upon the adsorption of alkanethiols to gold surfaces or alkylsilanes to hydroxylated surfaces generating an organic interface (variety of functional groups such as carboxylic acid, hydroxyl and amine groups) for adsorption of a broad spectrum of proteins or peptides and adhesion of cells [39-41]. SAMs with cell repellent properties are also widely used, such as Poly (ethylene glycol) or PEG -thiol and PEG-silane SAMs [42, 43]. Furthermore, the term 'polymer brushes' refers to surface-confined macromolecular structures, consisting of polymer chains, usually formed via covalent attachment or physisorption [44]. The 3D morphology of polymer brushes is suitable for binding multiple protein monolayers, making them excellent candidates for protein immobilization studies [45, 46]. Polymer brushes have been implemented to generate surfaces with switchable cell adhesiveness. For instance, thermosensitive polyisopropylacrylamide (PNIPAM) brushes are cell-adhesive above a critical temperature and non-adhesive below it [47, 48]. Another self-assembling-based technique is the 'Layer by Layer' (LbL) deposition method, that implements the alternate adsorption of self-assembling poly-electrolytes on a surface to generate the so-called polyelectrolyte multilayer (PEM) films [49, 50]. PEM films are able to adhere large numbers of biomolecules while preserving their activity and their preparation is possible under aqueous environment and mild conditions, providing high stability. Therefore, the LbL assembly method (e.g. hyaluronic acid/chitosan polyelectrolyte multilayers) has been widely used for regulating the adhesion behavior of various cell types [51], also in combination with click-chemistry principles [52, 53].

Another popular surface functionalization method is plasma polymerization, where ionization of the precursor molecule by high-energy electrons and UV leads to the production of reactive species that bond together and deposit on the substrate, forming a coating on its surface [54]. Furthermore, spin coating is a more high-throughput technique for the deposition of large-sized polymer films on surfaces and is based on 4 sequential processes: deposition, rotation,

rotation, and evaporation [55]. Spin coating is commonly used for the preparation of micro or nanoscale organic photosensitive films, implemented in cell culture studies [56]. A different 'bottom up' fabrication technique is 'colloidal lithography' which is based on the assembly of micro and nanometer sized colloidal particles. Implementing colloidal patterns as masks, various topographical or geometrical features can be generated. One way to achieve this is by reactive ion etching (RIE) on colloidal surfaces [57, 58]. Another method involves the deposition of the material of interest on the substrate surface through the gaps formed between the colloidal particles via evaporation [59, 60]. A more novel version called 'shadow nanosphere lithography' relies on manipulating the position/ angle of the substrate surface relatively to the source of evaporation [61, 62] to produce various structures (e.g. nanometer-sized rods, wires, rings and dots). Finally, Block Copolymers Lithography (BCPL) refers to the use of different block-copolymers to generate regions of contrast on a substrate. This method is based on the differential solubilities of the blocks: the more soluble block envelops the less soluble block and with the use of certain solvents the more soluble block is removed, allowing the second polymer to form a pattern on the surface [63, 64].

'Top down' approaches have also been used for a long time in surface fabrication. Some of the most popular methods are photolithography and soft lithography. Moreover, scanning beam lithography methods have evolved, including electron beam lithography (EBL) [65, 66], Focused Ion Beam Lithography (FIBL) [67] and Transmission Electron Beam Ablation Lithography (TEBAL) [68]. Moreover, Extreme ultraviolet (EUV) [69] and X-ray Lithography (XRL) [70] and Nanoimprint Lithography [71] have been used to introduce micro or nanoscale architectures on surfaces for studying cell adhesion among other biological processes. Another category of scanning lithography is the Scanning Probe Lithography (SPL) [72], including techniques such as Dip Pen Nanolithography or Chemical Nanolithography [73-76]. A more recent development for topographic patterning with very high resolution is the Femtosecond Laser Texturing [77], with several applications for studying cell behavior upon surface adhesion [78]. Finally, ink-jet technology deriving from the printing industry is another

method for structuring of surfaces with high applicability in life sciences [79-81]. The aforementioned top-down patterning techniques will be further described in the paragraph 1.5.

Furthermore, several ‘top down’ and ‘bottom up’ methods have been combined for surface patterning [5]. In addition, patterning approaches are also classified as parallel or serial methods. In parallel methods (for example soft lithography, colloidal lithography) large areas can be patterned by one fabrication process. In contrast, serial techniques (e.g. EBL or FIBL) entail the performance of step-by-step processes, which reduce the writing speed [82]. Unfortunately, there is a trade-off between pattern resolution and writing speed as high-resolution techniques are usually accompanied by low writing speeds.

1.4 Top-down patterning methods for studying biological systems

1.4.1 Soft Lithography and microcontact printing

Soft lithography employs polymers (most commonly polydimethylsiloxane-PDMS) as templates to produce micropatterned substrates from a wide range of materials [83]. Microcontact printing is a type of soft lithography, based on the simple stamping principle, where a solution of cell-adhesive molecules or proteins is used instead of an ink, in order to enable the adsorption of cells or proteins on a substrate surface in a geometrically defined manner [84]. First, an elastomeric (PDMS) stamp with the pattern of interest is fabricated using soft lithography. After inking the stamp with the material solution, the deposition of the material takes place by pressing the stamp on the surface of the substrate, resulting in the pattern of interest (schematic representation in Fig. 3).

As the use of PDMS in microcontact printing has its disadvantages (mainly low polarity and low mechanical stability), alternative polymers have been implemented. Some of the PDMS alternatives are: Poly(ether-block-ester) or PEE which due to its thermoplastic properties reduces oligomer/monomer contamination of substrates during the printing process;

commercial block copolymers as stamp materials for various applications. The same group used poly(styrene-block-butadiene-block-styrene) or SBS- Kraton D1102 and poly(styrene-block-ethylene-co-butylene-blockstyrene) or SEBS-Kraton G1652 which provide higher mechanical strength, allowing the printing of more demanding aspect ratio patterns that are not achievable with PDMS stamps [85]. Polyolefin plastomers (POP) stamps [86] and photocurable poly(urethane acrylate) [87] have also been used for printing proteins on substrate surfaces, yielding patterns of higher quality and resolution than PDMS stamps. Moreover, a hydrophilic and photocurable polymer produced by mixing poly(ethylene glycol) diacrylate or PEGDA and the (NOA) 63 adhesive was found to provide highly tunable mechanical flexibility and bio-compatibility [88]. A plethora of hydrogel stamps have also been successfully used as substitutes for PDMS stamps (nicely reviewed by Kaufmann et al. [83]) including synthetic polymers or natural ones, such as agarose with the latter showing a favorable interaction with the proteins to be printed [89].

Microcontact printing has been widely implemented for generating micropatterned surfaces of cell adhesive biomolecules such as fibronectin [90], or the tripeptide Arg-Gly-Asp (RGD) that is present in fibronectin, laminine, and collagen [91]. Besides RGD, which is the most commonly used cell adhesive peptide, multiple other peptides are known to have cell adhesive properties. These include IKVAV, IKLLI, LGTIPG, LRE, LRGDN, PDGSR, and YIGSR found in laminine [92], DGEA found in collagen I [93], as well as KQAGDV, REDV and PHSRN found in fibronectin [93, 94]. This leads to the development of clusters where cell growth is restricted to cell adhesive islands, enabling the in vitro culture of geometrically organized cell colonies [95]. Besides patterning of cell-adhesive molecules for cell attachment, soft lithography has been used for DNA patterning, in high-throughput production of DNA microarrays [96].

Although the generation of high aspect ratio patterns is challenging with this technique, a general advantage of microcontact printing is its applicability for large areas as well as the ability to make a high-copy number of patterns with repeatedly using a same stamp [1].

Compared to standard photolithography techniques, microcontact printing has the benefit of being less expensive and being suitable for non-planar surfaces, due to PDMS flexibility [97].

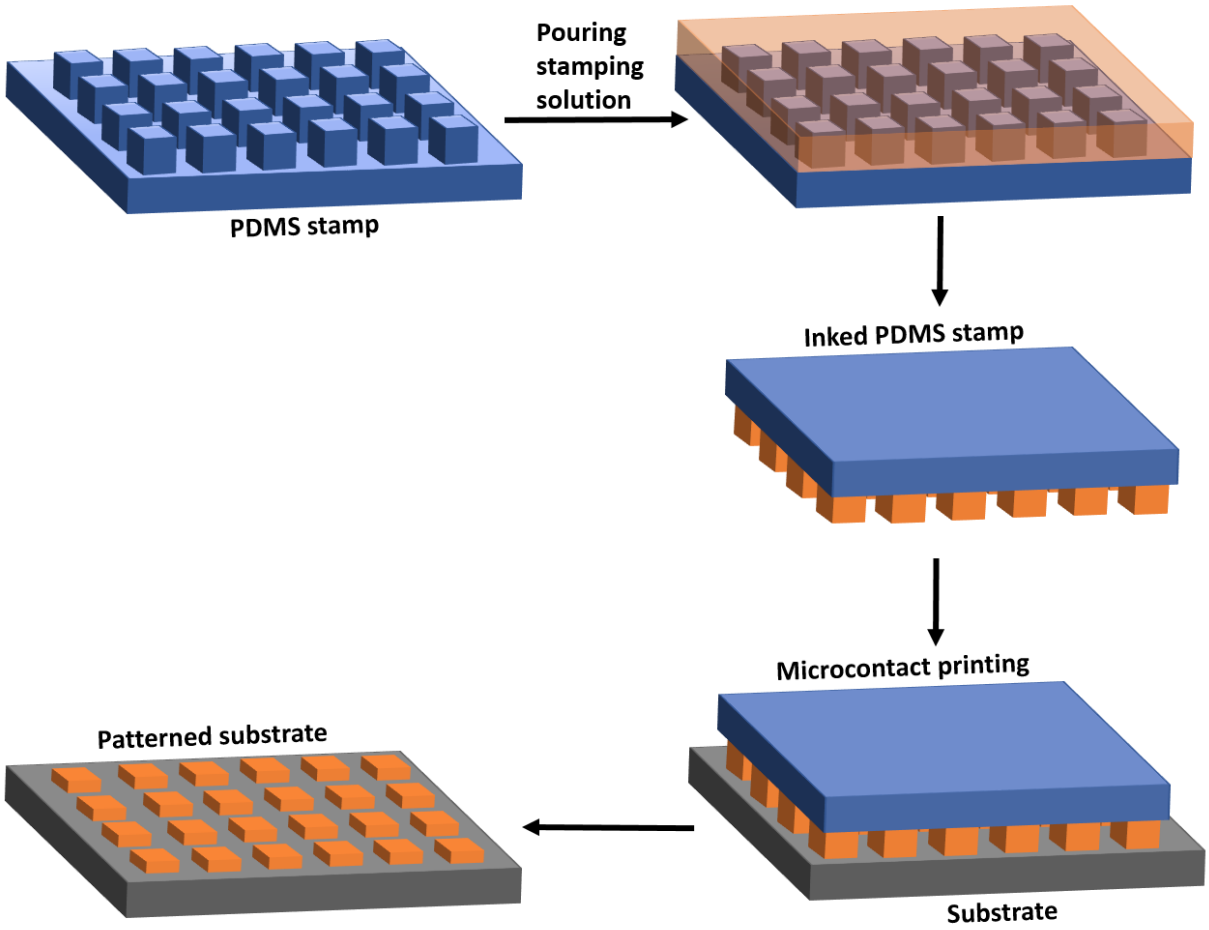

Figure 3: Schematic illustration of the key steps for the generation of micropatterned surfaces with microcontact printing.

1.4.2 Nanoimprint lithography

This is an alternative lithography method first described by Chou et al., in 1995 [71]. It involves two steps: First, the compression molding and then the pattern transfer. During the first step, a nanostructured mold is pressed into a thin resist layer that has been spin coated onto a substrate. When heated above a certain degree, the resist layer becomes deformed (a process also known as hot embossing). Upon cooling down the resist, the mold can be removed and using a reactive ion etching step the resist residues in the compressed areas

can be cleared away [98]. NIL provides a low-cost and high-throughput nanopatterning technology with high applicability in the biomedical field. For example, surfaces patterned using NIL have been implemented to investigate how topographic or chemical nanostructures affect cell-surface interactions [99, 100]. Moreover, the ability to produce a high number of identical nanostructured elements allows the possibility to generate nanoarrays for biosensing [101].

1.4.3 Photolithography

This method uses a resin-coated photomask containing a desired pattern in chrome and transfers this pattern on a photosensitive layer (photoresist) via UV exposure. The photoresist consists of organic compounds in a solvent solution. There are two types of resists: positive resists, where UV-exposed regions become soluble in the developer solution and negative resists where the UV-exposure leads to stabilization or cross-linking of the materials, which become insoluble. In the development step, the soluble parts of the resist are washed away. Therefore, for positive resists the exposed resist is dissolved while the unexposed resist stays on the underlying layer substrate (most commonly silicon wafer). In case of negative resists, the unexposed resist is dissolved while the exposed resist stays on the wafer. As a next step, also known as hardbake, the pattern is transferred from the photoresist into the wafer [102]. A schematic illustration of the photolithography process is provided in Fig. 4. This method has been used, with certain modifications, to produce (cell adhesive) protein micropatterns [34, 103]. A popular adaptation of this method involves photobleaching [104-106], In this case, a microscope plays the role of the mask, projecting the illumination micropattern on the surface. One advantage of using a microscope is that it allows the generation of more complex micropatterned structures containing multiple proteins, as the micropatterned protein can be visualized by imaging and then the subsequent illumination micropattern can be aligned with it, with high accuracy [107]. More recent approaches have adapted photolithographic or photobleaching processes to produce multiplexed microdomains comprised of different

molecules [108, 109], and to enhance the patterning resolution from the micrometer to the sub-micrometer scale [110].

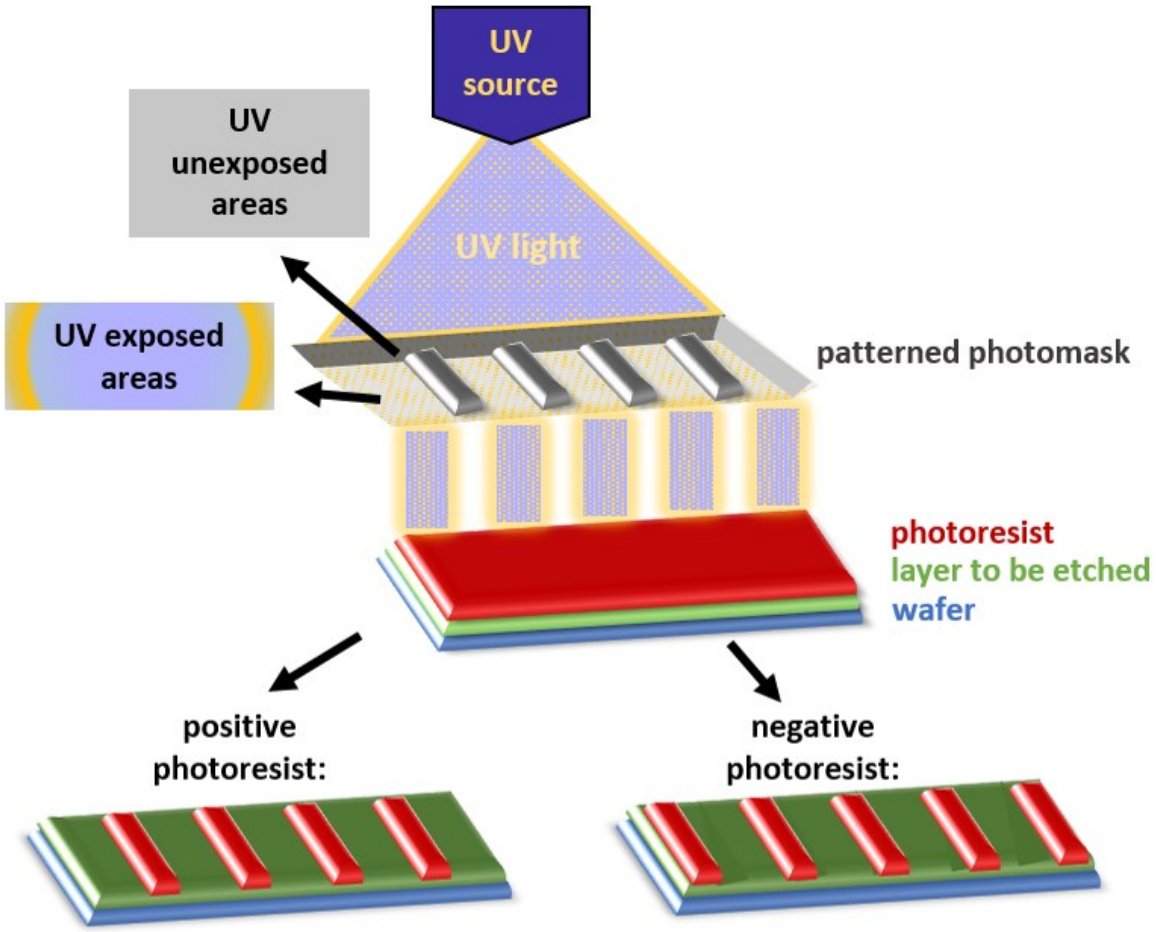

Figure 4: Schematic illustration of the key steps for the production of micropatterned substrates using photolithography. In case of positive resists, the UV-exposed regions become soluble in the developer solution while for negative resists the UV-exposure leads to stabilization or cross-linking of the materials, which become insoluble.

1.4.4 Electron Beam Lithography, Transmission Electron Beam Ablation Lithography and Focused Ion Beam Lithography

Electron beam lithography (EBL) enables the fabrication of very small-scale patterns (dimensions as low as 3 nm) [111]. EBL has a lot of similarities with photolithography, using

exposure and a resist to generate the desired pattern on a substrate. In contrast to photolithography, EBL does not need a mask and uses electron-sensitive instead of light-sensitive resists (usually a polymer coat that gets degraded or crosslinked upon electron exposure, as illustrated in Fig. 5 A). The method requires an electron source and a scanning electron microscope and involves the acceleration of electrons to form an electron beam that is focused on a narrow spot (2-5 nm) through electrostatic lenses. Deflection coils are implemented to control the position of the electron beam on the surface, enabling the raster scanning of the surface. EBL allows for sub-micron pattern production because the wavelength of the electrons is much shorter compared to UV light. While photolithography can use one exposure for a whole wafer, EBL needs multiple exposures and is therefore more time-consuming. Another key difference between the two processes is that EBL requires conducting substrates (for example silicon) or a metallic layer to cover non-conducting substrates [112].

Following EBL, Transmission Electron Beam Ablation Lithography (TEBAL) [68] has been developed as an attempt to achieve even higher resolutions. TEBAL involves controllably ablating evaporated metal films, which are prepared using e-beam lithography on silicon nitride membrane substrates, to generate various nano-geometries such as lines, circles, channels and holes [68].

Furthermore, quite similarly to EBL, Focused Ion Beam Lithography (FIBL) uses a focused beam of ions to scan across a substrate surface in a patterned manner with sub-10nm resolution [113] (schematic illustration in Fig. 5 B). Because of the higher mass of the ions compared to the electrons, the higher energy of the ion beam reduces the required exposure time for the resists (increased resist sensitivity), leading to higher processing speeds. FIBL has the extra advantage over EBL of avoiding electron backscattering and thus, the pixel size is approximately equal to the beam spot size, without between-pixel exposure. Hence, due to lower scattering and reduced lateral diffusion of secondary electrons, FIBL achieves higher resolutions than EBL even with same sizes of beam spot.

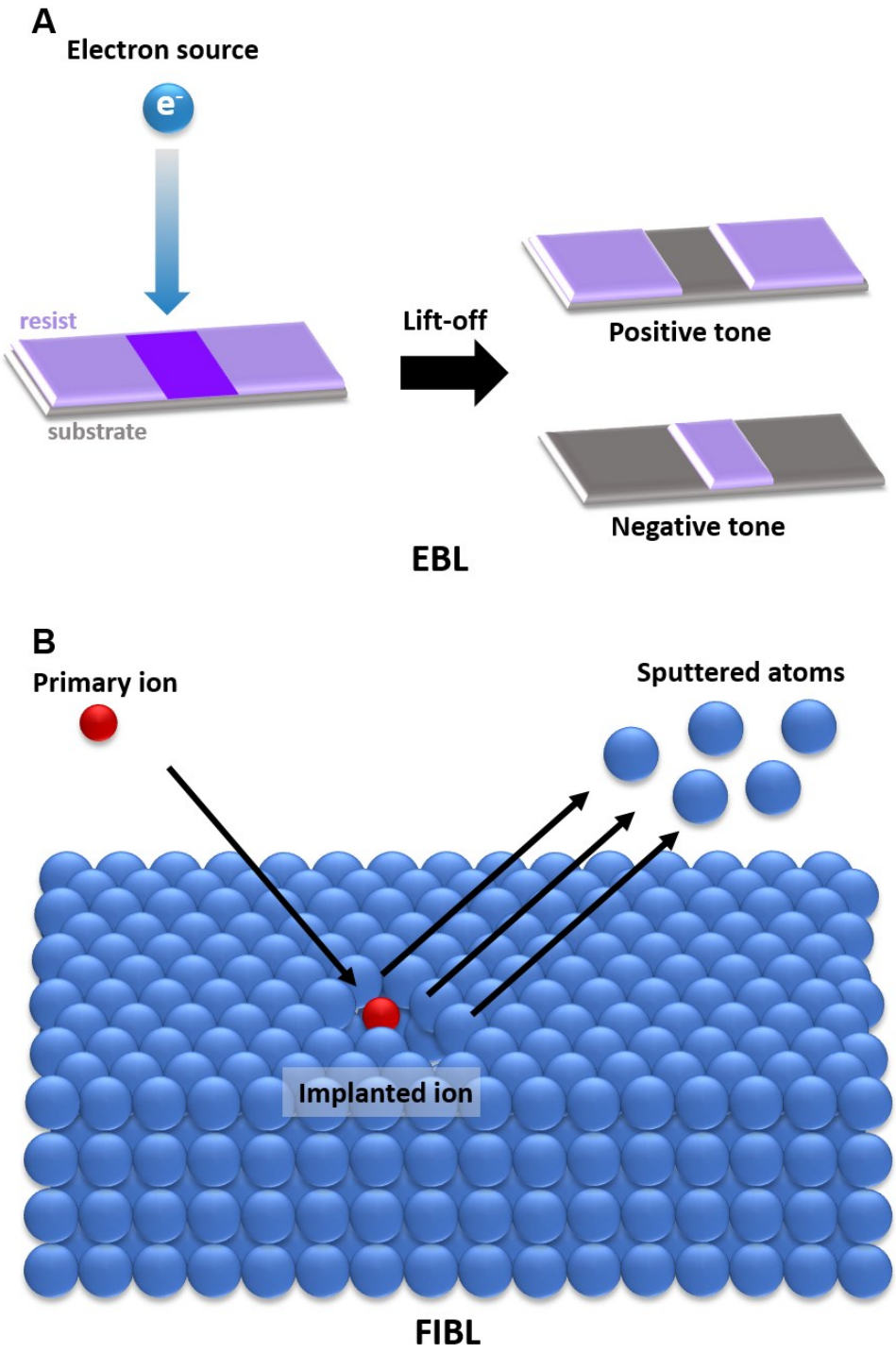

Figure 5: Schematic representation of the EBL process (A) and FIBL principle of function (B).

1.4.5 Extreme ultraviolet (EUV) and X-ray Lithography (XRL)

Extreme ultraviolet (EUV) irradiation is another lithographic method, based on the high energy/low-wavelength photons (124 to 10 nm). Photons in such energy spectrum can eradicate multiple bonds from polymer materials, and thereby introduce micro- or nanostructures [69]. Due to the EUV photons' restricted penetration depth, they can modify polymer surfaces without changing the properties of the substrate material in terms of volume. EUV irradiation is frequently implemented for improving the roughness of a polymer surface (for example polytetrafluoroethylene or PTFE), as the mean surface roughness of the polymer increases 4 times upon EUV irradiation, enhancing its hydrophobicity and subsequent cell adhesion efficiency [114].

X-ray lithography uses X-rays instead of high energy photons, and a substrate with a conductive electroplating seed layer, coated with a photoresist [70]. The coated substrate is exposed to X-rays using a mask with the pattern of interest [115]. X-ray lithography followed by electroplating is considered an optimal choice for creating microstructures with high height to width ratio [116, 117] .

1.4.6 Dip Pen Nanolithography and Chemical Nanolithography

Dip pen nanolithography is a direct-writing lithographic method that provides a sub-100nm-scale patterning resolution. It is a scanning-probe based method that modifies a substrate surface in a localized manner by oxidation or by directly transferring the material of interest [74, 118]. This is achieved by dipping an atomic force microscope (AFM) tip in a solution containing the material (for example alkanethiols) and then allowing the inked AFM tip to transfer the material molecules to the areas of the surface that it passes above, similarly to traditional writing with pen and ink on paper [119]. The molecule transfer from the tip to the surface usually relies on the the chemical gradient generated between the AFM tip and the substrate (capillary transport) [101] or heat-induced chemical reactivity between the ink material and the surface (thermochemical nanolithography) [120]. Dip pen nanolithography

has been extensively used in the production of nanoscale patterns with applications in the biomedical research [75]. A strong advantage of Dip pen nanolithography is that practically any design of nanostructure can be fabricated, as it is a writing-based technique. However, a disadvantage of Dip pen nanolithography is that it's a serial method, making it much slower and hindering potential high-throughput applications [101]. Therefore, this technique is selected when the cost and speed of the process is less important than the resolution and specificity of the nanostructure of interest (for example generation of long-term usable masters or masks). On the other hand, there are several adaptations of the Dip pen nanolithography, often referred to as Multiple Ink Nanolithography, that allow the production of monolayers of different organic molecules with a separation of 5 nm [121]. For example, the successful implementation of an eight-pen nano-plotter that performs parallel dip pen nanolithography has been reported [122]. Moreover, further adaptation of the aforementioned method that uses multiple AFM tips and inks composed of organic adsorbates exhibited 12 nm width resolution, multiple pattern alignment, and a potential for high speed parallel writing (thus called massively-parallel dip pen nanolithography).

1.4.7 Femtosecond laser texturing

Femtosecond laser texturing is a widely used strategy for surface functionalization. It involves direct laser writing with femtosecond (fs) laser pulses and allows the generation of patterns with high reproducibility without the requirement of a clean room [123]. Laser texturing enables in a single step the controlled multi-scaled design on metallic surfaces, such as titanium-6aluminum-4vanadium plates [124] that are often used in graft transplantation [125]. The resulting laser-induced nanostructures can modify surface properties such as roughness and wettability, to enhance cell adhesion and control cell spreading. Therefore, this technique is highly applicable in implant bio-engineering, for example in dental and orthopaedic implants [124]. Moreover, fs laser texturing has been used to construct high-resolution patterns on soft polymer (PET, PTT and polycarbonate bisphenol) films or Polylactic acid (PLA) construct to allow cell adhesion and cell culture [16, 126]. Another important application of fs laser

processing was the fabrication of patterns of thin films of chitosan or chitosan/ZrO2 combination for obtaining efficient platforms for bone tissue repair with high stability and mechanical strength but also high biocompatibility, biodegradability, and protein affinity [127].

1.4.8 Ink-jet technology

Another method for surface fabrication that has been inspired by the printing industry is the ink-jet technology, which has multiple applications in life sciences from genomics and chemistry, to high-throughput drug screening [79] and tissue engineering by seeding living cells in geometries similar to biological microenvironments [80]. This technology is capable of achieving high resolutions (~ 1 μm) by ejecting extremely small-sized ink drops in a parallel fashion [81].

1.5 Concluding remarks

Surface fabrication for the spatially-controlled adhesion of cells, cellular components or proteins can be achieved using a wide spectrum of techniques. Such techniques can introduce different topographies or chemical contrasts on a great variety of substrate surfaces, from (bio)polymer films to ceramic or metallic surfaces. Although serial patterning methods allow for higher pattern resolution, parallel patterning methods are faster, less expensive and suitable for high-throughput biomedical applications. The spatial control of cell adhesion that is provided by such techniques is extremely valuable. However, in order to study dynamic cell behaviour, it is important to gain temporal control of the surface properties. In other words, being able to render a surface cell reactive or non-reactive at a wished time-point during an experiment is crucial for *in vitro* research. In the first part of this study (Chapter 2), standard microcontact printing processes were implemented for studying the role of intercellular contacts in the collective spreading behaviour of human cancer cell (T24) colonies. In the second part of my study (Chapter 3), multiple surface engineering approaches were used, including standard microcontact printing, a novel covalent (building block-based)

photolithography process and a further adaptation of this photolithographic process that provides spatio-temporal control over the surface adhesive properties and the subsequent cell migratory behaviour.

1.6 Aims and outline of the study

The general aim of this study is adapting existing surface engineering methods to generate patterned surfaces for studying various aspects of cell behaviour, where the pattern properties are adjustable, according to the experimental requirements. More specifically, the aim of the first part of the study (Chapter 2) is to use a surface fabrication- based approach to investigate the collective spreading dynamics of urothelial bladder carcinoma T24 cell clusters upon disruption of Cadherin junctions. We combine the resulting experimental observations with quantitative biophysical predictions to show how disrupting Cadherin junctions affects cellular interactions and the cell spreading efficiency in the colony.

The aim of the second part of this study (Chapter 3), is to initially establish a covalent single photopatterning technique that provides high stability and versatility as it can be used with a variety of different illumination setups and photo-chemistries tailored to the specific biological set-up needed. The specificity and efficacy of this photopatterning system is assessed by generating concentration gradients to investigate haptotactic cell migration using different cell lines. The next goal is becoming able to ‘’switch on’’ distinct areas at any selected timepoint. For that purpose, another photopatterning step is included and the efficacy of this sequential photopatterning setup in inducing a tip/stalk phenotype switch in migrating endothelial cells is evaluated.

1.7 References

1. Ermis, M., E. Antmen, and V. Hasirci, *Micro and Nanofabrication methods to control cell-substrate interactions and cell behavior: A review from the tissue engineering perspective.* Bioactive Materials, 2018. **3**(3): p. 355-369.

2. *Cell Sensing and Response to Micro- and Nanostructured Surfaces Produced by Chemical and Topographic Patterning.* Tissue Engineering, 2007. **13**(8): p. 1879-1891.
3. Harrison, R.G., *The cultivation of tissues in extraneous media as a method of morpho-genetic study.* The Anatomical Record, 1912. **6**(4): p. 181-193.
4. Sevcik, E.N., et al., *Patterning on Topography for Generation of Cell Culture Substrates with Independent Nanoscale Control of Chemical and Topographical Extracellular Matrix Cues.* Current protocols in cell biology, 2017. **75**: p. 10.23.1-10.23.25.
5. Ogaki, R., M. Alexander, and P. Kingshott, *Chemical patterning in biointerface science.* Materials Today, 2010. **13**(4): p. 22-35.
6. Wójciak-Stothard, B., et al., *Role of the cytoskeleton in the reaction of fibroblasts to multiple grooved substrata.* Cell Motil Cytoskeleton, 1995. **31**(2): p. 147-58.
7. Oakley, C. and D.M. Brunette, *The sequence of alignment of microtubules, focal contacts and actin filaments in fibroblasts spreading on smooth and grooved titanium substrata.* J Cell Sci, 1993. **106 (Pt 1)**: p. 343-54.
8. den Braber, E.T., et al., *Orientation of ECM protein deposition, fibroblast cytoskeleton, and attachment complex components on silicone microgrooved surfaces.* J Biomed Mater Res, 1998. **40**(2): p. 291-300.
9. Green, A.M., et al., *Fibroblast response to microtextured silicone surfaces: texture orientation into or out of the surface.* J Biomed Mater Res, 1994. **28**(5): p. 647-53.
10. Curtis, A.S., et al., *Cells react to nanoscale order and symmetry in their surroundings.* IEEE Trans Nanobioscience, 2004. **3**(1): p. 61-5.
11. Mata, A., et al., *Growth of connective tissue progenitor cells on microtextured polydimethylsiloxane surfaces.* J Biomed Mater Res, 2002. **62**(4): p. 499-506.
12. Schmidt, J.A. and A.F. von Recum, *Macrophage response to microtextured silicone.* Biomaterials, 1992. **13**(15): p. 1059-69.
13. Franco, D., et al., *Control of initial endothelial spreading by topographic activation of focal adhesion kinase.* Soft Matter, 2011. **7**(16): p. 7313-7324.
14. Murphy, C.M. and F.J. O'Brien, *Understanding the effect of mean pore size on cell activity in collagen-glycosaminoglycan scaffolds.* Cell adhesion & migration, 2010. **4**(3): p. 377-381.
15. Hatano, K., et al., *Effect of surface roughness on proliferation and alkaline phosphatase expression of rat calvarial cells cultured on polystyrene.* Bone, 1999. **25**(4): p. 439-45.
16. Jeon, H., et al., *Directing cell migration and organization via nanocrater-patterned cell-repellent interfaces.* Nat Mater, 2015. **14**(9): p. 918-23.
17. Zhao, G., et al., *Osteoblast-like cells are sensitive to submicron-scale surface structure.* Clin Oral Implants Res, 2006. **17**(3): p. 258-64.
18. Deligianni, D.D., et al., *Effect of surface roughness of hydroxyapatite on human bone marrow cell adhesion, proliferation, differentiation and detachment strength.* Biomaterials, 2000. **22**(1): p. 87-96.
19. Engler, A.J., et al., *Matrix elasticity directs stem cell lineage specification.* Cell, 2006. **126**(4): p. 677-89.
20. Yeung, T., et al., *Effects of substrate stiffness on cell morphology, cytoskeletal structure, and adhesion.* Cell Motil Cytoskeleton, 2005. **60**(1): p. 24-34.
21. Karthaus, O., *Chemical Patterning on Surfaces and in Bulk Gels*, in *Handbook of Solid State Chemistry*. p. 539-562.
22. Curtis, A.S., *THE MECHANISM OF ADHESION OF CELLS TO GLASS. A STUDY BY INTERFERENCE REFLECTION MICROSCOPY.* The Journal of cell biology, 1964. **20**(2): p. 199-215.
23. Curtis, A.S., et al., *Adhesion of cells to polystyrene surfaces.* J Cell Biol, 1983. **97**(5 Pt 1): p. 1500-6.
24. Edelman, G.M., *Cell Adhesion Molecules.* Science, 1983. **219**(4584): p. 450-457.
25. Isermann, P. and J. Lammerding, *Nuclear Mechanics and Mechanotransduction in Health and Disease.* Current Biology, 2013. **23**(24): p. R1113-R1121.
26. Hutchison, C.J. and H.J. Worman, *A-type lamins: Guardians of the soma?* Nature Cell Biology, 2004. **6**(11): p. 1062-1067.
27. Geiger, B., et al., *Transmembrane crosstalk between the extracellular matrix and the cytoskeleton.* Nature Reviews Molecular Cell Biology, 2001. **2**(11): p. 793-805.
28. Alamdari, O., et al., *Micropatterning of ECM Proteins on Glass Substrates to Regulate Cell Attachment and Proliferation.* Avicenna journal of medical biotechnology, 2013. **5**: p. 234-240.
29. Dånmark, S., et al., *Integrin-mediated adhesion of human mesenchymal stem cells to extracellular matrix proteins adsorbed to polymer surfaces.* Biomed Mater, 2012. **7**(3): p. 035011.
30. McDevitt, T.C., et al., *Spatially organized layers of cardiomyocytes on biodegradable polyurethane films for myocardial repair.* J Biomed Mater Res A, 2003. **66**(3): p. 586-95.

31. Hidalgo-Bastida, L.A., et al., *Cell adhesion and mechanical properties of a flexible scaffold for cardiac tissue engineering.* Acta Biomater, 2007. **3**(4): p. 457-62.
32. Lecuit, T. and P.-F. Lenne, *Cell surface mechanics and the control of cell shape, tissue patterns and morphogenesis.* Nature Reviews Molecular Cell Biology, 2007. **8**(8): p. 633-644.
33. Mrksich, M., *What can surface chemistry do for cell biology?* Current Opinion in Chemical Biology, 2002. **6**(6): p. 794-797.
34. Falconnet, D., et al., *Surface engineering approaches to micropattern surfaces for cell-based assays.* Biomaterials, 2006. **27**(16): p. 3044-63.
35. Robotti, F., et al., *A micron-scale surface topography design reducing cell adhesion to implanted materials.* Scientific Reports, 2018. **8**(1): p. 10887.
36. Szymanski, J.M., Q. Jallerat, and A.W. Feinberg, *ECM protein nanofibers and nanostructures engineered using surface-initiated assembly.* Journal of visualized experiments : JoVE, 2014(86): p. 51176.
37. Sun, Y., et al., *Conformal nanopatterning of extracellular matrix proteins onto topographically complex surfaces.* Nature methods, 2015. **12**(2): p. 134-136.
38. Raynor, J.E., et al., *Polymer brushes and self-assembled monolayers: Versatile platforms to control cell adhesion to biomaterials (Review).* Biointerphases, 2009. **4**(2): p. FA3-FA16.
39. Mrksich, M. and G.M. Whitesides, *Using self-assembled monolayers to understand the interactions of man-made surfaces with proteins and cells.* Annu Rev Biophys Biomol Struct, 1996. **25**: p. 55-78.
40. Arima, Y. and H. Iwata, *Preferential adsorption of cell adhesive proteins from complex media on self-assembled monolayers and its effect on subsequent cell adhesion.* Acta Biomaterialia, 2015. **26**: p. 72-81.
41. Wink, T., et al., *Self-assembled Monolayers for Biosensors.* Analyst, 1997. **122**(4): p. 43R-50R.
42. Banik, B.L., et al., *Chapter 9 - Bio-Instructive Scaffolds for Musculoskeletal Interfaces*, in *Bio-Instructive Scaffolds for Musculoskeletal Tissue Engineering and Regenerative Medicine*, J.L. Brown, S.G. Kumbar, and B.L. Banik, Editors. 2017, Academic Press. p. 203-233.
43. Cerruti, M., et al., *Poly(ethylene glycol) monolayer formation and stability on gold and silicon nitride substrates.* Langmuir, 2008. **24**(19): p. 10646-53.
44. Brittain, W.J. and S. Minko, *A structural definition of polymer brushes.* Journal of Polymer Science Part A: Polymer Chemistry, 2007. **45**(16): p. 3505-3512.
45. Dai, J., G.L. Baker, and M.L. Bruening, *Use of porous membranes modified with polyelectrolyte multilayers as substrates for protein arrays with low nonspecific adsorption.* Anal Chem, 2006. **78**(1): p. 135-40.
46. Bratek-Skicki, A., et al., *Mixed Polymer Brushes for the Selective Capture and Release of Proteins.* Biomacromolecules, 2019. **20**(2): p. 778-789.
47. Liu, X., et al., *Switching water droplet adhesion using responsive polymer brushes.* Langmuir, 2010. **26**(14): p. 12377-82.
48. Halperin, A. and M. Kröger, *Thermoresponsive Cell Culture Substrates Based on PNIPAM Brushes Functionalized with Adhesion Peptides: Theoretical Considerations of Mechanism and Design.* Langmuir, 2012. **28**(48): p. 16623-16637.
49. Decher, M.G. *Fuzzy Nanoassemblies: Toward Layered Polymeric*. 1997.
50. Gribova, V., R. Auzely-Velty, and C. Picart, *Polyelectrolyte Multilayer Assemblies on Materials Surfaces: From Cell Adhesion to Tissue Engineering.* Chem Mater, 2012. **24**(5): p. 854-869.
51. Croll, T.I., et al., *A blank slate? Layer-by-layer deposition of hyaluronic acid and chitosan onto various surfaces.* Biomacromolecules, 2006. **7**(5): p. 1610-22.
52. Kinnane, C.R., et al., *Peptide-Functionalized, Low-Biofouling Click Multilayers for Promoting Cell Adhesion and Growth.* Small, 2009. **5**(4): p. 444-448.
53. Chua, P.H., et al., *Surface functionalization of titanium with hyaluronic acid/chitosan polyelectrolyte multilayers and RGD for promoting osteoblast functions and inhibiting bacterial adhesion.* Biomaterials, 2008. **29**(10): p. 1412-21.
54. Kumar, A., et al., *Plasma Polymerization: Electronics and Biomedical Application*. 2017. p. 593-657.
55. Sahu, N., B. Parija, and S. Panigrahi, *Fundamental understanding and modeling of spin coating process: A review.* Indian Journal of Physics, 2009. **83**(4): p. 493-502.
56. Xu, L. and A. Yamamoto, *Characteristics and cytocompatibility of biodegradable polymer film on magnesium by spin coating.* Colloids Surf B Biointerfaces, 2012. **93**: p. 67-74.
57. Choi, D.-G., et al., *Colloidal Lithographic Nanopatterning via Reactive Ion Etching.* Journal of the American Chemical Society, 2004. **126**(22): p. 7019-7025.

58. Yang, S.M., et al., *Nanomachining by colloidal lithography.* Small, 2006. **2**(4): p. 458-75.
59. Chen, J., et al., *Evaporation-induced assembly of quantum dots into nanorings.* ACS nano, 2009. **3**(1): p. 173-180.
60. Burmeister, F., et al., *Colloid Monolayers as Versatile Lithographic Masks.* Langmuir, 1997. **13**(11): p. 2983-2987.
61. Kosiorek, A., et al., *Shadow Nanosphere Lithography: Simulation and Experiment.* Nano Letters, 2004. **4**(7): p. 1359-1363.
62. Kosiorek, A., et al., *Fabrication of Nanoscale Rings, Dots, and Rods by Combining Shadow Nanosphere Lithography and Annealed Polystyrene Nanosphere Masks.* Small (Weinheim an der Bergstrasse, Germany), 2005. **1**: p. 439-44.
63. Xu, C., Ohno, K., Ladmiral, V., & Composto, R. J. (2008). Dispersion of polymer-grafted magnetic nanoparticles in homopolymers and block copolymers.
64. Glass, R., et al., *Block copolymer micelle nanolithography on non-conductive substrates.* New Journal of Physics, 2004. **6**: p. 101.
65. Craighead, H.G., et al., *10-nm linewidth electron beam lithography on GaAs.* Applied Physics Letters, 1983. **42**(1): p. 38-40.
66. Ito, T. and S. Okazaki, *Pushing the limits of lithography.* Nature, 2000. **406**(6799): p. 1027-31.
67. Romano-Rodriguez, A. and F. Hernandez-Ramirez, *Dual-beam focused ion beam (FIB): A prototyping tool for micro and nanofabrication.* Microelectronic Engineering, 2007. **84**: p. 789-792.
68. Fischbein, M.D. and M. Drndić, *Sub-10 nm Device Fabrication in a Transmission Electron Microscope.* Nano Letters, 2007. **7**(5): p. 1329-1337.
69. Ahad, I., et al., *Extreme Ultraviolet Surface Modification of Polyethylene Terephthalate (PET) for Surface Structuring and Wettability Control.* Acta Physica Polonica A, 2016. **129**: p. 241-243.
70. Smith, H.I. and M.L. Schattenburg, *X-ray lithography from 500 to 30 nm: X-ray nanolithography.* IBM Journal of Research and Development, 1993. **37**(3): p. 319-329.
71. Chou, S.Y., P.R. Krauss, and P.J. Renstrom, *Imprint of sub-25 nm vias and trenches in polymers.* Applied Physics Letters, 1995. **67**(21): p. 3114-3116.
72. Gates, B.D., et al., *UNCONVENTIONAL NANOFABRICATION.* Annual Review of Materials Research, 2004. **34**(1): p. 339-372.
73. Wouters, D.D. and U.S. Schubert, *Nanolithography and nanochemistry: probe-related patterning techniques and chemical modification for nanometer-sized devices.* Angewandte Chemie, 2004. **43 19**: p. 2480-95.
74. Ginger, D.S., H. Zhang, and C.A. Mirkin, *The Evolution of Dip-Pen Nanolithography.* Angewandte Chemie International Edition, 2004. **43**(1): p. 30-45.
75. Salaita, K., Y. Wang, and C.A. Mirkin, *Applications of dip-pen nanolithography.* Nature Nanotechnology, 2007. **2**(3): p. 145-155.
76. Xie, X.N., et al., *Nanoscale materials patterning and engineering by atomic force microscopy nanolithography.* Materials Science and Engineering: R: Reports, 2006. **54**(1): p. 1-48.
77. Okano, K., et al., *In situ patterning and controlling living cells by utilizing femtosecond laser.* Journal of Photochemistry and Photobiology C: Photochemistry Reviews, 2016. **28**: p. 1-28.
78. Jun, I., et al., *Creating Hierarchical Topographies on Fibrous Platforms Using Femtosecond Laser Ablation for Directing Myoblasts Behavior.* ACS Applied Materials & Interfaces, 2016. **8**(5): p. 3407-3417.
79. Lemmo, A.V., D.J. Rose, and T.C. Tisone, *Inkjet dispensing technology: applications in drug discovery.* Current Opinion in Biotechnology, 1998. **9**(6): p. 615-617.
80. Nakamura, M., et al., *Biocompatible inkjet printing technique for designed seeding of individual living cells.* Tissue Eng, 2005. **11**(11-12): p. 1658-66.
81. Park, J.-U., et al., *High-resolution electrohydrodynamic jet printing.* Nature Materials, 2007. **6**(10): p. 782-789.
82. Koch, A.J. and H. Meinhardt, *Biological pattern formation: from basic mechanisms to complex structures.* Reviews of Modern Physics, 1994. **66**(4): p. 1481-1507.
83. Kaufmann, T. and B.J. Ravoo, *Stamps, inks and substrates: polymers in microcontact printing.* Polymer Chemistry, 2010. **1**(4): p. 371-387.
84. Fernandes, T.G., M.M. Diogo, and J.M.S. Cabral, *5 - Microscale technologies for stem cell culture*, in *Stem Cell Bioprocessing*, T.G. Fernandes, M.M. Diogo, and J.M.S. Cabral, Editors. 2013, Woodhead Publishing. p. 143-175.

85. Trimbach, D., et al., *Block Copolymer Thermoplastic Elastomers for Microcontact Printing.* Langmuir, 2003. **19**(26): p. 10957-10961.
86. Csucs, G., et al., *Microcontact Printing of Macromolecules with Submicrometer Resolution by Means of Polyolefin Stamps.* Langmuir, 2003. **19**(15): p. 6104-6109.
87. Yoo, P.J., et al., *Unconventional Patterning with A Modulus-Tunable Mold: From Imprinting to Microcontact Printing.* Chemistry of Materials, 2004. **16**(24): p. 5000-5005.
88. Lee, N.Y., et al., *Hydrophilic Composite Elastomeric Mold for High-Resolution Soft Lithography.* Langmuir, 2006. **22**(21): p. 9018-9022.
89. Mayer, M., et al., *Micropatterned agarose gels for stamping arrays of proteins and gradients of proteins.* PROTEOMICS, 2004. **4**(8): p. 2366-2376.
90. Fitzpatrick, V., et al., *Signal mingle: Micropatterns of BMP-2 and fibronectin on soft biopolymeric films regulate myoblast shape and SMAD signaling.* Scientific Reports, 2017. **7**(1): p. 41479.
91. Wheeldon, I., et al., *Nanoscale tissue engineering: spatial control over cell-materials interactions.* Nanotechnology, 2011. **22**(21): p. 212001-212001.
92. Zhu, J., *Bioactive modification of poly(ethylene glycol) hydrogels for tissue engineering.* Biomaterials, 2010. **31**(17): p. 4639-56.
93. Lauffenburger, D.A. and J.J. Linderman, *Receptors: models for binding, trafficking, and signaling*. 1996: Oxford University Press on Demand.
94. Hynes, R.O. and K.M. Yamada, *Fibronectins: multifunctional modular glycoproteins.* J Cell Biol, 1982. **95**(2 Pt 1): p. 369-77.
95. Peerani, R., et al., *Manipulation of Signaling Thresholds in "Engineered Stem Cell Niches" Identifies Design Criteria for Pluripotent Stem Cell Screens.* PLOS ONE, 2009. **4**(7): p. e6438.
96. Fredonnet, J., et al., *Dynamic PDMS inking for DNA patterning by soft lithography.* Microelectronic Engineering, 2013. **111**: p. 379 - 383.
97. Liu, W.-W., Z.-L. Chen, and X.-Y. Jiang, *Methods for Cell Micropatterning on Two-Dimensional Surfaces and Their Applications in Biology.* Chinese Journal of Analytical Chemistry, 2009. **37**(7): p. 943-949.
98. Zankovych, S., et al., *Nanoimprint lithography: challenges and prospects.* Nanotechnology, 2001. **12**(2): p. 91-95.
99. Yim, E.K., et al., *Nanopattern-induced changes in morphology and motility of smooth muscle cells.* Biomaterials, 2005. **26**(26): p. 5405-13.
100. Dalby, M.J., et al., *Investigating filopodia sensing using arrays of defined nano-pits down to 35 nm diameter in size.* Int J Biochem Cell Biol, 2004. **36**(10): p. 2005-15.
101. Blättler, T., et al., *Nanopatterns with biological functions.* J Nanosci Nanotechnol, 2006. **6**(8): p. 2237-64.
102. Berkowski, K.L., et al., *Introduction to Photolithography: Preparation of Microscale Polymer Silhouettes.* Journal of Chemical Education, 2005. **82**(9): p. 1365.
103. Azioune, A., et al., *Simple and rapid process for single cell micro-patterning.* Lab on a Chip, 2009. **9**(11): p. 1640-1642.
104. Waldbaur, A., et al., *Maskless Projection Lithography for the Fast and Flexible Generation of Grayscale Protein Patterns.* Small, 2012. **8**(10): p. 1570-1578.
105. Bélisle, J.M., J. Mazzaferri, and S. Costantino, *Laser-assisted adsorption by photobleaching.* Methods Cell Biol, 2014. **119**: p. 125-40.
106. Martin, T.A., et al., *Quantitative photochemical immobilization of biomolecules on planar and corrugated substrates: a versatile strategy for creating functional biointerfaces.* ACS applied materials & interfaces, 2011. **3**(9): p. 3762-3771.
107. Bélisle, J.M., et al., *Patterning protein concentration using laser-assisted adsorption by photobleaching, LAPAP.* Lab Chip, 2008. **8**(12): p. 2164-7.
108. Qiao, F., et al., *Photolithography-Mediated Area-Selective Immobilization of Biomolecules on Polydopamine Coating.* Langmuir, 2019. **35**(22): p. 7175-7179.
109. Watson, J.L., et al., *High-efficacy subcellular micropatterning of proteins using fibrinogen anchors.* Journal of Cell Biology, 2021. **220**(2).
110. Wu, C.Y., H. Hsieh, and Y.C. Lee, *Contact Photolithography at Sub-Micrometer Scale Using a Soft Photomask.* Micromachines (Basel), 2019. **10**(8).
111. Vieu, C., et al., *Electron beam lithography: resolution limits and applications.* Applied Surface Science, 2000. **164**: p. 111.
112. McMurray, R., J, M., & Gadegaar, N. , *Nanopatterned Surfaces for Biomedical Applications.* Biomedical Engineering, Trends in Materials Science, 2011.

113. Cabrini, S., et al., *Focused ion beam lithography for two dimensional array structures for photonic applications.* Microelectronic Engineering, 2005. **78-79**: p. 11-15.
114. Cai, S., et al., *Recent advance in surface modification for regulating cell adhesion and behaviors.* Nanotechnology Reviews, 2020. **9**(1): p. 971-989.
115. T. J. Schröter, F.J.K., P. Meyer, D. Kunka, J. Meiser, K. Willer,, et al.
116. Becker, E.W., et al., *Fabrication of microstructures with high aspect ratios and great structural heights by synchrotron radiation lithography, galvanoforming, and plastic moulding (LIGA process).* Microelectronic Engineering, 1986. **4**(1): p. 35-56.
117. Reznikova, E., et al., *Soft X-ray lithography of high aspect ratio SU8 submicron structures.* Microsyst. Technol., 2008. **14**(9–11): p. 1683–1688.
118. Wouters, D. and U.S. Schubert, *Nanolithography and nanochemistry: probe-related patterning techniques and chemical modification for nanometer-sized devices.* Angew Chem Int Ed Engl, 2004. **43**(19): p. 2480-95.
119. Piner, R.D., et al., *"Dip-Pen" nanolithography.* Science, 1999. **283**(5402): p. 661-3.
120. Szoszkiewicz, R., et al., *High-Speed, Sub-15 nm Feature Size Thermochemical Nanolithography.* Nano Letters, 2007. **7**(4): p. 1064-1069.
121. Hong, S., J. Zhu, and C.A. Mirkin, *Multiple Ink Nanolithography: Toward a Multiple-Pen Nano-Plotter.* Science, 1999. **286**(5439): p. 523-525.
122. Hong, S. and C.A. Mirkin, *A nanoplotter with both parallel and serial writing capabilities.* Science, 2000. **288**(5472): p. 1808-11.
123. Florian, C., et al., *Surface functionalization by laser-induced periodic surface structures.* Journal of Laser Applications, 2020. **32**(2): p. 022063.
124. Klos, A., et al., *Ultrafast Laser Processing of Nanostructured Patterns for the Control of Cell Adhesion and Migration on Titanium Alloy.* Nanomaterials (Basel), 2020. **10**(5).
125. Wu, S.-H., et al., *Porous Titanium-6 Aluminum-4 Vanadium Cage Has Better Osseointegration and Less Micromotion Than a Poly-Ether-Ether-Ketone Cage in Sheep Vertebral Fusion.* Artificial Organs, 2013. **37**(12): p. E191-E201.
126. Rebollar, E., M. Castillejo, and T. Ezquerra, *Laser induced periodic surface structures on polymer films: From fundamentals to applications.* European Polymer Journal, 2015. **73**: p. 162-174.
127. Daskalova, A., et al., *FS laser processing of bio-polymer thin films for studying cell-to-substrate specific response.* Applied Surface Science, 2016. **382**.

CHAPTER 2

Disentangling cadherin-mediated cell-cell interactions in collective cancer cell migration*

*This chapter is based on the published article: T. Zisis[+], D. B. Brückner[+], T. Brandstätter, W. X. Siow, J. d'Alessandro, A. M. Vollmar, C. P. Broedersz, S. Zahler, 'Disentangling cadherin-mediated cell-cell interactions in collective cancer cell migration', *Biophysical Journal* 2022, 121, 44-60.

[+] These authors contributed equally to the manuscript.

T. Zisis., D. B. Brückner, C. P. Broedersz and S. Zahler designed the study. T. Zisis performed all experiments. J. d'Alessandro contributed the tracking software. D. B. Brückner and T. Zisis analyzed data. D. B. Brückner and T. Brandstätter developed the theoretical model. T. Zisis and D. B. Brückner wrote the paper with input from all authors.

2.1 Introduction

Collective cell migration is central to a number of key physiological processes, including morphogenesis during development [1], as well as immune response [2], wound repair [3] and tissue homeostasis [4] in the developed organism. Aberrant cell migration is associated with several pathologies, such as the spread of malignant cancer cells to previously healthy tissues during metastasis [5]. The migratory dynamics of cell collectives in these processes are not merely the outcome of many independently moving cells: they are controlled by cell-cell interactions [6, 7]. Specifically, cells form mechanosensitive cell–cell adhesion junctions (adherens junctions) and coordinate their movements by actively interacting with each other [8]. These interactions facilitate a coordination of collective behavior where a colony of cells invades an empty area [9]. However, it remains unclear how different types of cell-cell interactions control such collective spreading behavior.

The trajectories of single migrating cells are well described by stochastic trajectory models, both for cells migrating on 2D surfaces [10-12] and in confining environments [13-16]. Yet, it is challenging to describe the stochastic collective migration of a cancer cell colony, as cell division and cell-cell contacts have to be taken into consideration. Cell-cell contacts lead to a variety of interactions between cells. Firstly, cells exhibit excluded volume (EV) interactions, where an individual cell occupies space and exerts a repelling force on other cells that move within this space [17]. Secondly, many cell types have the tendency to reorient their direction of motion and move apart upon contact, which is referred to as Contact Inhibition of Locomotion (CIL) [18, 19]. In physical stochastic trajectory models, these interactions are frequently incorporated as a combination of *repulsive interactions*, modelling EV, and *velocity interactions* including velocity alignment as well as CIL [20-24]. Conceptually, there is a key difference between these interactions: while repulsive interactions depend on the relative positions of cells, velocity interactions depend on their motion, i.e. their velocities or polarities. However, it remains unclear how changes in cell-cell contacts within a migrating colony influence these distinct types of interactions and the resulting collective migratory behavior.

Intercellular interactions are strongly dependent on Cadherins, highly conserved calcium-dependent transmembrane proteins that constitute the main component of adherens junctions. Type I classical cadherins (including epithelial (E) and neuronal (N) cadherin as well as P-, R- and M-cadherin [25]) form strong cell–cell adhesion by predominantly homotypic interaction between their extracellular domains [26]. The intracellular cadherin domains connect to β- and α-catenins that associate with the actin cytoskeleton to mediate mechanotransduction [27]. Changes in the normal expression levels of the different cadherin types has been associated with carcinogenesis. One of the most studied processes related to several epithelial tumors is the cadherin switch observed during Epithelial-Mesenchymal transition (EMT). EMT involves the loss of epithelial cell polarity and cell-cell adhesion and the gain of migratory and invasive properties, resulting in the predominance of a mesenchymal phenotype [28]. More specifically, there typically is a strong downregulation of E-Cadherin in parallel with an upregulation of N-Cadherin in EMT. As a result, E-Cadherin adherens junctions disassociate while N-Cadherin junctions establish a relatively weak (compared to E-Cadherin) adherens junction [29].

However, the role of E- or N- Cadherin-mediated intercellular adhesions in cancer cell migration remains controversial. On the one hand, E-Cadherin downregulation has been related to cancer development [30, 31], and it has been shown that the presence of E-Cadherin induces a spreading cell monolayer to retract and form a spheroid aggregate, a process called dewetting [32], suggesting its role as a potent tumor suppressor. On the other hand, a number of studies suggest the opposite effect: E-Cadherin is required for coordinated collective movement of cancer cells in organotypic culture [33] and for metastasis in multiple models of breast cancer [34], it promotes expansion of bladder carcinoma in situ [35], and is highly present in patients with prostate cancer [36], ovarian cancer [37], and glioblastoma [38]. A similar controversy characterizes the involvement of N-Cadherin in migratory behavior. Although N-cadherin is a marker of EMT and its expression has been associated with the development of multiple cancer types [29], there are studies pointing in the opposite direction.

In fact, N-cadherin loss was associated with increased tumor incidence [39] and metastasis [40]. Consequently, a question is yet to be answered: what is the distinct contribution of E- and N-Cadherin junctions to cell-cell interactions and the resulting spreading dynamics of cancer cell colonies?

Here, we aim to investigate this question by combining experimental observations on collectively migrating cells and a minimal physical model of the spreading behavior. We use an epithelial bladder cancerous cell line (T24), which is characterized by high N-Cadherin expression and limited [41] or zero functional levels of E-Cadherin [42, 43]. After initial confinement of a colony of cells to a circular micropattern, the cells are released using chemical tools [44, 45]. We quantify the collective migration by identifying and tracking the entire ensemble of single cell trajectories in each colony. To investigate the effect of cell-cell contacts for the migration, we inhibit E- or N-Cadherin junctions via specific blocking antibodies. In both cases, our analysis reveals that such inhibition leads to a reduced spreading velocity of the cell colonies. To elucidate these dynamics, we develop a minimal active particle model for collective migration, that includes cell proliferation as well as repulsive and CIL interactions. This model shows that inhibiting E- or N-Cadherin has an effect akin to reducing the strength of repulsive cell-cell interactions in the model. In other words, disturbing either of these cadherin junctions decreases the displacement generated when neighboring cells push each other away in order to create space for themselves. Therefore, we show that both E- and N-Cadherins contribute to the maintenance of intercellular contacts that facilitate cell spreading via repulsive interactions, causing cells to move further away from each other. This could be a consequence of cadherins 'sharpening' cellular boundaries, through e.g. shape regulation, changes in interfacial tension, or increased cell-cell recognition [46]. These observations indicate the important role of cadherins in metastatic events and their potential as cancer treatment targets.

2.2 Materials and methods

2.2.1 T24 cell culture transfection with H2B-GFP plasmid for nucleus labeling.

H2B–GFP expression vectors, were obtained from Addgene (#11680). T24 cells exponentially growing in Dulbecco's modified Eagle's medium (DMEM) supplemented with 10% fetal calf serum (FCS) were transfected with 2.5 µg of the H2B–GFP expression vector carrying a G418 resistance as selection marker, using an Amaxa R-Kit (Program I-013) under constant humidity at 37°C and 5% CO2. 24h after the transfection, cells were treated with G418 (A1720, Sigma-Aldrich) to an end concentration of 0.8mg/ml in 2ml well-plates and then further cultivated in T25 flasks and later on in T75 flasks with the same concentration of G418 (0.8mg/ml). After two rounds of additional cell sorting by flow cytometry the GFP+ cells at passage 30 were frozen in a nitrogen tank at a concentration of 1x 10^6 cells/ml.

For all collective migration experiments, T24 cells were pre-grown as monolayers and diluted down to the desired concentrations in Dulbecco's modified Eagle's medium (DMEM) supplemented with 10% fetal calf serum (FCS), 10.000 U/ml penicillin/streptomycin and 0.8 mg/ml antibiotic G418 under constant humidity at 37°C and 5% CO_2.

2.2.2 Microcontact printing for circular pattern generation

8-well uncoated µ-Slides (ibidi, Martinsried, Germany) underwent 3 min of oxygen plasma treatment (Plasma cleaner typ ''ZEPTO,'' Diener electronic, Ebhausen, Germany) at 0.3 mbar for activation (generation of OH-hydroxyl bonds). Then, 250 µl/well of 0.05 mg/ml fibronectin (R&D Systems, US) solution in MilliQ were added to the now highly reactive surface and incubated at room temp for 2 hours. After washing 2 times with 500 µl of milliQ H_2O the surface was allowed to dry. Following that, we used standard microcontact printing techniques to create PDMS stamps with circular patterns. We placed one stamp at the center of each well and plasma treated the surface one last time at the same conditions as before. This step

removes all fibronectin from the surface except the areas that are protected by the stamp, so all the unprotected areas on the surface become hydroxylated and highly reactive again. Without removing the stamps, we added a 7 μl drop of 1mg/ml PLL(20)-g[3.5]- PEG-N_3(3) (APP) (Susos AG, Switzerland) solution in MilliQ right next to each stamp allowing surface tension to absorb the liquid underneath the stamp. We let the above condition settle for 45 min. We gently removed the stamp and washed 2 times with 500 μl of MilliQ. Now the circular areas contain fibronectin and are highly cell-adhesive while the surrounding areas are initially cell repellent. At this point, T24 cells were trypsinized after reaching confluency, diluted to the desired density (70.000 cell/ml) in the aforementioned DMEM-based medium and 250 μl of this cell suspension were added in each well and allowed to settle overnight at 37 °C. The next day, the cell medium was replaced with 200 μl of fresh medium and the slide was placed under the microscope. Finally, 10 μl of 100μM BCN-cRGDfk (Synaffix, Netherlands) in PBS were added in the medium of each well to a final concentration of 20 μM. The BCN groups formed a link with the Azide groups of the APP-covered, cell-repellent areas around the colonies. This resulted in the binding of RGD on the surface, thereby rendering the surrounding areas cell adhesive and initiating cell migration.

2.2.3 Blocking antibody treatment of T24 circular colonies

For the blocking antibody treatment experiments, we followed the exact same cell preparation protocol as above with the addition of the following steps: On the next day, after the first washing step, 200 μl of 5mM EGTA solution were added in each well for 30 min. This step was performed in order to break the existing cadherin junctions and allow the blocking antibodies (anti N-Cadherin antibody: LEAF™ Purified anti-human CD325, #350804, Biolegend, USA; anti E-Cadherin antibody: CD324 #16-3249-82, Invitrogen, USA) to bind to their respective epitopes. Following that, the wells were washed two times with 200 μl of fresh cell medium. Subsequently, 200 μl of the appropriate E- (10 or 25μg/ml) or N- (25, 50 or 100μg/ml). Cadherin blocking antibody solution in cell medium were added in each well. Cells

were incubated additionally for 30 min and then the slide was placed under the microscope. Finally, 10 µl of 100µM BCN-cRGDfk (Synaffix, Netherlands) in PBS were added in the medium of each well to a final concentration of 20 µM.

2.2.4 Cell imaging

Live cell imaging was performed using the T24 seeded 8-well fibronectin/APP patterned slides with an Eclipse Ti inverted microscope (Nikon, Dusseldorf, Germany) with a 4x/10x phase contrast objective and a CCD camera ([DS-Qi1Mc] Nikon, Dusseldorf, Germany). The slides were inserted into a 37 °C heating and incubation system that was flushed with actively mixed 5% CO_2 at a rate of 10 l/h, and the humidity was kept at 80% to prevent dehydration. The cells were imaged in bright-field and the fluorescence of the nuclei was detected at a 488 nm wavelength using the integrated fluorescence LED. Time-lapse video microscopy was performed with a time interval of 5 min between images over 24 h.

2.2.5 Evaluation of cell division

Using the videos acquired as described above, we manually tracked the number of cell divisions in each frame in outer ring (edge) vs the inner area (core) of the cluster and the definition of these areas can be observed in Supplementary Figure 8. For each area, the number of cell divisions counted was divided by the total number of cells in that area and expressed as a percentage of the total cell divisions.

2.2.6 Tracking of single cell trajectories

The positions of individual cells were detected as previously described [45] using custom-made ImageJ macros implementing the ‘Find Maxima’ built-in function. The individual trajectories were then reconstructed using a squared-displacement minimization algorithm (http://site.physics.georgetown.edu/matlab) and data analysis was performed via custom-made Matlab programs.

2.2.7 qPCR

T24 cells were lysed for mRNA isolation. Briefly, “Buffer RLT, Lysis Buffer” (RNeasy® Mini Kit (250) PCR lab) was mixed with DTT 2M at a ratio of 50:1. After medium aspiration and ice-cold PBS rinsing, ice-cold lysis buffer was added and the lysates were stored at -80 °C. For the mRNA, isolation the RNeasy® Mini Kit (250) (QIAGEN, Hilden, Germany) was used according to the modified manufacturer’s instructions. 2 µl of the mRNA samples was used directly for mRNA concentration determination using a Nanodrop® Spectrophotometer (PEQLAB Biotechnologie, Erlangen, Germany) with absorption at 260 nm (specific for mRNA) while impurities were determined at 280 nm. For the reverse transcription of mRNA to cDNA, 2X RT master mix was prepared containing: 10% TaqMan RT Puffer-10x, 0,04% dNTPs, 10% random hexamers, 5% Reverse Transcriptase, 21%RNAase free water, 50% H2O+ RNA 2.5µg. For the quantitative PCR the following primers were obtained from metabion GmbH: E-Cadh_1_F (MM125, 5´TGG GCC AGG AAA TCA CAT CC3´), E-Cadh_1_R (MM126, 5´GGC ACC AGT GTC CGG ATT AA3´); N-Cadh_2_F (MM133, 5´CCT TTC AAA CAC AGC CAC GG3´), N-Cadh_2_R (MM134, 5´TGT TTG GGT CGG TCT GGA TG3´). We used 2 µl of the acquired cDNA in each well of the MicroAmp® Fast Optical 96-Well Reaction Plate or 2 µl of autoclaved Millipore H2O for the no-template controls (NTCs), respectively. 10.5 µl of PCR master mix containing 6.25 µl of PowerUPTM SYBR® Green Master Mix, 3.75 µl of autoclaved Millipore H2O, 0.25 µl of forward primer and 0.25 µl of reverse primer were added to each probe well and the qPCR was performed in a QuantStudio™ 3 Real-Time PCR system (ThermoFisher, MA, USA). Data were normalized to the housekeeping gene GAPDH. The analysis was carried out with the $\Delta\Delta$CT method as previously described [47], using the ThermoFisher cloud and threshold cycle was set to > 9-15 and ≤ 30 to allow acceptable detection for best reproducibility.

2.2.8 Western Blots

Cells were harvested and lysed in RIPA lysis buffer containing a protease inhibitor mix (Roche #4693159001). Lysates were centrifuged at 10,000 x g for 10 min and 4 °C. Protein amounts were assessed by Bradford assay, and an equal amount of protein was separated by SDS-PAGE and transferred to nitrocellulose membranes (Hybond-ECLTM, Amersham Bioscience). Membranes were incubated with blocking buffer containing 5% BSA and 0.1% Tween 20 in PBS for 1h at room temperature, followed by 3x 5 min. rinsing with PBS-T. After that, membranes were incubated with rabbit anti-ECAD (24E10) monoclonal Ab (1:500; #3195, Cell Signaling Technology, Inc. USA) or rabbit anti-NCAD (D4R1H) XP® monoclonal Ab (1:500; #13116, Cell Signaling Technology Inc. USA) at 4°C overnight. Membranes were washed again with PBS-T 3 times for 5 min. Secondary antibody (HRP-Goat-Anti-Rabbit 1:1000; #111-035-144, Dianova, Germany) were used for 2h incubation at room temperature and subsequently conjugated with horseradish peroxidase and freshly prepared ECL solution (protected from light), which contained 2.5 mM luminol (detailed description of ECL solution preparation in table 1). Conjugated proteins were detected by the ChemiDoc™ Touch Imaging System (Bio-Rad, USA) and quantified by ImageLab software (Bio-Rad, USA). For quantification protein amount was normalized to total protein-loading, detected by 2,2,2-trichloroethanol activation as described previously [47] [48].

#	Reagent	Volume	Stock
1	distilled Water	4500µl	
2	Tris-Base pH 8.5	500µl	
3	p-coumaric acid	22µl	15mg/ml in DMSO (Aliquots at -20°C)
4	luminol	50µl	44mg/ml in DMSO (Aliquots at -20°C)
5	H2O2 30%	3µl	

Table 1: Western Blot Solution Reagents

2.2.9 Immunohistochemistry

We performed the following stainings

- E-Cadherin+ N-Cadherin+ Hoechst co-staining (Methanol/acetone fixation protocol)
- γ-Tubulin+ Actin+ Hoechst co-staining (Methanol/acetone fixation protocol)
- γ-Tubulin+ Hoechst co-staining (Methanol/acetone fixation protocol)
- Actin + Hoechst co-staining (PFA fixation protocol)

Cells were fixed at 5h or 24h after the start of cell migration with 4% PFA (only in case of actin staining) or 1:1 pure methanol/acetone for 20 min. After 10min of permeabilization with 250 µl/well 0.5% Triton X-100 at room temperature (only for actin staining) and 5 x 5min. washings with PBS, cells were incubated with (1% BSA in PBS, 250 µl/well) at room temperature for 1h. Then the primary antibody was added (150 µl/well). The details on the primary antibodies used are listed in the table below.

Target	Company	Lot	Dilutiion	Species	Number
Ecad	Invitrogen	131700	1:2000	mouse	531
Ncad	Cell signaling	4016	1:200	rabbit	477
γ-Tubulin	Sigma	T 6557	1:200	mouse	380

Table 2: List of primary antibodies

After overnight incubation with the primary antibody, the solution was removed and cells were washed 5 times for 5 min. with PBS and then incubated with secondary antibody in 1% BSA for 1h at room temperature in the dark. The details on the secondary antibodies used are listed in the table below.

2nd Antibody/dye	Company	Lot	Dilutiion	Species/specificity
Alexa 488-Ab‘‘ (for gamma Tubulin and E-cad)	Invitrogen	11001	1:400	Goat Anti-mouse
Alexa 647-Ab‘‘ (for N-cad)	Invitrogen	21443	1:400	chicken Anti-Rabbit
Hoechst 33342 (blue-fluorescent)	Thermo Scientific	62249	1:400	Nuclear-specific dye
Actin stain (red-fluorescent phalloidin)	Invitrogen	22287	1:400	Specific to native quaternary structure of F-actin

Table 3: List of secondary antibodies

The solution was then removed and cells were washed 5 times for 5 min with PBS. For mounting, 1 drop of mounting medium was added before sealing with cover slips and Incubating for 30 minutes at room temperature.

2.2.10 Imaging and image analysis of stainings

Cells were imaged using a Leica TCS SP8 confocal microscope with HC PL Fluotar CS2 10×/0.3 NA DRY (Leica, Wetzlar, Germany) using LAS X Core software. For the imaging of E-, N- Cadherin, γ-Tubulin and Actin staining, the argon laser with an excitation wavelength of 488 or 647 nm was used, and the wavelength range of the detector was set between 480−530 and 640−680 nm, respectively. For Hoechst 33342 imaging, the diode laser was employed with excitation wavelength of 405 nm and the detection wavelength was set between 460 to 490 nm. All images were analyzed using the ImageJ version 1.53c61 software tool.

For the assessment of cell polarization on the γ-Tubulin (+Actin) +Hoechst co-stained colonies, we consider a cell to be polarized when the microtubule-organizing center (MTOC, visible as a distinguished green dot) is located rear/frontal to the nucleus in relation to the direction of movement [49]. The direction of movement is towards the higher microtubule distribution edge in each cell [50]. We quantified the number of cells polarized away from cell-cell contacts (examples in red arrows, towards cell-cell contacts (examples in blue arrows) or non-polarized (orange arrows) at the edge of the cluster (Supplementary Figure 7). The numbers were divided by the total number of counted cells at the edge of the cluster.

For the analysis of E- and N-Cadherin immunofluorescence in untreated (control) colonies vs E- or N-Cadherin blocking antibody-treated colonies, we measured the fluorescence intensity in each channel (green for E- and red for N-Cadherin). The fluorescence intensity of each the blocking condition was normalized to the fluorescence intensity of the control condition.

2.2.11 Cross-correlation functions of velocity fluctuations

To investigate the interactions of cells in the experiment, we calculate the spatial velocity cross-correlation function

$$C(r) = \frac{\sum_{ij} v_i \cdot v_j \delta(r - r_{ij})}{\sum_{ij} \delta(r - r_{ij})}$$

where v_i is the two-dimensional velocity vector of cell *i* and $\delta(r - r_{ij})$ is the Dirac delta-function. This function measures how 'similar' the velocities (magnitude and direction) of cells at distance *r* from one another are on average. Using discrete bins as an approximation for the delta-function for finite data, we obtain expected results both for experimental and simulated data.

The complete velocity field is composed of the collective outward motion, a dilatational mode, and additional velocity fluctuations due to interactions between the cells. Following previous work [51], we calculate these fluctuations by obtaining the scalar dilatation D as a function of time, by optimizing the quantity $\sum_i [x_i(t+T) - Dx_i(t)]^2$. The fluctuation velocities are then giving by $u_i = [x_i(t+T) - Dx_i(t)]/T$. Note that here, we use a time-interval $T = 15\Delta t$ which is larger than the time-resolution of the experiment. This allows us to average out the short-time scale noise fluctuations of the cellular velocities, and instead focusses on longer time-scale process relevant to the spreading dynamics. We test this approach in our simulations, and find that it accurately detects the presence of velocity-dependent interactions, such as CIL (Supplementary Figure 4).

2.2.12 Dilatational order parameter

To estimate the order parameter of the collective spreading process, we calculate the dilatational order parameter Λ, as previously defined in ref. [51]:

$$\Lambda = \sum_i \frac{x_i(t) \cdot [x_i(t+T) - x_i(t)]}{|x_i(t)||[x_i(t+T) - x_i(t)]|}$$

using $T = \Delta t$. This parameter is defined in the range $-1 < \Lambda < 1$, and measures the degree of coherent expansion (for $\Lambda > 0$) or contraction (for $\Lambda < 0$). For Λ close to 0, there is little dilatational order.

2.2.13 Computational modeling

To provide a minimal computational model for the spreading process, we implement a simple active particle model for collective cell migration. Similar to previous works [22, 45, 52-55], we describe the motion of the cells using stochastic equations of motion with interactions. Specifically, we use the equation of motion

$$\frac{d\vec{v_i}}{dt} = -\gamma\vec{v_i} + \vec{F}_{\mathrm{rep}}\left(|r_i - r_j|\right) + \vec{F}^{i}{}_{\mathrm{CIL}} + \sigma\vec{\eta}_i(t)$$

where $\vec{\eta}_i(t)$ represents a Gaussian white noise with $\langle\vec{\eta}_i(t)\rangle = 0$ and $\langle\vec{\eta}_i(t)\vec{\eta}_j(t')\rangle = \delta(t - t')\delta_{ij}$. The model furthermore includes a persistence term $-\gamma v$, where γ^{-1} is the persistence time of the cells. The repulsive interactions are implemented as the repulsive part of a quadratic potential

$$\vec{F}_{\mathrm{rep}} = -\varepsilon\left(2\lambda - r_{ij}\right)\frac{\vec{r}_{ij}}{r_{ij}}$$

where λ represents the radius of the cells, and ε is the strength of the interaction.

The contact inhibition of locomotion (CIL) interaction $\vec{F}_{\mathrm{CIL}}$ is implemented in the form of a rotation of the velocity vector away from the distance vector $\vec{r}_{ij} = \vec{r}_j - \vec{r}_i$ to nearest neighbours, which are defined by being within an interaction range of radius 2.5λ, and being on collision course with cell *i*, i.e. $\vec{v}_i \cdot \vec{r}_{ij} > 0$. The angular displacement only depends on the velocity direction, a constant acceleration α and the number as well as the positions of nearest neighbours: For each nearest neighbour the direction of the axis of rotation is found such that the rotation will be away from the nearest neighbours. All directions of the axes of rotations of all nearest neighbours are added up and multiplied by the acceleration α. Specifically, we use

$$\vec{F}^{i}{}_{\mathrm{CIL}} = \alpha \sum_{j} s_{ij} \left(\hat{e}_z \times \frac{\vec{v}_i}{|\vec{v}_i|} \right)$$

where

$$s_{ij} = \begin{cases} -\mathrm{sign}\left(\frac{\vec{v}_i}{|\vec{v}_i|} \times \vec{r}_{ij} \right) \cdot \hat{e_z}, & |\vec{r}_{ij}| < 2.5\lambda \text{ and } \vec{v}_i \cdot \vec{r}_{ij} > 0 \\ 0, & \text{otherwise} \end{cases}$$

In simulations where velocity alignment rather than CIL is used (Supplementary Figure 4) , we replace $\vec{F}_{\mathrm{CIL}}$ by an alignment interaction $\beta \vec{V}_i / |\vec{V}_i|$ with strength β, which is implemented as a constant acceleration in the direction of the average velocity $\vec{V}_i = \langle \vec{\mathrm{v}}_{\mathrm{j}} \rangle_{j \in NN_i}$ of nearest neighbours within an interaction range of radius 2.5λ.

Finally, cell division is implemented with a constant probability $\nu \mathrm{d}t$ of dividing, provided there is sufficient space for the appearance of new cells. In a division event, a cell produces a daughter cell in its direct neighborhood with an initial velocity pointing away from the mother cell.

The simulation is performed in non-dimensional units such that $\gamma^{-1} = \lambda = 1$. We use the parameters $\sigma^2 = 2$, $\nu = 0.1$, and vary ε between 0.1 and 40, and α between 0 and 12. We initialize $N = 37$ particles within the initial confinement radius R. The stochastic trajectories of the model are then simulated by step-wise Euler updates with a time-step of $dt = 10^{-3}$. We first perform a pre-equilibration run with a confinement potential at $r = R$, modelling the initial confinement phase. At $t = 0$, we remove the boundary by setting the confinement potential to zero, leading to the spreading of the simulated cluster.

2.2.14 Statistical evaluation

For statistical analysis of the data one-way ANOVA followed by Dunnett's multiple comparisons test was performed using GraphPad Prism version 8.0.0 for Windows,

(GraphPad Software, San Diego, California USA, www.graphpad.com). n.s.= not significant, * $p < 0.05$, ** $p < 0.01$.

2.3 Results & Discussion

2.3.1 Release from a micropatterned circular adhesive area leads to collective cell spreading

To generate an experimental setup for tracking collective cell spreading dynamics, we develop a micropatterned platform from which cells can be released in a standardized manner. Specifically, we design a new patterning approach based on a novel sequence of surface plasma treatment, standard microcontact printing, fibronectin coating and click chemistry steps. This process results in the production of a 100 μm radius circular fibronectin-coated adhesive areas that are surrounded by cell-repellent azido (PLL-g-PEG) (APP)-coated surfaces. These non-adhesive surfaces can then be activated on demand, via a biocompatible click chemistry reaction between the azide groups of the APP on the surface and added BCN-RGD peptides to allow time-controlled cell migration outside the circular areas [56] (see Materials and Methods and Fig. 1). Subsequently, we use T24 urothelial bladder carcinoma epithelial cells which is a well-established malignant cell line [57], widely used in cell migration research [58-61] and in EMT transition [61]. The cells are detectable using fluorescence microscopy imaging via their nuclear H2B-GFP fluorescent tag.

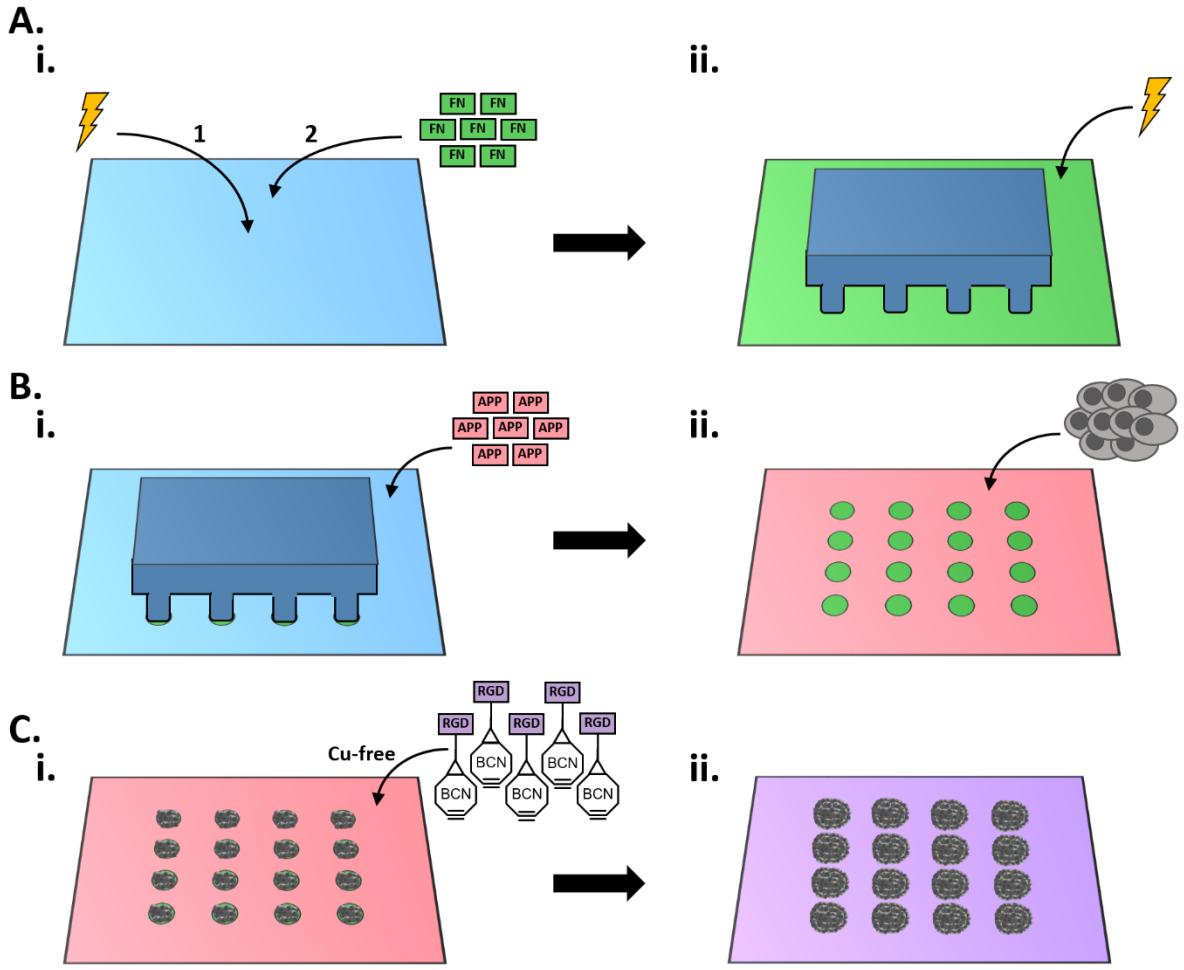

Figure 1: Schematic representation of the microcontact printing and click-chemistry process

A i) Ibidi's uncoated surface (here one well is represented) undergoes plasma treatment to become reactive, for subsequent attachment of fibronectin (FN). ii) Example of PDMS-square stamp with circular patterns produced with standard microcontact printing techniques (blue). The stamp is placed at the center of the well and the surface is plasma-treated again. The whole surface except for the stamp-protected circular areas loses its fibronectin coating and becomes hydroxylated. B i) With the stamp remaining in place, APP is added next to it and absorbed by the whole surface except for the stamp-protected circular areas (green). B ii) This results in 100 µm radius fibronectin-coated circular areas (green) surrounded by an otherwise cell repellent APP surface (red). T24 cancer cells are seeded on the circular areas forming the initial cell population. C i) BCN -RGD peptides are then added and bind to the APP coated surface via click chemistry reaction between the BCN and the azide groups of the APP. C ii) The previously cell-repellent surface is now coated with RGD and thus, highly cell adhesive. The cells are able to expand (migrate) from the circular areas to the rest of the surface.

We perform time-lapse fluorescence and bright-field microscopy for the first 24 hours after surface activation. Here, we observe cells increasingly spreading outwards over time, in all

directions, covering a large circular area (Fig. 2 A, Supplementary Movie S1). To gain access to the dynamics of the entire cell collective, we perform tracking of the fluorescently tagged nuclei as previously described [45], giving access to the full ensemble of cell trajectories in each escaping cluster (Fig. 3 B).

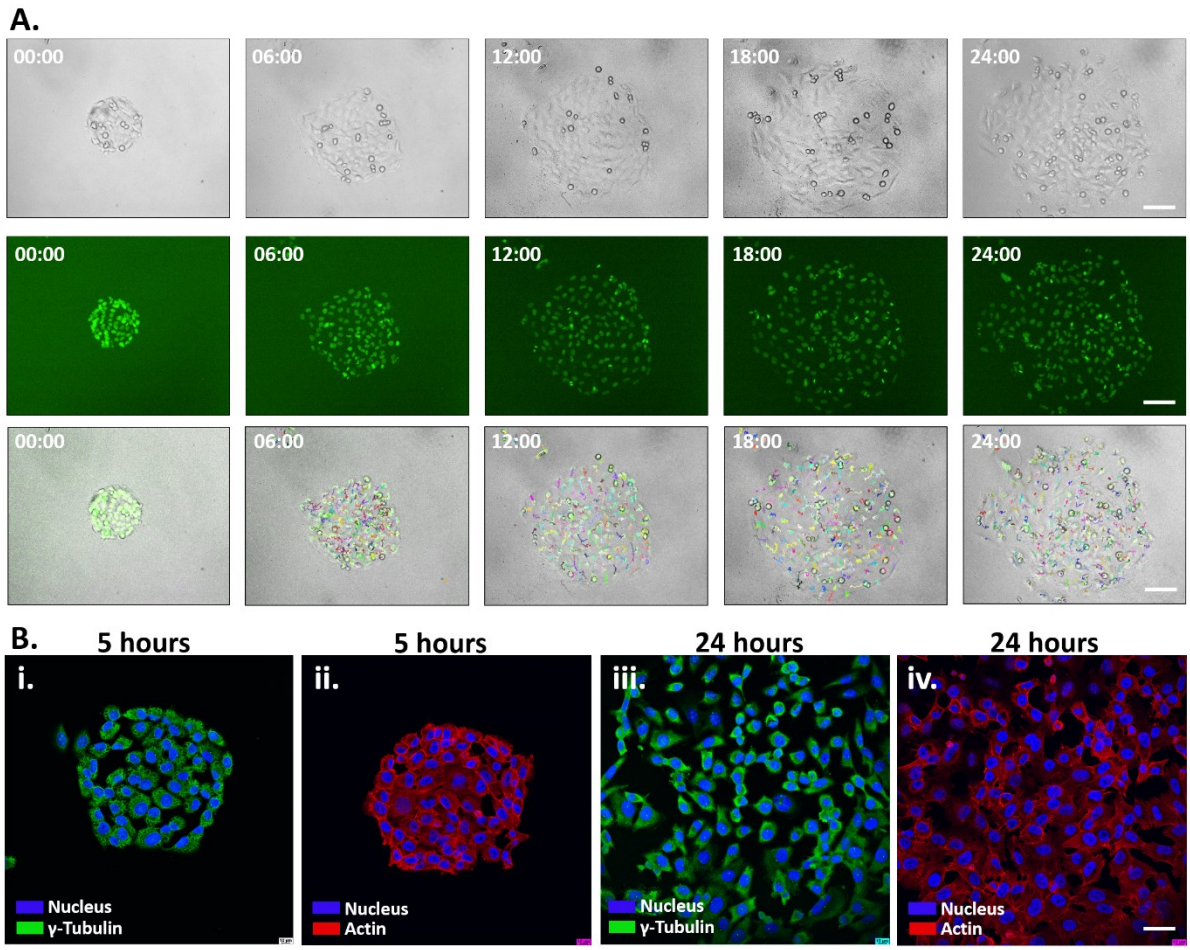

Figure 2: Cell spreading time-lapse and cytoskeletal staining of untreated (control) colonies

A) Time-lapse bright-field (upper), fluorescence (middle) microscopy images or overlay with cell tracks (lower) showing the T24 cell migration with 6h intervals from 0h to 24h after surface activation. Scale bar: 100 µm. B) representative confocal images of colonies at 5h after surface activation with γ-Tubulin + nucleus staining (i) or actin + nucleus staining (ii). The same colonies at 24h after surface activation are shown in iii and iv, respectively. Scale bar: 50 µm. The cytoskeletal stainings were performed to enable better visual detection of the cell boundaries. Cell clusters are not confluent and a high number of gaps between the cells can be observed.

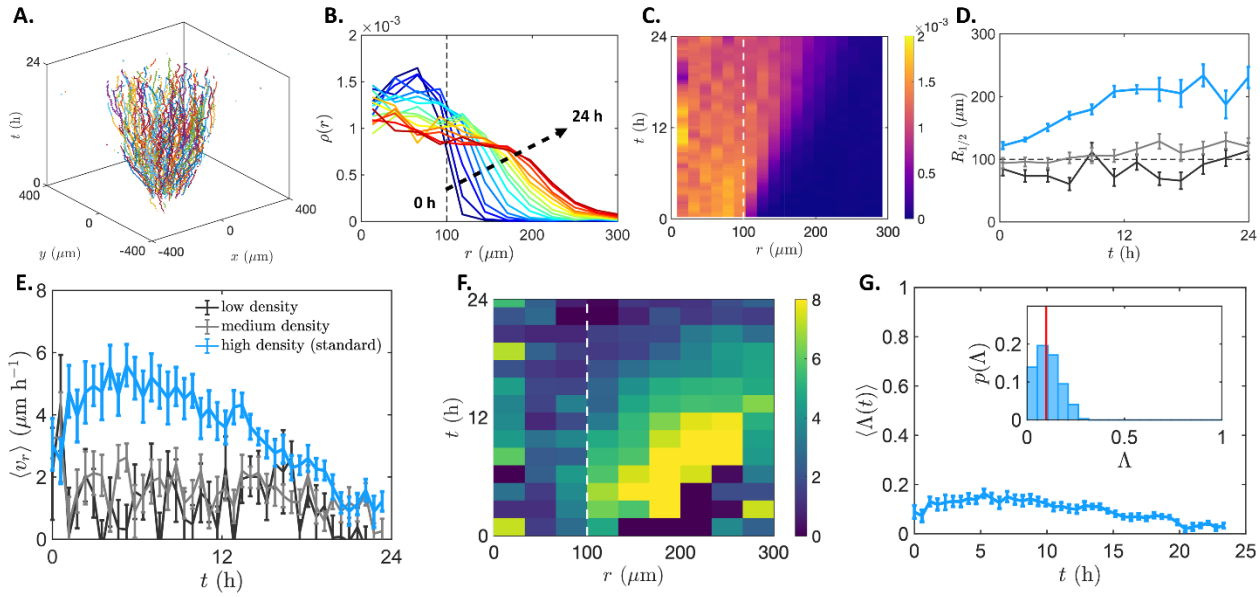

Figure 3: Cell spreading and evolution of cell density of control (untreated) T24 cells

A) Space diagram of colony spreading up to 24h after surface activation. B) Evolution of the density profile over time (blue to red) plotted as the mean of n=12 colonies. C) Kymograph of the cell density evolution. Dashed lines indicate the initial confinement radius. D) Average distance where density has decayed to half of its value in the center of the original confinement (i.e. at r=0). E) Mean radial velocity over time for clusters with different initial density. Specifically, the high-density condition corresponds to an average cell number 40±1.5 within the initial confinement. In the medium- and low-density condition the average cell number within the initial confinement is 18±1.6 and 10±1, respectively. F) Kymograph of the evolution of the radial velocity in space and time (measured in µm/h). Dashed white line indicated the initial confinement radius. G) Average dilatational order parameter as a function of time (defined in Methods). Inset: Probability distribution of observed order parameters; red line indicates the average. Error bars: SEM; n=12 for panels B, C, F, G. For D, E: n_{high}= 12, n_{medium}= 15, n_{low}= 12.

As shown by the space-time trajectories of the system, the cells have an overall tendency to spread outwards from the initial confinement, and after a period of 10h, a large fraction of the cells has left the initial confinement (Fig. 3 A). The spreading process is quantified by the evolution of the radial density profile *ρ(r)* of the cluster (Fig. 3 B, C). Specifically, we calculate the average number of cells per area element as a function of the distance to the center of the initial confinement radius. As a function of time, the density within the confinement initially decreases, due to cells leaving the confinement through random migration. Correspondingly, the density outside the confinement increases. Interestingly, after a period of approximately

10h, the density inside the confinement stabilizes at a constant value. To further quantify the overall spreading, we calculate the average radius at which the density profile has decayed to half its value at the center of the initial confinement $R_{1/2}$ (Fig. 3 D). The spreading of the cluster appears to be determined both by the movement of cells, as well as cell proliferation (Supplementary Movie S1). To quantify proliferation, we track the number of cells as a function of time (Supplementary Figure 2), which reveals that the number of cells doubles within 10h. Furthermore, we manually track the number of cell divisions in each frame (~5 min. difference between frames) in outer ring (edge) vs the inner area (core) of the cluster. We show that divisions are equally distributed across the colony (Supplementary Figure 8). This is true not only for the untreated condition (mean diff. $_{\text{core-edge}}$= -2.1±1.7; p=0.27), but also for the E-Cadherin blocking antibody condition (mean diff. $_{\text{core-edge}}$ = -2.7±1.7; p=0.18) as well as the N-Cadherin blocking antibody condition (mean diff. $_{\text{core-edge}}$ = -0.02±1.4; p=0.99). Finally, to quantify migration, we measure the average radial velocity of the spreading cells as a function of time, which reveals a marked peak at intermediate spreading times (Fig. 3 E).

These statistics are helpful to investigate the impact of collective effects. Thus, we analyzed clusters initialized in the same confinement radius, but with lower cell concentrations. At these lower concentrations, less spreading is achieved (Fig. 3 D), and the peak in radial velocity disappears (Fig. 3 E), indicating that the dynamics observed in our experiments are density dependent, and therefore have a distinct collective character. Together, these results indicate that release from a micropatterned area leads to the spreading of cell clusters with distinct collective character.

2.3.2 Collective spreading of T24 cancer cells is driven by single-cell migration with transient contacts

Having established the collective character of the spreading process, we next seek to determine whether this expansion is driven by the outward motion of leader cells attached to a confluent monolayer by cell-cell adhesions [62, 63]; or whether this process is dominated by

stochastic single-cell migration with transient cell-cell contacts. To this end, we perform high-resolution cytoskeletal imaging with staining of actin and γ-Tubulin (Figure 2 B and Supplementary Figure 9). These experiments reveal that, both at early and late time-points, the cell colonies are not fully confluent as there are significant gaps within the cluster. Furthermore, we found no evidence for the presence of leader cells at the edge of the cluster. Our cytoskeletal staining showed no apparent prevalence of cells with large lamellipodia (a characteristic of leader cells [64, 65]) at the edge of the monolayer compared to the rest of the inner reservoir. There were also no apparent actomyosin cables at the colony boundaries or finger-like structures invading the free space that are associated with leader cells [66-68].

We next turn to the time-lapse imaged trajectories to further quantify the nature of collective motion in this system. At the single cell level, these trajectories are highly stochastic, as expected from single cells which perform persistent random motion on unstructured 2D substrates [12] (Fig. 3 A). Furthermore, time-lapse imaging reveals significant stochastic motion of single cells and frequent nearest-neighbor rearrangements during the spreading process (Supplementary Movie S1). To quantify the degree of stochasticity in the collective spreading, we calculate the order of the expansion through the dilatational order parameter D, defined to be 1 for perfectly ordered expansion, and 0 for disordered motion (Methods). This quantity is distinct from the radial velocity, which instead measures the magnitude of the collective motion rather than its order. Interestingly, we observe an average order parameter of 0.1, indicating a large degree of disorder in the spreading process (Fig. 3 G). Finally, we investigate the origin of the observed peak in the radial velocity by measuring the radial speed as a function of position within the cell cluster (Fig. 3 F). This analysis shows that the onset of radial motion occurs at the periphery of the cluster, and does not spread inwards, which is in contrast to previous findings in confluent monolayers of non-cancerous cell types [69]. Together, these observations suggest that rather than spreading of a confluent, mechanically connected monolayer [62, 63], this system exhibits collective motion with predominantly single-cell migration with transient contacts. The collective spreading behavior is therefore

likely determined by a combination of single-cell motility, cell proliferation, and transient cell-cell interactions.

2.3.3 Minimal active particle model captures experimental colony spreading

To elucidate the interplay of the various factors affecting the collective migration in our experiments, we develop a minimal active particle model for collective cell migration (Fig. 4 A). In this model, single cells perform persistent random motion, as observed for single cell migration on two-dimensional substrates [10]. We include transient cell-cell interactions in our model through two distinct contributions [22, 45, 55]: a repulsive component modelling excluded volume (EV) interactions, and Contact Inhibition of Locomotion (CIL) which models the tendency of cells to reorient away from contacts upon collision. Thus, unlike previous models for confluent cell monolayers with elastic [70, 71] or attractive [54, 72, 73] interactions, with this model, we aim to capture the spreading of a non-confluent cell layer driven by single-cell migration with transient interactions (Fig. 4 B). We first confine the particles into a circular region of radius R and then observe their behavior upon release, exactly like in the experiment (Methods Section and Fig. 4 B).

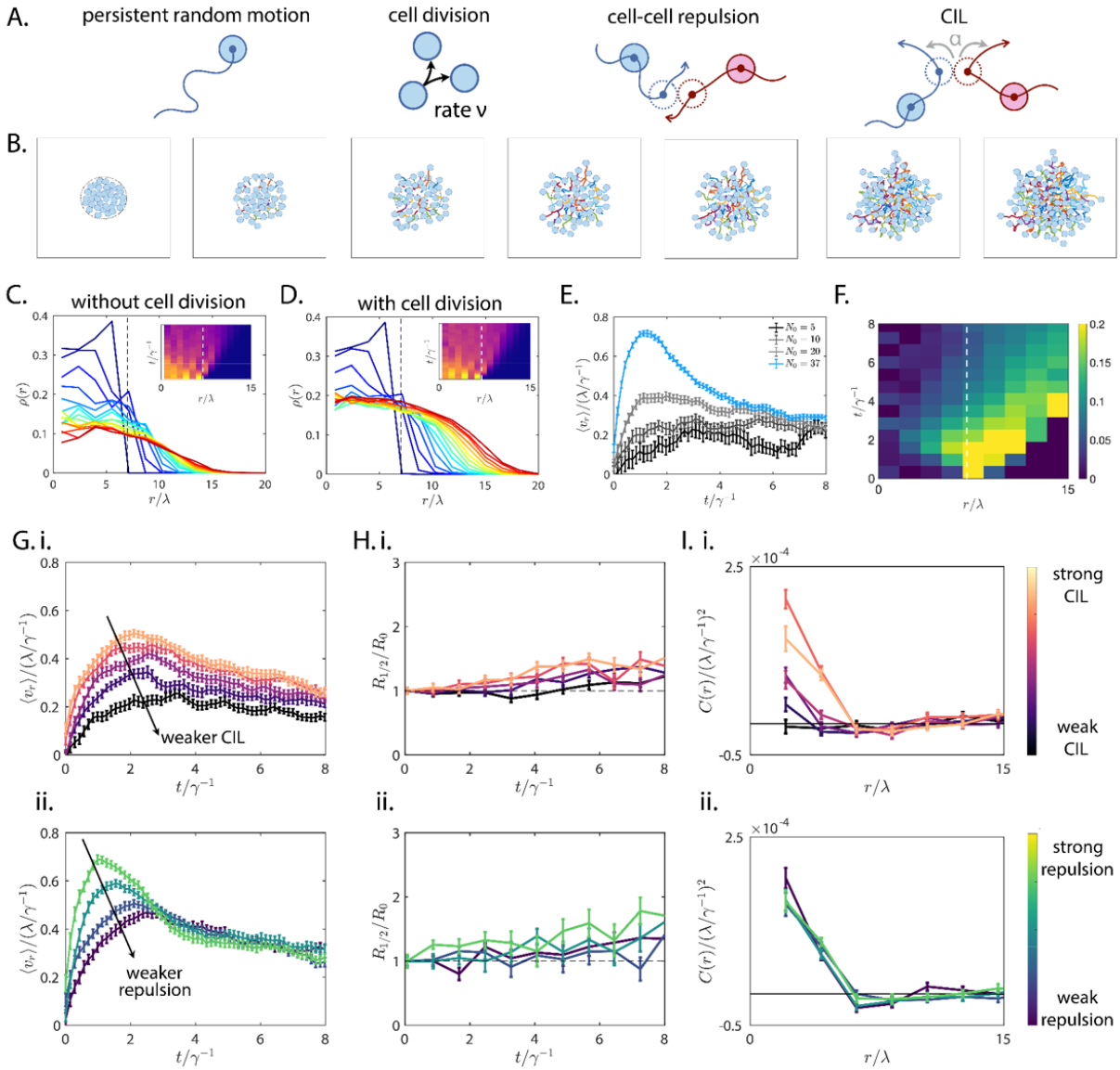

Figure 4: Computational model for collective cell spreading

A) Schematic of the components of our active particle model, from left to right: persistent random motion of individual particles, cell division with constant rate ν, excluded volume interactions, and Contact Inhibition of Locomotion. B) Time-series of a cluster spreading simulation. Cell positions are shown as blue circles of radius λ, which is the radius of the repulsive potential. Previous motion of the cells is shown as colored trajectories. C, D) Evolution of the density profile over time (blue to red) plotted as the mean of n=30 colonies. Inset: Kymograph of the cell density evolution. Dashed lines indicate the initial confinement radius. C corresponds to a model without cell division, while D includes cell division. E) Mean radial velocity over time for clusters with different initial density. F) Kymograph of the evolution of the radial velocity in space and time for the model including cell division with high density. Dashed white line indicated the initial confinement radius. G) Mean radial velocity over time for. H) Average distance where density has decayed to half of its value in the center of the original confinement (i.e. at r=0). I) Cross-correlation of velocity fluctuations. Error bars: SEM; n=30 for all panels. For G, H, I: (i) clusters with different CIL interaction amplitudes, (ii) different strengths of cell-cell repulsion interactions.

Interestingly, this model predicts a rapid decay of the density within the initial confinement area over time, as particles perform random motion and are repelled by their neighbors and move outwards (Fig. 4 C). This observation is inconsistent with our experimental data, which showed only a weak decay in the initial confinement area (Fig. 3 D, E). As shown by our cell proliferation estimations, cell division plays an important role on the time-scale of tissue spreading in this system: the number of cells nearly doubles within 10h (Supplementary Figure 2). We therefore include a basic implementation of cell division in our model, where cells stochastically perform divisions at a constant rate. This model including cell division exhibits a slower decay of density, and an overall density profile that is consistent with our experimental observations (Fig. 3 D, 4 D). This also suggests that divisions play an important role in the experiment by maintaining a high density of the cell layer. This prevents the density from decreasing too quickly, in which case cells would not interact significantly, further supporting the important role of cell proliferation in collective cell spreading phenomena.

Having included cell division, we find that our model captures other key features of the experimentally observed dynamics. Importantly, we observe that the model predicts a peak in the radial velocity which emerges at the periphery of the colony (Fig. 4 E, F), similar to experiments (Fig. 3 E, F). This peak in radial velocity on a time-scale of the order of the persistence time of the cells corresponds to the outward diffusive flux expected for a collection of self-propelled particles [45, 74]. Specifically, upon removal of the confinement, cells at the boundary of the cluster are repelled by the bulk of the cluster, leading to a re-orientation of their movement in an outward direction. This causes the initial increase of the average radial velocity, which is followed by a decreasing trend due to the randomization of movement once the cluster has spread significantly (Fig. 4 G i). Furthermore, our model reproduces the gradual increase of the spreading radius (Fig. 4 H i), and a positive cross-correlation of velocity fluctuations indicating short-ranged alignment of cell movement (Fig. 4 I i). Finally, our model correctly predicts a reduction in the radial velocity for lower cell densities, as we observed

experimentally (Fig. 3 E). Taken together, these results demonstrate that our cell cluster experiments exhibit the behavior expected for a collection of active particles with interactions. In the experiment, the interactions between cells are known to be controlled by transmembrane proteins, including E- and N-Cadherins [46, 75], whose role we seek to elucidate in the next section.

2.3.4 Effect of blocking antibody treatment on E- and N-Cadherin gene and protein expression

To investigate the role of E- and N-Cadherin adherens junctions in collective cell migration, we inhibit their function using either E- or N-Cadherin blocking antibodies at different concentrations. To assess the effect of E-Cadherin blocking antibody on the different cadherin gene expression levels, we perform qPCR for E- and N- Cadherin genes at 1h and 5h after E-Cadherin blocking antibody treatment at the highest concentration tested (25 μg/ml). The qPCR serves as a short-term indicator of compensatory reactions of the cells upon functional blocking of an adhesion molecule in the crucial 5h time window after activation. This 5h timepoint coincides with the peak spreading velocities in the control condition and is therefore of particular interest. We find a significant upregulation of the E-cadherin gene expression after 5 hours compared to control (Fig. 5 A i). This increase can be considered as a compensatory mechanism of the cell to normalize its E-Cadherin functionality after the antibody-mediated blockage. Furthermore, the same treatment results in an early slight upregulation followed by significant downregulation of N-cadherin gene expression at 5h (Fig. 5 A ii). The latter result indicates that the upregulated E-Cadherin blocks the expression of N-cadherin [76, 77] , which may correspond to a known phenomenon called cadherin switching (extensively reviewed by Loh et al. [29]). Moreover, using Western Blot (WB), we evaluate the effect of E- or N-blocking antibody on E-Cadherin protein levels, as WB provides a longer time-scale endpoint image of the blocking effect on the total E-Cadherin levels. Here, we observe a significant downregulation of E-Cadherin at 24h after treatment with the E-Cadherin blocking antibody, verifying the antibody functionality. E-Cadherin is also downregulated after

N-Cadherin blocking antibody treatment (Fig. 5 B), which further implies the presence of a cadherin switching effect. Specifically, the N-Cadherin blocking antibody could transiently increase the gene expression of N-Cadherin, as a compensatory mechanism, which in turn could represses E-Cadherin expression. Interestingly, for E-Cadherin in the control (untreated) condition, we detect multiple shorter bands rather than one band of 130-135 kDa which is the normal size of the protein. The observed bands were a size of ~120 kDa, 95 kDa and 55 kDa (as shown in Supplementary Figure 3, respectively). Such deviations from the 135 kDa range, involving predominantly a soluble 80 kDa species [78] [79] [80] as well as 97 kDa [81], 48 kDa [82] and 23 kDa [83] fragments are common in the literature and have been associated with the development of different cancer types [29] [84] [85]. Therefore, as E-Cadherin protein expression is known to be very limited [41] or non-existent [42, 43] in T24 cells, it is probable that the shorter E-Cadherin fragments we see are a result of protein degradation.

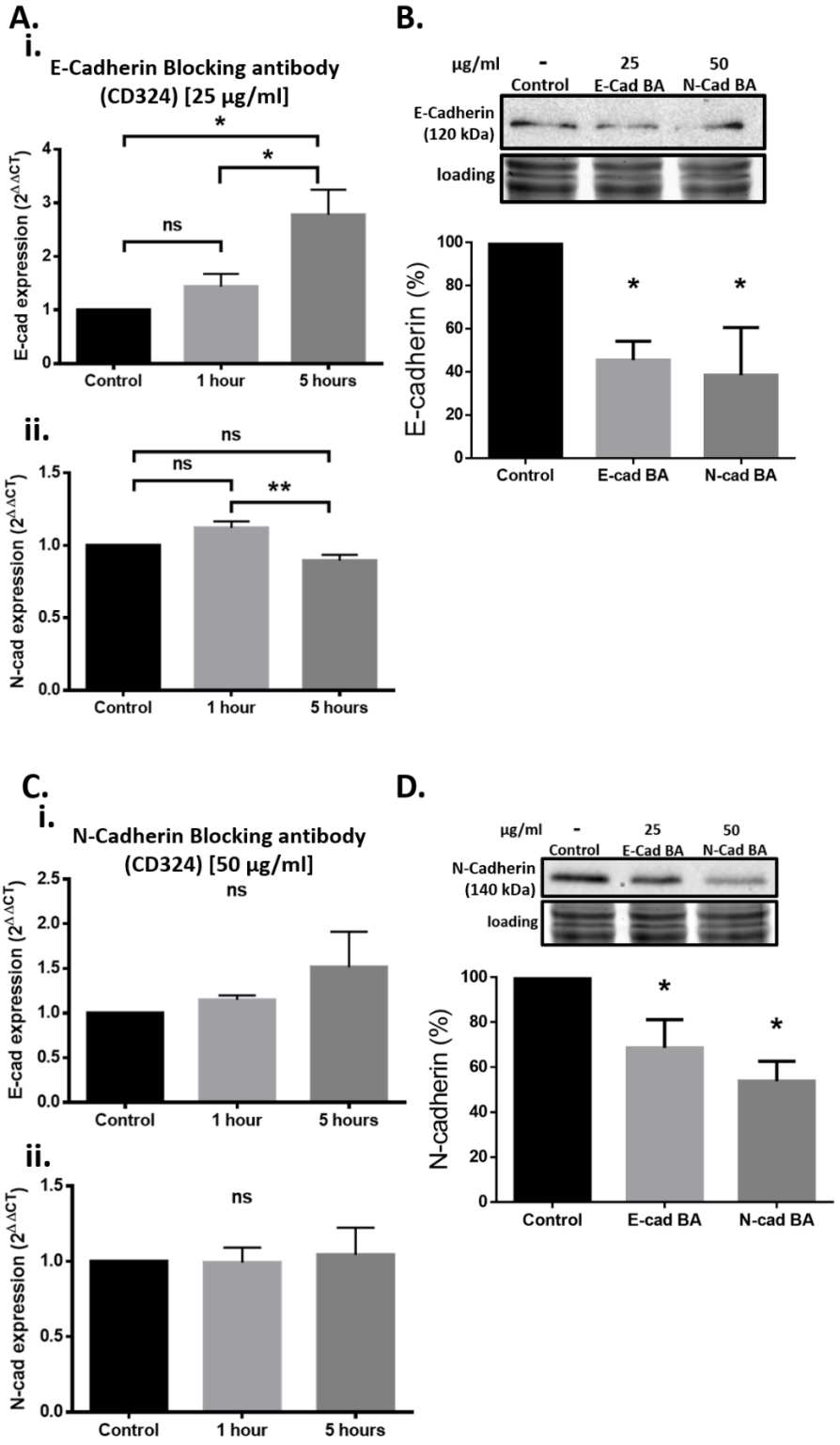

Figure 5: Effect of blocking antibody treatment on E- and N-Cadherin gene and protein expression

A) Quantitative PCR analysis of (i) E- and (ii) N-Cadherin gene expression in untreated (control) or treated T24 cells with E- blocking antibody for 1 and 5 hours, respectively. E-Cadherin blocking antibody treatment at the highest concentration tested (25um/ml) resulted in a significant upregulation of the E-

Cadherin gene expression after 5 hours compared to control (mean diff. ± SE= 1.8± 0.43, p=0.01). Furthermore, the same treatment resulted in a significant downregulation of N-Cadherin gene expression at the same timepoint compared to the 1h timepoint, indicating a cadherin-switching effect (mean diff. ± SE= 0.23, ±0.05, p=0.009). B) Quantitative Western Blot analysis of E- cadherin protein levels in untreated (control) or treated T24 cells with 25μg/ml E-Cadherin or 50μg/ml N-Cadherin blocking antibody after 24 hours. Both antibodies significantly reduced the levels of E-Cadherin after 24 hours (Control vs E-CAD BA: mean diff± SE=54.4±19.4, p=0.03; Control vs N-CAD BA: mean diff± SE= 61.5±19.4, p=0.03). C) Quantitative PCR analysis of (i) E- and (ii) N-Cadherin gene expression in untreated (control) or treated T24 cells with N- blocking antibody for 1 and 5 hours, respectively. N-Cadherin blocking antibody treatment at the second highest concentration tested (50 μg/ml) resulted in a non-significant upregulation of N- and E-Cadherin gene expression at 5h compared to control (N-Cadherin: mean diff ± SE= 0.05± 0.17, p=0.96; E-Cadherin: mean diff ± SE= 0.52± 0.33, p=0.32). D) Quantitative Western Blot analysis of N-Cadherin protein levels in untreated (control) or treated T24 cells with 25μg/ml E-Cadherin or 50μg/ml N-Cadherin blocking antibody after 24 hours. Both antibodies significantly reduced the levels of N-Cadherin after 24 hours (Control vs E-CAD BA: mean diff± SE=31.4±12.5, p=0.02; Control vs N-CAD BA: mean diff± SE= 53.8±12.5, p=0.02). Untreated cells were used for data normalization. One representative Western blot is shown per condition including a total protein loading control. Whole Western blots are shown in supplementary Figure 3. Statistical analysis was performed using 1-way ANOVA followed by Tukey's multiple comparisons (qPCR) or Sidak's multiple comparisons (WB) test; $p< 0.05$ (*), $p< 0.01$ (**); n = 3 (triplicates).

We then investigate the effect of N-Cadherin blocking antibody on cadherin gene expression levels, by performing qPCR for E- and N- Cadherin genes 1h and 5h after N-Cadherin blocking antibody treatment at the second highest concentration tested (50 μg/ml). In that case, a slight tendency towards upregulation of E-Cadherin gene expression is observed at 5h compared to control (Fig 5 C i), while the N-Cadherin expression levels were not significantly different from untreated cells (Fig. 5 C ii). This lack of significance could result from the fact that in T24 cells, the presence of N-Cadherin is much higher compared to E-Cadherin [41] and thus a higher concentration of blocking antibody would be required for a stronger effect. However, we observe the clear long-term influence of E- or N- blocking antibody on N-Cadherin protein levels by WB where we identify a significant downregulation of N-Cadherin protein levels at 24h after E- and N- Cadherin blocking antibody treatment (Fig. 5 D). Therefore, we conclude that treatment with either E- or N- cadherin blocking antibody starts with a transient upregulation in the corresponding cadherin gene expression which in turn leads to activation

of the cadherin switching mechanism that results in the downregulation of the opposite cadherin. This result is further verified by the WB results, where E- or N- cadherin protein levels are significantly downregulated when cells are treated with opposite blocking antibody over the long-term 24h timepoint. With regards to the WB-detected N-Cadherin bands in the untreated condition, a clear band at the expected size (140kDa) is always observed, suggesting that there was no apparent degradation or soluble form as was the case for E-Cadherin. This is not surprising, as N-Cadherin is the predominant and fully functional cadherin in the T24 cell line [41, 86, 87]. In summary, these findings verify that (i) there is a low gene and protein expression of functional (membrane-bound) E-Cadherin in our T24 cells (Supplementary Figure 3 C, D) and that (ii) besides the direct blocking effect, there is an 'off target' blocking effect, where the continuous overexpression of the cadherin being directly blocked leads to a downregulation of the opposite cadherin due to cadherin switching.

To visualize the effect of blocking antibody treatment on E- and N-Cadherin junctions, we performed immunofluorescence stainings of colonies at the 5- and 24 hour-timepoints (Fig. 6). Upon E-Cadherin blocking, we observe an evident reduction in the fluorescence intensity of E-Cadherin staining at 24h. This shows that the E-Cadherin blocking antibody reduced the amount of functional E-Cadherin in the cells 24h post-treatment, in agreement with our WB results. The fluorescence intensity of N-Cadherin staining was not visibly reduced by addition of N-Cadherin blocking antibody. Although in the WB experiments we see a clear reduction in the levels of N-Cadherin as a result of N-Cadherin blocking antibody treatment, the N-Cadherin staining was probably not sensitive enough to reflect this effect as a decrease in fluorescence intensity. This suggests that, as T24 cells express much higher of N-Cadherin compared to E-Cadherin [41], a higher concentration of N-Cadherin blocking antibody may be required to induce a visible reduction in the fluorescence intensity. Interestingly, both blocking antibodies resulted in larger gaps between the cells, and slightly elongated cell phenotypes.

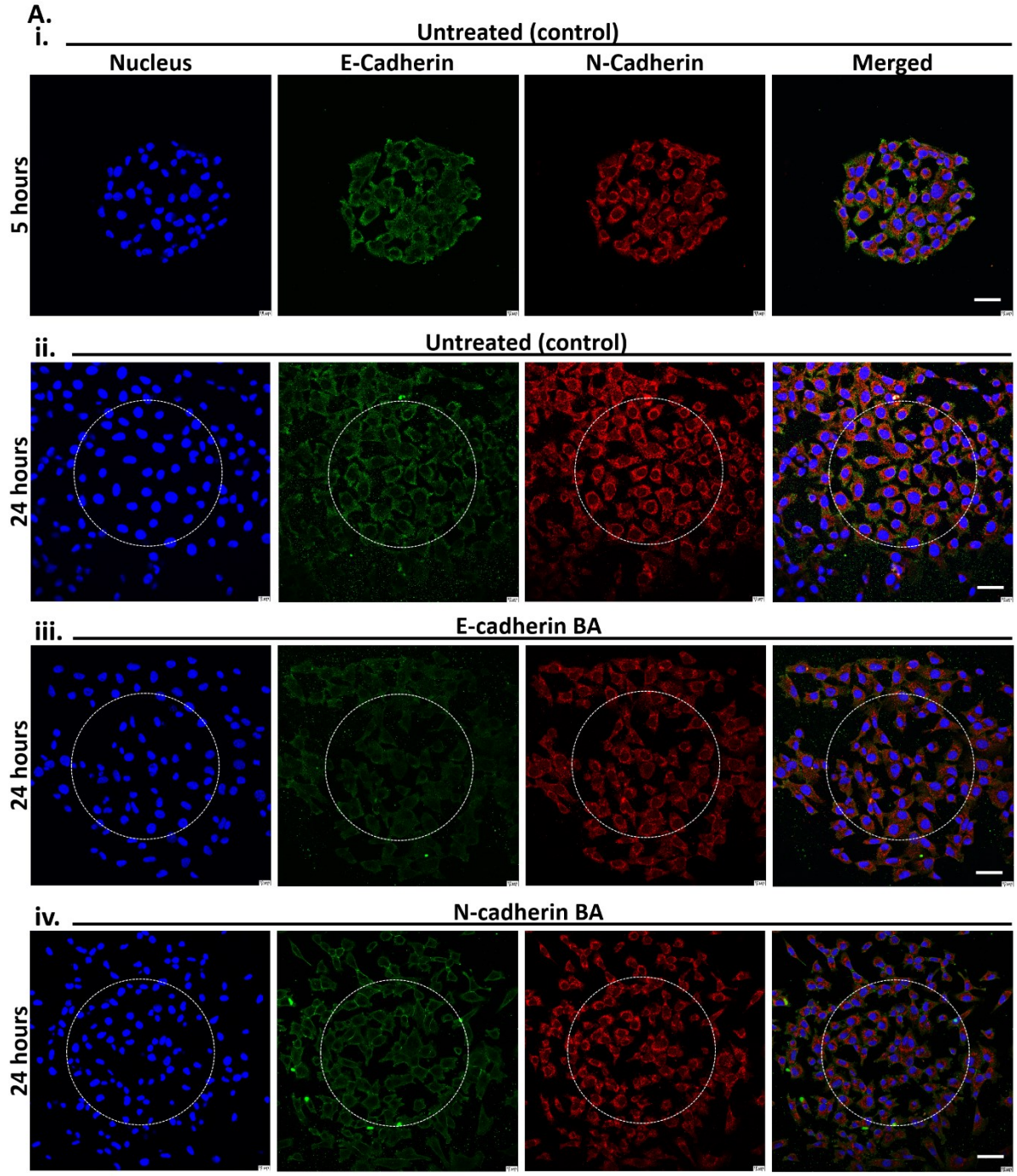

Figure 6: E-and N-Cadherin immunofluorescence staining of untreated (control) and E- or N-Cadherin BA treated colonies

Representative confocal images of untreated (control) colonies co-stained against E-and N-Cadherin (green and red, respectively), together with nuclear labeling (blue), at 5 hours (i) and 24h (ii) after surface activation. iii) Cadherin-stained colonies upon E-Cadherin blocking antibody treatment (25 μg/ml) at 24h after surface activation, iv) Cadherin stained colonies upon N-Cadherin blocking antibody treatment (100 μg/ml) at 24h after surface activation. Dashed circles show the original confinement of the clusters. Merge is shown on the right column. Scale bar: 50 μm.

2.3.5 Disrupting E- and N-Cadherin junctions decreases speed of collective spreading

Having quantified the E- and N-Cadherin expression upon different levels of E- or N-Cadherin blocking, we move on to analyzing the collective migration behavior in these conditions. First, we find that a low concentration of E-Cadherin blocking antibody (10 μg/ml) does not significantly affect migration behaviour such as the colony spreading represented by density profiles and radial velocities of the cells (Fig. 7 A, B i, C i, D i, D ii and Supplementary Movie S4). However, blocking E-Cadherin at a higher concentration of antibody (25 μg/ml) reduces the average spreading of the colonies (Fig. 7 B ii, C ii, D ii) as well as the average radial velocity of the cells (Fig. 7 D i). Similarly, increasing concentrations of N-cadherin blocking antibody leads to reduced average colony spreading and radial velocities, with the highest one (100 μg/ml) having the strongest effect (Fig. 8 A, B, C, D i, D ii and Supplementary Movie S5). In contrast, we find that the average velocity of single migrating cells in experiments with sparsely seeded cells is not significantly affected by the addition of either blocking antibody, for the whole duration of the experiment (Supplementary Figure 1). Furthermore, the proliferation of cells is similar across all conditions (Supplementary Figure 2). These observations suggest that the change in spreading behaviour upon Cadherin blocking is not mediated by changes in the behaviour of single cells or their proliferation, but is mainly caused by the reduction in cell-cell interactions and is thereby a collective effect.

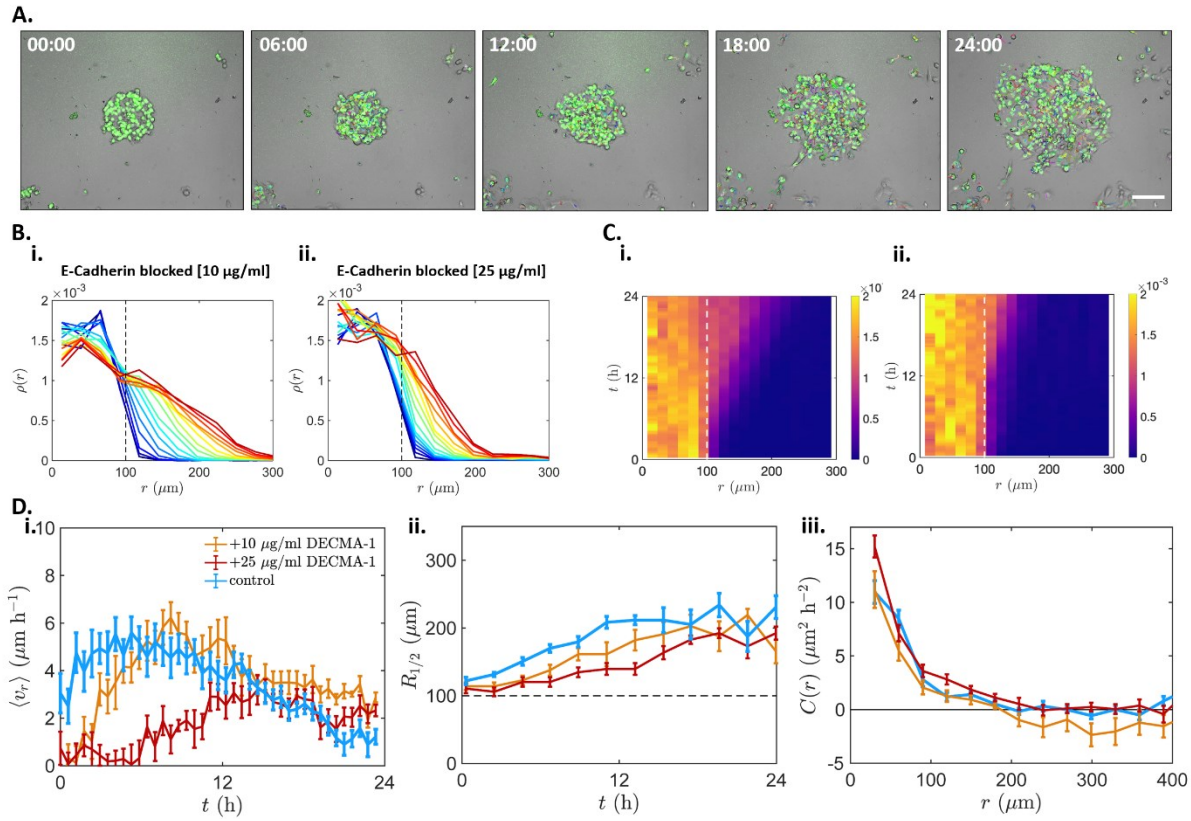

Figure 7: Evolution of cell density profile, radial velocities and average distance of T24 cells treated with increasing concentrations of E-Cadherin blocking antibody

A) Time-lapse overlay of bright-field and fluorescence microscopy images with cell tracks of the 25 µg/ml E-Cadherin blocking, showing the T24 cell migration with 6h intervals from 0h to 24h after surface activation. B) Evolution of the density profiles over 24 hours (blue to red) plotted as the mean of all colonies per condition for T24 cells treated with (i) 10 µg/ml or (ii) 25 µg/ml E-Cadherin blocking antibody. All curves are separated by 1 h intervals. C) Kymographs of the cell density evolution, for T24 cells treated with (i) 10µg/ml and (ii) 25 µg/ml E-Cadherin blocking antibody. D) i) Mean radial velocity (u_r) over time (average of all colonies per condition). The control condition exhibited a direct increase in radial velocity, peaking around 5h after surface activation (blue). 10 µg/ml E-Cadherin blocking antibody slowed down this increase in radial speed, which peaked at 8h (orange). The highest concentration of blocking antibody (25 µg/ml) resulted in even lower radial velocity that did not reach the initial peaks exhibited in the other conditions (red). ii) Average distance where density has decayed to half of its value in the center of the original confinement (i.e. at r=0). The distance was the highest over time in the control condition and decreased with increasing concentrations of E-Cadherin blocking antibody. iii) Cross correlation of velocity fluctuations showing no significant differences between conditions. Error bars: SEM; $n_{control}$= 12, n_{10ECAD}= 13, n_{25ECAD}= 8.

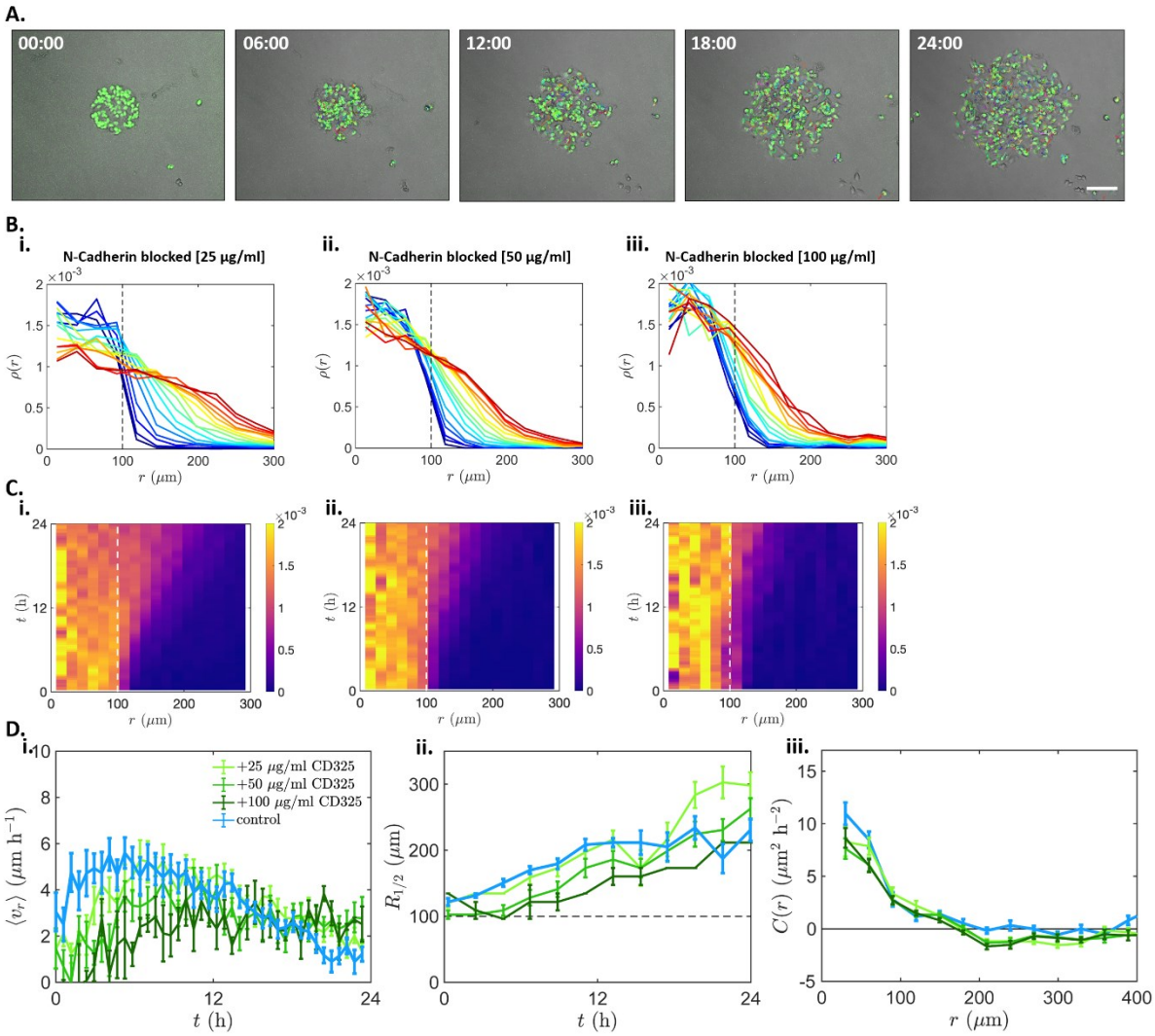

Figure 8: Evolution of cell density profile, radial velocities and average distance of T24 cells treated with increasing concentrations of N-Cadherin blocking antibody

A) Time-lapse overlay of bright-field and fluorescence microscopy images with cell tracks of the 100 µg/ml N-Cadherin blocking, showing the T24 cell migration with 6h intervals from 0h to 24h after surface activation. B) Evolution of the density profiles over 24 hours (blue to red) plotted as the mean of all colonies per condition for T24 cells treated with (i) 25 µg/ml, (ii) 50 µg/ml or (iii) 100 µg/ml N-Cadherin blocking antibody. All curves are separated by 1 h intervals. C) Kymographs of the cell density evolution, for T24 cells treated with (i) 25 µg/ml, (ii) 50 µg/ml or (iii) 100 µg/ml N-Cadherin blocking antibody. D) i) Mean radial velocity (u_r) over time (average of all colonies per condition). The control condition exhibited a direct increase in radial velocity, peaking around 5h after surface activation (blue). Increasing concentrations of N-Cadherin blocking antibody reduced this increase in radial speed, with the highest reduction observed in the 100µg/ml treated cells (dark green). ii) Average distance where density has decayed to half of its value in the center of the original confinement (i.e. at r=0). The distance was the highest in the control condition and decreased with increasing concentrations of N-Cadherin blocking antibody up to 11h. After this timepoint, the 25 µg/ml N-Cadherin blocking antibody treated

colonies surpassed the control ones. iii) Cross correlation of velocity fluctuations showing no significant differences between conditions. Error bars: SEM; $n_{control}$= 12, n_{25NCAD}= 8, n_{50NCAD}= 6 $n_{100NCAD}$= 3.

To identify a possible change in cell-cell interactions due to cadherin blocking, we calculate the cross-correlation functions of velocity fluctuations between pairs of cells, which quantifies how similar cellular velocities are as a function of their distance from one another (Methods Section and Fig. 7 D iii and 8 D iii). As expected, in the control condition, we find that cells tend to align their direction of motion with neighbouring cells, but exhibit no correlations at long distances. Unexpectedly, however, we find that all observed experimental conditions have a similar cross-correlation function. This indicates that while we expect a change in cell-cell interactions to be responsible for the change in spreading behaviour, this change does not directly affect the degree of velocity alignment, quantified through the velocity cross-correlation. In a following section, we will turn to a theoretical model for a possible explanation of these observations.

To summarize our experimental findings, we find that by partially blocking either E- or N-cadherin adherens junctions, the collective spreading behaviour of initially confined clusters of T24 cells becomes less efficient. This suggests that cell-cell contacts are important for coordinated migration, possibly by promoting cell-cell interactions. This result is in agreement with earlier reports showing that preventing cells from forming stable cell-cell contacts resulted in uncoordinated and random cell movement [88], leading to significantly lower migration velocities [89]. In contrast to other studies observing no E-Cadherin expression in T24 cells, we detect its presence (120 kDa) among other fragmented species of the protein. Furthermore, we show that as a type III carcinogenic line, T24 cells exhibit an increased N-Cadherin vs E-Cadherin expression ratio (3/1 as shown in Supplementary Figure 3 C, D), characteristic for EMT [29]. Interestingly, we find that the limited E-Cadherin expression is still important for the efficiency of the collective migration, as is the more predominantly expressed N-Cadherin. Therefore, the interplay between E- and N-Cadherin in T24 cells points to a

crucial balance in cell-cell contacts that seems to be important for collective migration. In the next section, we use our minimal active particle model to elucidate the nature of these interactions and how they influence the cell spreading behavior.

2.3.6 Varying cell-cell interactions in a minimal active particle model captures the effects of Cadherin blocking

To investigate how changes in cell-cell interactions affect the spreading behavior in our model, we first vary the strength of contact inhibition of locomotion (CIL). We implement CIL as an angular repulsion that acts as a torque on cells undergoing a contact, with strength α, similar to previous work [45] (see Fig. 4 A and Methods Section). We find that decreasing α, corresponding to weaker CIL, leads to a reduction in radial velocity, spreading, and cross-correlations (Fig. 4 G i, H i, I i). Thus, while the first two findings are in line with the changes in behavior upon cadherin inhibition in the experiment, the change in cross-correlation is not observed in the experiment. In contrast, reducing the strength of the repulsive interactions between particles leads to a reduction of the radial velocity peak and the overall spreading, while keeping the cross-correlations constant (Fig. 4 G ii, H ii, I ii) - similar to what we observed experimentally upon blocking E- or N-Cadherin-mediated intercellular contacts (Fig. 7 B ii, D and 8 B ii-iii, D). These results are robust over a wide range of parameters in the model (Supplementary Figures 5, 6). These observations suggest that disrupting cell-cell junctions through E and N-Cadherin blocking has an effect akin to reducing excluded volume interactions between cells.

The reduced spreading for weaker CIL and weaker repulsive interactions can be understood intuitively. Firstly, CIL interactions ensure that cells at the cluster boundary do not cross paths, leading to outward alignment of their velocities. In fact, in this setup, CIL has an effect very similar to velocity alignment interactions: an alternative model with velocity alignment instead of CIL produces very similar results (Supplementary Figure 4), highlighting the similarity of these two interaction types in this setup. Secondly, repulsion ensures that boundary cells are

repelled by the bulk of the cluster, which further rectifies their motion into a radially outward direction. Thus, both stronger CIL and stronger repulsive interactions lead to faster, more efficient spreading dynamics (Fig. 4 G, H).

However, we can distinguish the two types of interaction through the cross-correlation of cell velocities: this quantity serves as a good indicator for changes in CIL-behavior. Specifically, changing repulsive interactions has no significant effect on the correlation function, since it is a position-dependent interaction (Fig. 4 I ii). In contrast, CIL is a velocity-dependent interaction, and its strength therefore controls the magnitude of the velocity cross-correlations (Fig. 4 I i). Therefore, our results suggest that rather than reducing the strength of CIL-behavior, disrupting cell-cell junctions through E- and N-Cadherin blocking has an effect akin to reducing repulsive interactions between cells.

To further test this finding experimentally, we assess cell polarization using cytoskeletal staining as previously described [49]. First, we show that the number of cells polarized towards cell-cell contacts is not significantly different from the number of cells polarized away from cell-cell contacts (mean diff $_{away\text{-}towards}$=13 ± 6.5 p=0.07, Supplementary Figure 7). Furthermore, we performed the same quantification for the E- and N-Cadherin blocking conditions and found that blocking of either cadherin type did not induce significant changes in this type of cell polarization behaviour compared to the control condition (1-way ANOVA for the ratio [perc. cells polarized away / perc. cells polarized towards]: F= 2.4; p=0.14, Supplementary Figure 7).

Taken together, our experimental and modeling results show that cell-cell interactions are key drivers of tissue spreading in this setup, and that disrupting cell-cell junctions through E- and N-Cadherin blocking has an effect akin to reducing repulsive interactions between cells. Specifically, the congruity between experiment and model suggests that both E- and N-Cadherin-mediated intercellular contacts create repulsive events via excluded volume interactions that are critical for the efficient cell spreading during collective migration. This

effect could be due to cadherins 'sharpening' cell boundaries by for example regulating cell shape, improving cell-cell recognition, or increasing interfacial tension. Indeed, both E- and N-cadherin have been shown to determine inter-cellular interfacial tension in the developing epithelium [46, 90, 91]. Our results challenge the prevalent view in the literature that E- and N- cadherin junctions are essential for CIL [92-97]. However, our findings are not entirely unexpected, as there are other studies showing an opposing role between the different cadherin-types in CIL, with E-Cadherin inhibiting CIL and N-Cadherin promoting CIL, in cells undergoing EMT to become migratory [98, 99]. Therefore, the role of cadherins in CIL during collective spreading may differ between cell lines (non-cancerous vs cancerous, epithelial vs mesenchymal). These results are also in qualitative agreement with previous work where the interactions of colliding pairs of cells were inferred directly from observed trajectories [55]. Specifically, it was shown that the cancerous MDA-MB-231 cell line exhibits less repulsive interactions than the non-malignant MCF10A cell line, which is known exhibit higher E-cadherin expression than MDA-MB-231 cells [100, 101]. Our work therefore further supports the important role of cadherin-mediated cell-cell interactions, and elucidates their role in collective cell migration.

2.4 Conclusion

This study provides new insight into the role of different cadherin junctions in the dynamics of collective cancer cell migration. In our setup, we find that the collective migration of T24 cancer cells is predominantly driven by stochastic single-cell migration with transient cell-cell contacts. We reveal that in this case, blocking E- or N-Cadherin in collectively migrating T24 cancer cells significantly reduces their spreading efficiency. The observed phenomenology is well captured by a biophysical model of stochastically migrating cells. Our model shows that cell proliferation as well as the excluded volume and Contact Inhibition of Locomotion interactions between cells drive tissue spreading in our setup. Our combined experimental

and theoretical results further indicate that disrupting E- and N-Cadherin-mediated intercellular contacts leads to a decrease in repulsive cell-cell interactions, which in turn reduces the spreading efficiency of the cell collective. Therefore, from a biomedical point of view, this study underscores the importance of E- and N-Cadherins as potential pharmacological targets in metastatic cancer research. Furthermore, our experimental setup design could be adapted for future research in the field, such as studying the impact of mechanical cell-cell communication on cell spreading on mechanically compliant substrates [102-104], or chemotactic cell spreading in external gradients [105, 106].

2.5 Supplementary Information

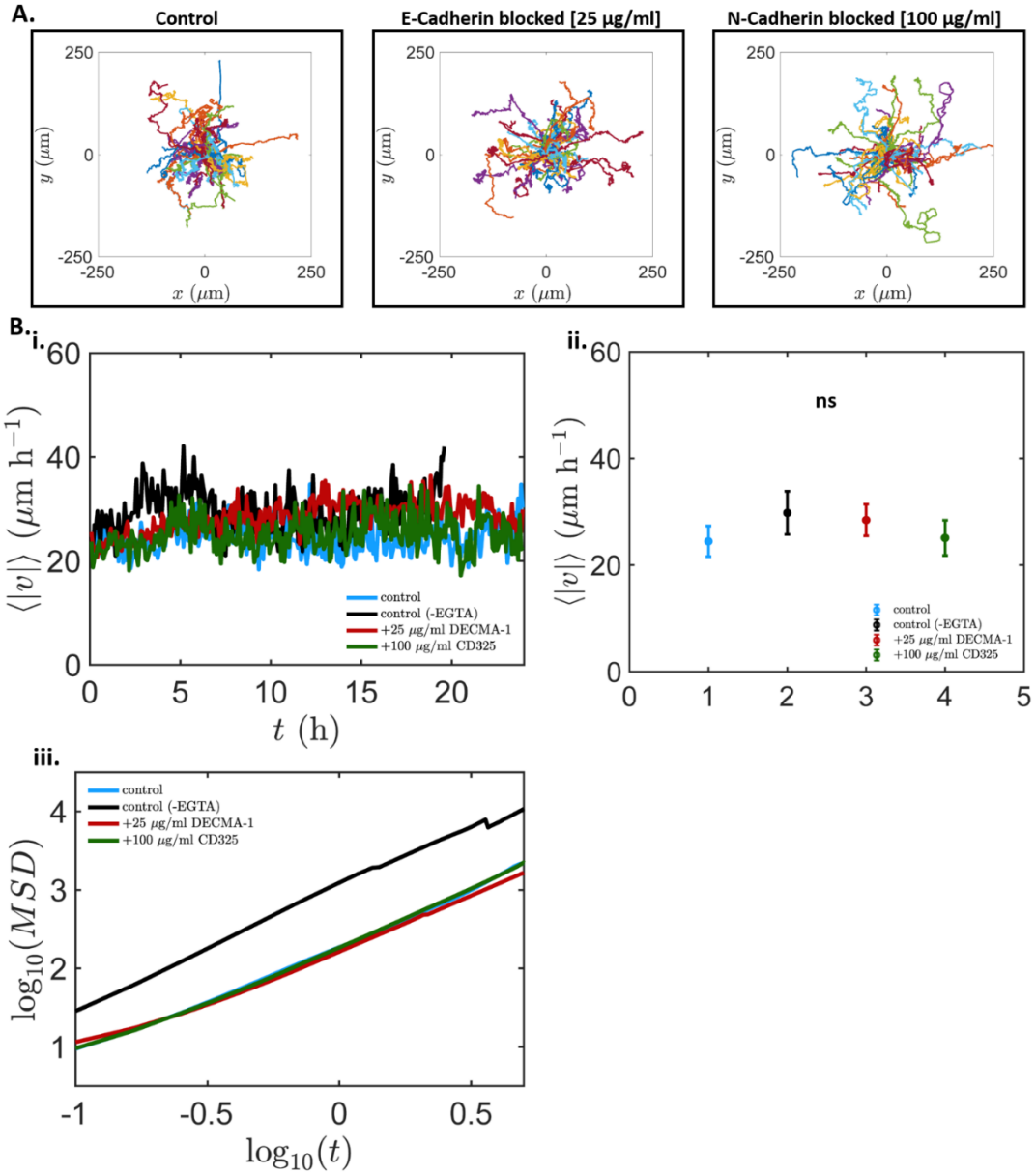

Supplementary Figure 1: Single cell trajectories, radial velocities and SEM for single T24 cell migration in the different blocking conditions

A) Single T24 cell trajectories in the control condition and at the highest blocking antibody concentration for each cadherin type. B) i) Mean radial velocity (u_r) over time and (ii) corresponding SEM graph showing no significant differences (1-way ANOVA, $p>0.05$) between averaged cell velocities of single cells for every condition. Average velocity of single cells was stable and was not affected by the addition of the different antibodies or EGTA pre-treatment. iii) Mean square displacement (MSD) plot showing all conditions having a 1.3 curve gradient.

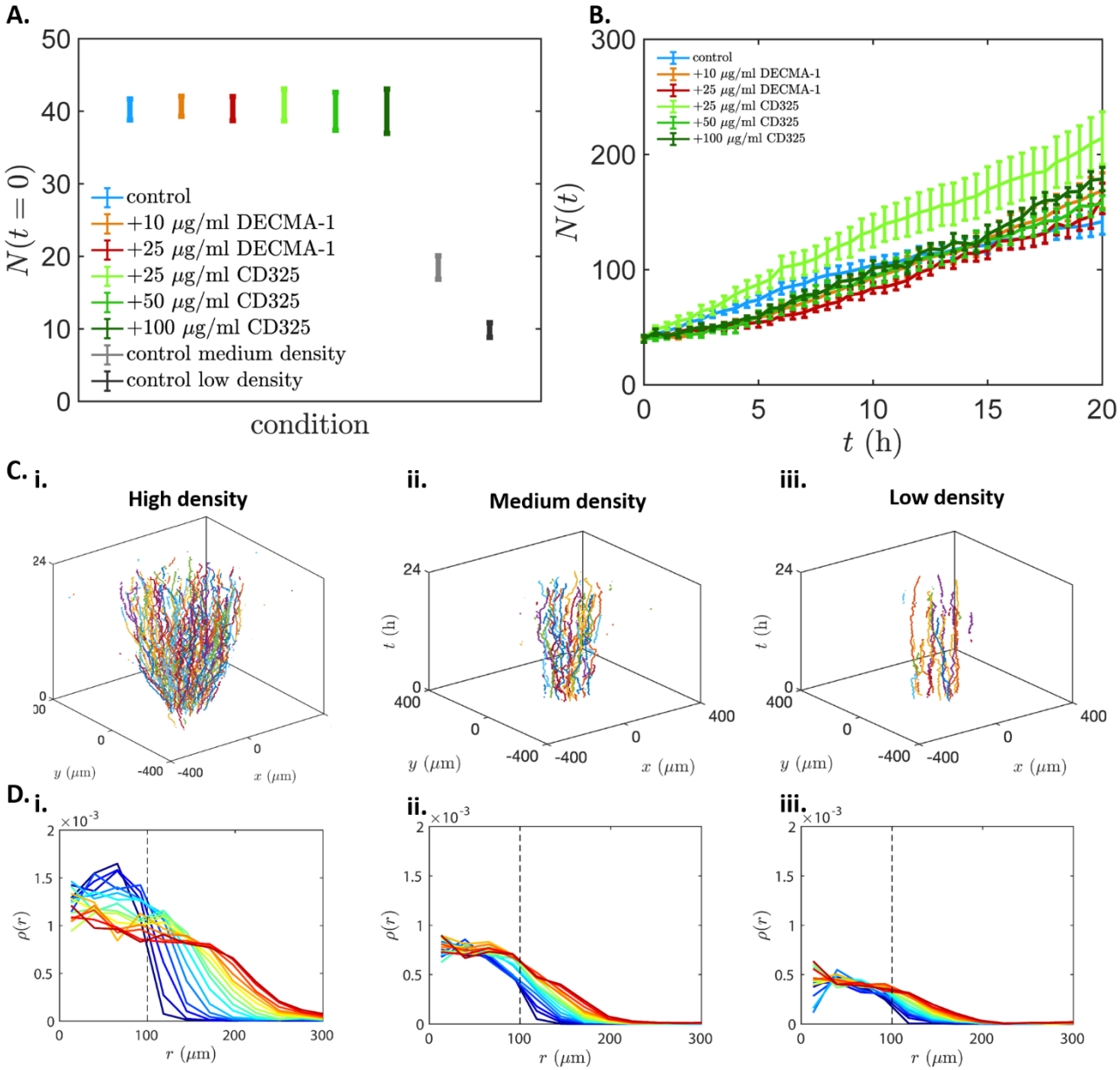

Supplementary Figure 2: Initial number of cells of each colony for every condition and T24 cell proliferation in the different blocking conditions, followed by space diagrams and evolution of density profiles for colonies with different cell densities

A) Number of cells (t=0) for each colony per condition, color-coded according to the colony's cell density. For every condition we ensured constant average initial cell density with an average cell number of ~40, except medium and low cell density control conditions. B) Cell proliferation shown as the average total number of cells of all colonies for each blocking condition. In all conditions, except the 25 μg/ml N-Cadherin blocking and the combination blocking, the proliferation rate was not affected by treatment with blocking antibodies. The cell number approximately doubles in 10h, corresponding to a division rate of 0.1 h^{-1} C) Space diagram of (i) a high cell density, (ii) a medium cell density and (iii) a low cell density colony spreading up to 24h after surface activation. D) Evolution of the density profiles of (i)

high cell density, (ii) medium cell density and (iii) low cell density colonies over time (blue to red) plotted as the mean of all colonies (n_{high}= 12, n_{medium}= 15, n_{low}= 12). All curves are separated by 1.5 h intervals.

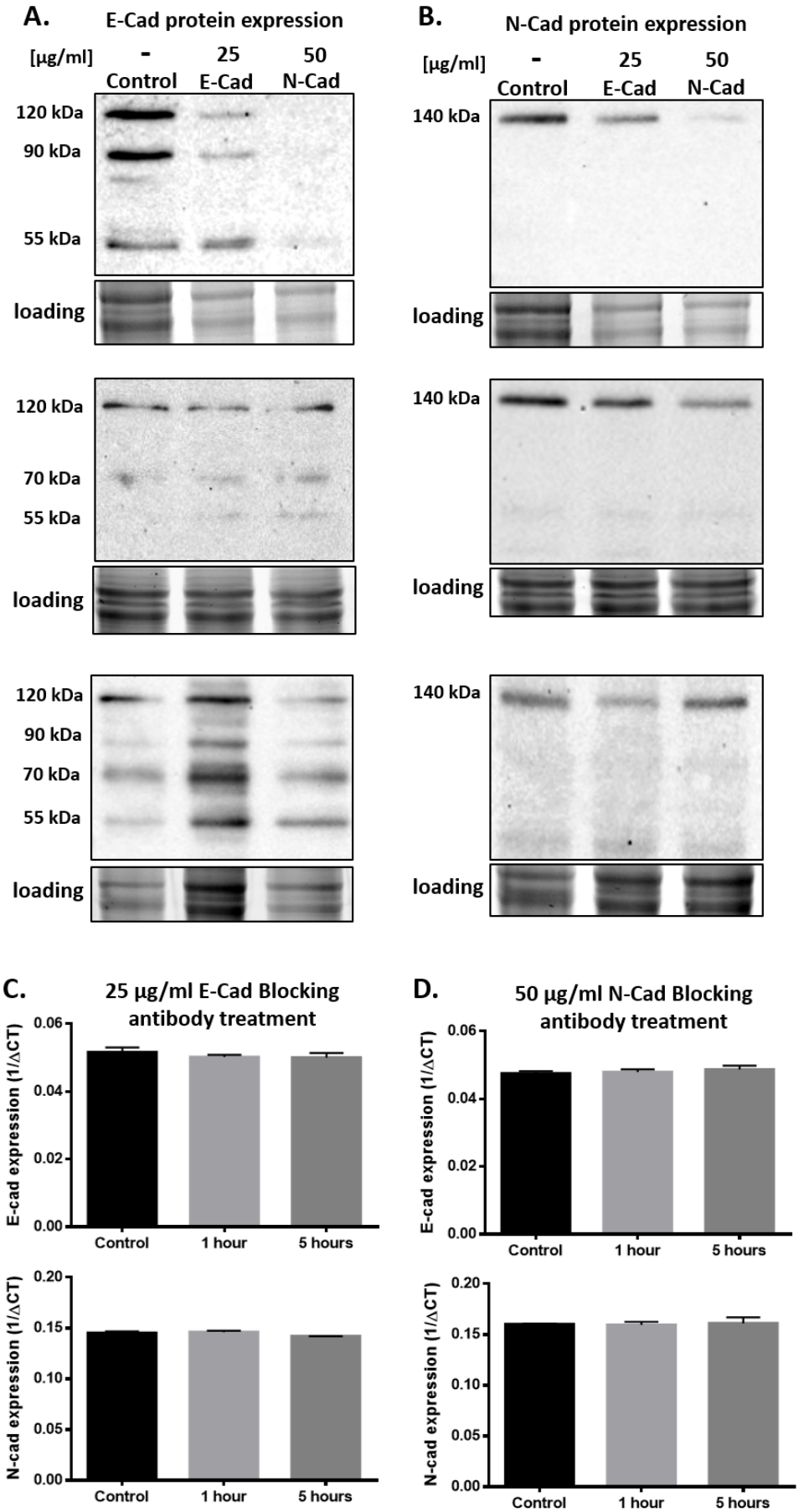
A.
E-Cad protein expression
[µg/ml]
-
25
50
Control
E-Cad
N-Cad
120 kDa
90 kDa
55 kDa
loading
120 kDa
70 kDa
55 kDa
loading
120 kDa
90 kDa
70 kDa
55 kDa
loading
B.
N-Cad protein expression
[µg/ml]
-
25
50
Control
E-Cad
N-Cad
140 kDa
loading
140 kDa
loading
140 kDa
loading
C.
25 µg/ml E-Cad Blocking antibody treatment
E-cad expression (1/ΔCT)
0.06
0.04
0.02
0.00
Control
1 hour
5 hours
N-cad expression (1/ΔCT)
0.20
0.15
0.10
0.05
0.00
Control
1 hour
5 hours
D.
50 µg/ml N-Cad Blocking antibody treatment
E-cad expression (1/ΔCT)
0.06
0.04
0.02
0.00
Control
1 hour
5 hours
N-cad expression (1/ΔCT)
0.20
0.15
0.10
0.05
0.00
Control
1 hour
5 hours

Supplementary Figure 3: Complete Western blot triplicates and qPCR results

A) E- cadherin protein levels in untreated (control) or treated T24 cells with 25μg/ml E-Cadherin or 50 μg/ml N-Cadherin blocking antibody after 24 hours. WB triplicates show the different band sizes occurring and the accompanying protein loading, with the 120kDa being the functional protein observed in all three WBs. B) N- cadherin protein levels in untreated (control) or treated T24 cells with 25 μg/ml E-Cadherin or 50μg/ml N-Cadherin blocking antibody after 24 hours. WB triplicates show the 140kDa band size occurring and the accompanying protein loading. In all cases, to calculate protein expression levels all band intensities were calibrated according to control using the loading band intensities. C) No significant differences in gene expression levels of E- and N-Cadherin at 1h and 5h upon 25μg/ml E-Cadherin blocking antibody treatment as determined by qPCR (E-Cadherin: 1-way ANOVA $F=0.54$, $p=0.61$; N-Cadherin: 1-way ANOVA $F= 3.5$, $p=0.097$). D) No significant differences in gene expression levels of E- and N-Cadherin at 1h and 5h upon 50μg/ml N-Cadherin blocking antibody treatment as determined by qPCR (E-Cadherin: 1-way ANOVA $F= 0.43$, $p=0.67$; N-Cadherin: 1-way ANOVA $F= 0.04$, $p=0.96$). In all cases the levels of N-Cadherin expression are ~3-fold higher than the levels of E-Cadherin expression.

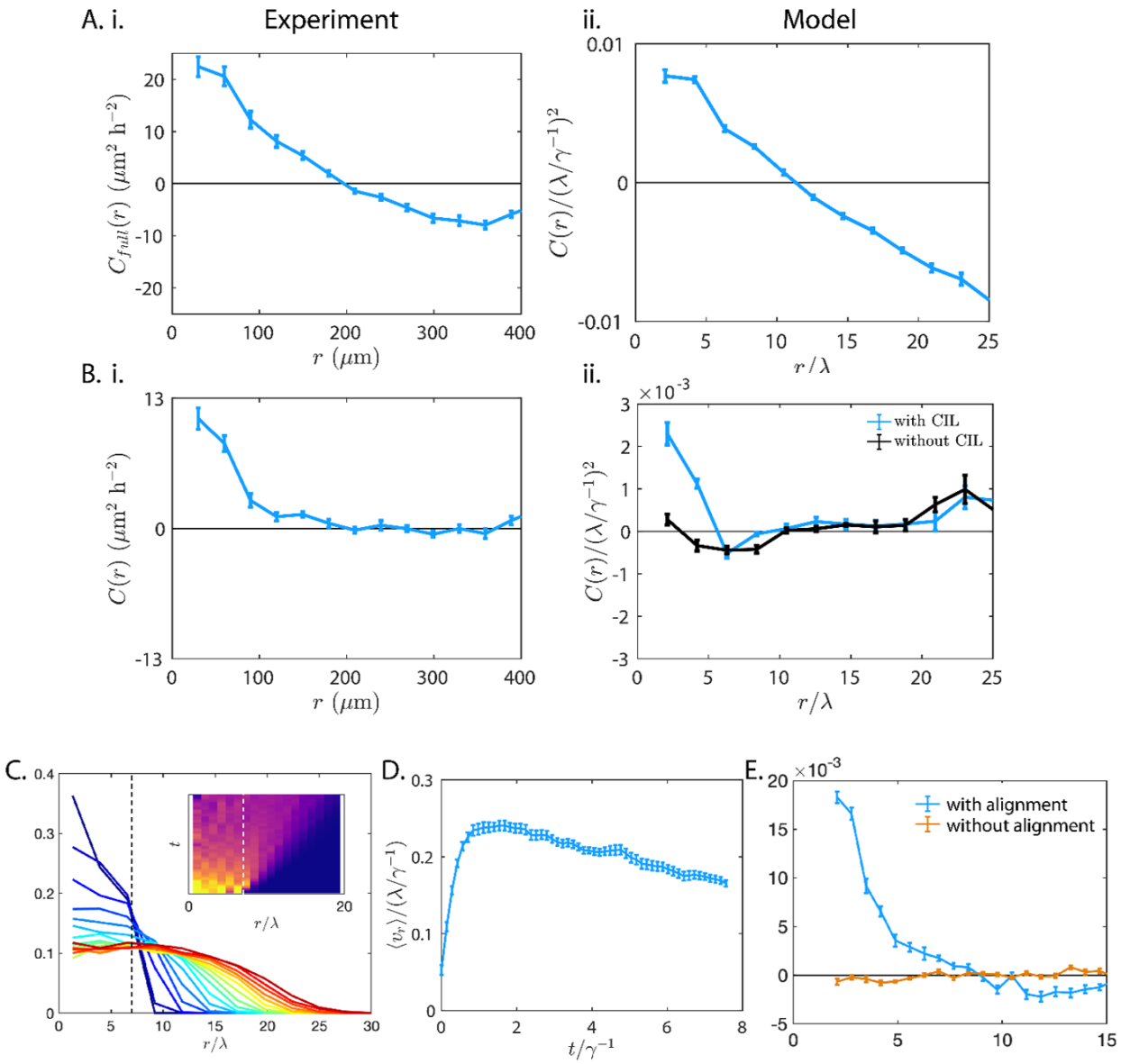

Supplementary Figure 4: Calculation of the spatial fluctuation velocity cross-correlation function and comparison to a model with velocity alignment interactions

A) Correlation function of the full velocities for (i) experiment and (ii) model with CIL. As expected, the correlation function is initially positive, corresponding to neighboring cells on average moving in the same direction. After a distance on the order of the initial confinement radius, the function turns negative, corresponding to cells on opposite ends of the cluster moving on average in opposite directions. B) Correlation function of the velocity fluctuations, where the overall dilatation of the cluster is subtracted. For the model, corresponding curves for a simulation with CIL (blue), and without CIL interactions (black) is shown. As expected, in both cases, the negative part of the correlation due to the overall dilatation of the cluster disappears and only simulations with CIL exhibit significant fluctuation velocity correlations. C)-E) Results for a model with velocity alignment instead of CIL interactions (Methods). C) Evolution of the density profile over time (blue to red). Inset: Kymograph of the cell density evolution. Dashed lines indicate the initial confinement radius. D) Mean radial velocity as a function of

time. E) Cross-correlation of velocity fluctuations, for a model with and without velocity alignment interactions. Error bars: SEM; n=30 for all panels.

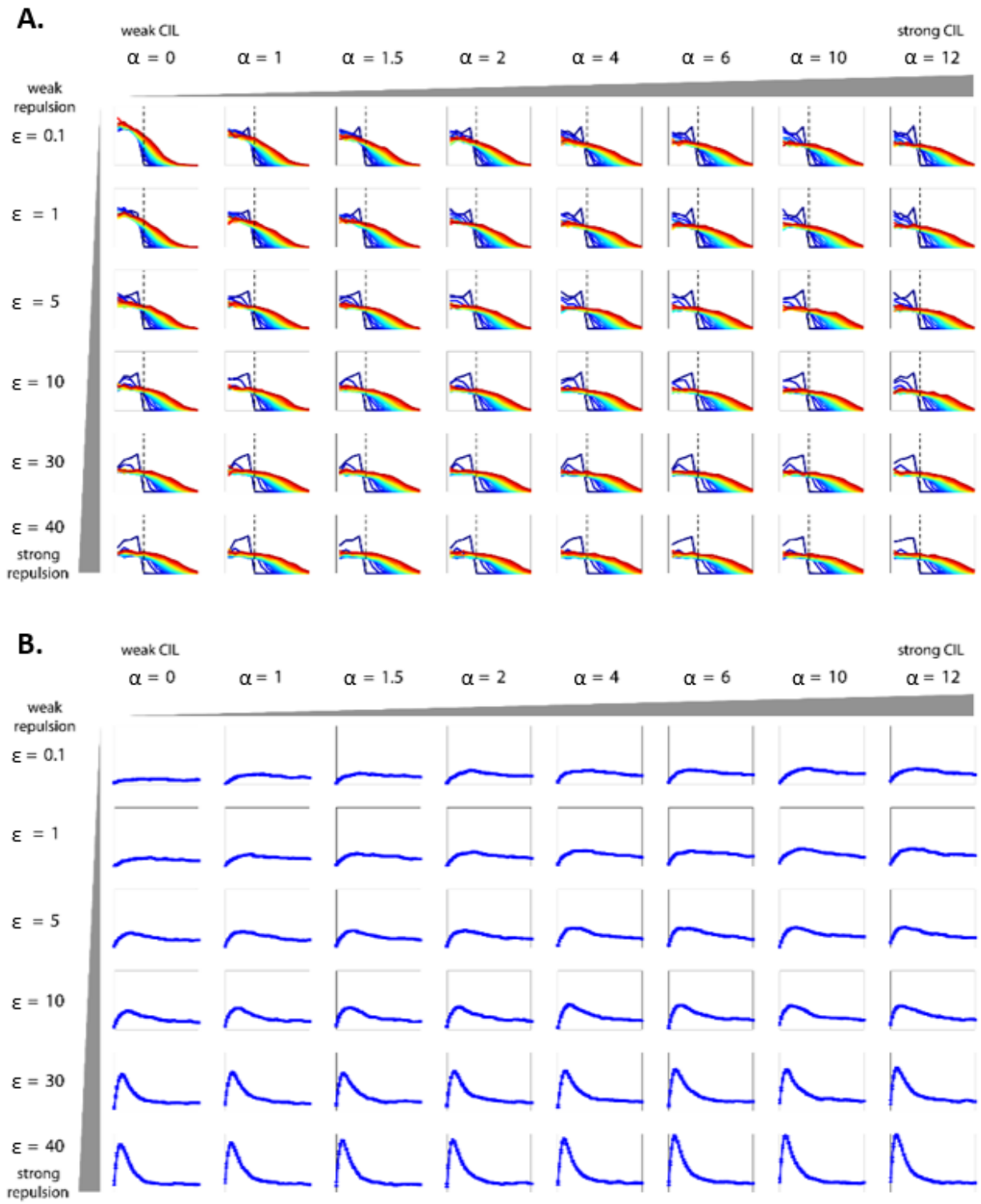

Supplementary Figure 5: Full parameter sweep: density profiles and radial velocity curves

A) Evolution of the density profile over time (blue to red) for all parameter combinations of repulsion strength ε and CIL interaction amplitude α, averaged over n=30 clusters per condition. The profiles exhibit further spreading for larger repulsions and larger CIL amplitudes. B) Mean radial velocity as a function of time for all parameter combinations of repulsion strength ε and CIL interaction amplitude α.

We generally observe larger radial velocity peaks for larger repulsions and larger CIL amplitudes. Error bars: SEM; n=30 for all panels.

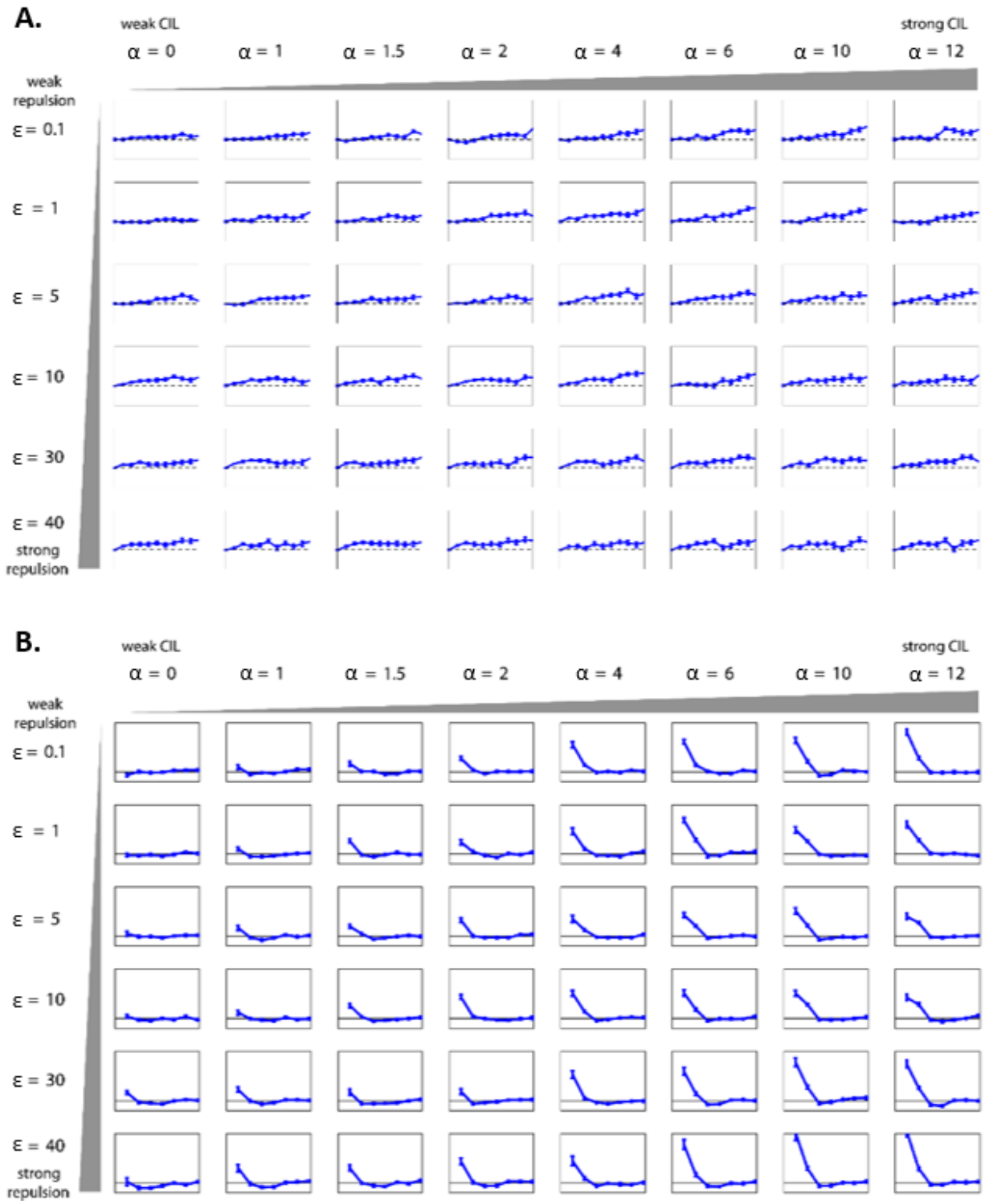

Supplementary Figure 6: Full parameter sweep: spreading radius and velocity fluctuation cross-correlation function

A) Average distance where density has decayed to half of its value in the center of the original confinement (i.e. at r=0) for all parameter combinations of repulsion strength ε and CIL interaction amplitude α. We observe larger spreading radii for larger repulsions and larger CIL amplitudes. Error bars: SEM; n=30 for all panels. B) Cross-correlation of velocity fluctuations for all parameter combinations of repulsion strength ε and CIL interaction amplitude α. We generally observe larger radial velocity peaks for larger repulsions and larger CIL amplitudes. Error bars: SEM; n=30 for all panels.

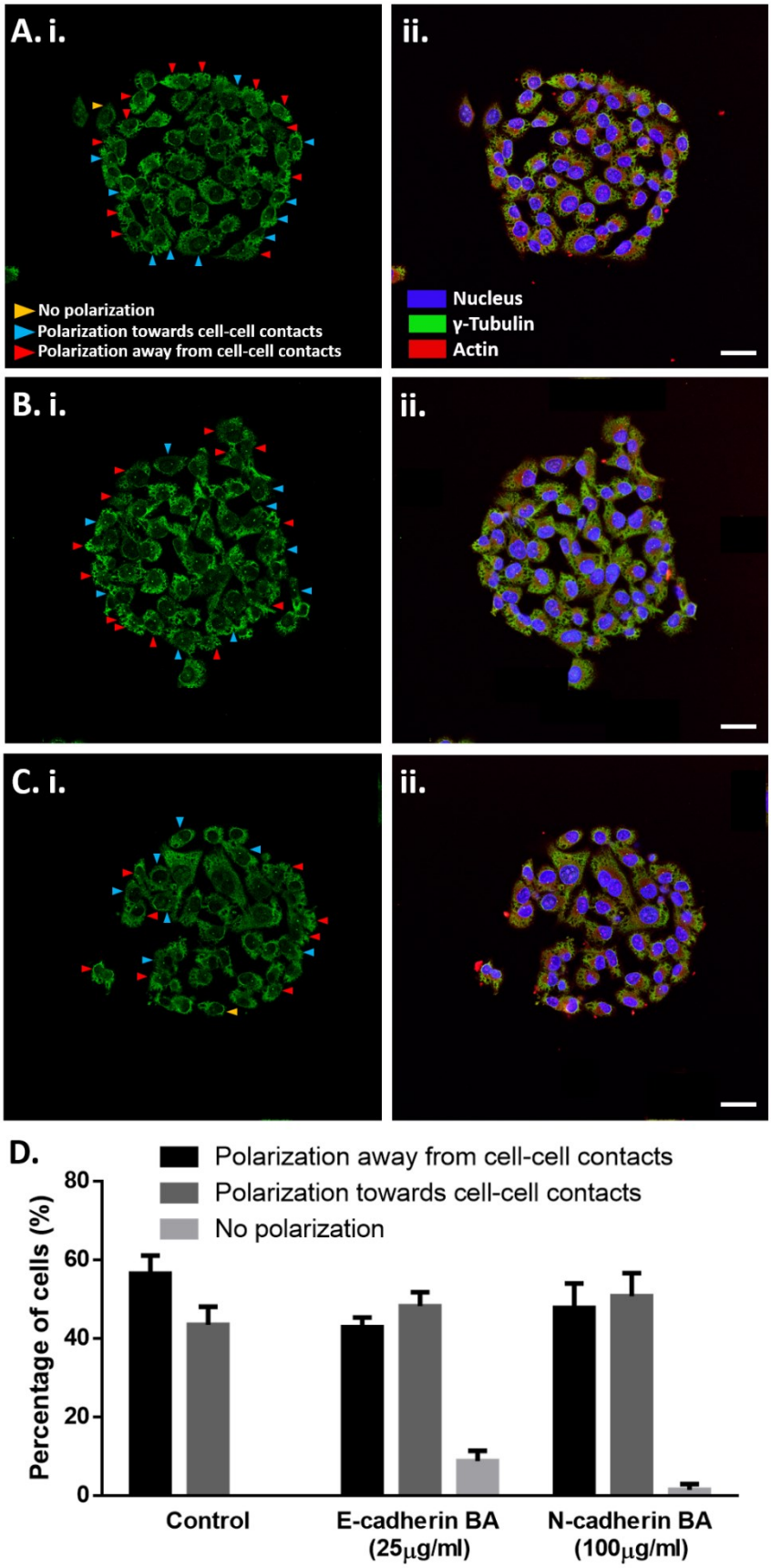
A. i.
ii.
No polarization
Polarization towards cell-cell contacts
Polarization away from cell-cell contacts
Nucleus
γ-Tubulin
Actin
B. i.
ii.
C. i.
ii.
D.
Polarization away from cell-cell contacts
Polarization towards cell-cell contacts
No polarization
Percentage of cells (%)
80
60
40
20
0
Control
E-cadherin BA (25μg/ml)
N-cadherin BA (100μg/ml)

Supplementary Figure 7: Polarization of cells at the edge of the monolayer relatively to cell-cell contact sites

A-C) Representative confocal images of colonies at 5h after surface activation co-stained against γ-Tubulin and actin together with nuclear labeling. A) Untreated colonies, B) Colonies treated with E-Cadherin BA (25 μg/ml), C) Colonies treated with N-Cadherin BA (100 μg/ml) i) γ-Tubulin staining in green, showing examples of cells polarized away from cell-cell contact sites (red arrows), towards cell-cell contact sites (blue arrows) and non-polarized cells (orange arrows). A cell is considered polarized when the microtubule-organizing center (MTOC, shown here as a distinguished green dot) is located rear/frontal to the nucleus in relation to the direction of movement [49]. The direction of movement is towards the higher microtubule distribution edge in each cell [50]. ii) Merge showing the nucleus (blue), γ-Tubulin (green) and actin (red) co-staining of the colonies shown in (i). Scale bars: 50 μm. D) Quantification of cell polarization in untreated (control) and E- or N- Cadherin BA treated colonies. For all conditions, the number of cells polarized towards cell-cell contacts is not significantly different from the number of cells polarized away from cell-cell contacts. Control: mean diff $_{away\text{-}towards}$=13 ± 6.5; p=0.07. E-Cadherin BA: mean diff $_{away\text{-}towards}$=-5.3± 4.3; p=0.26. N-Cadherin BA: mean diff $_{away\text{-}towards}$= -2.9 ± 8.6; p=0.74. Moreover, 1-way ANOVA showed no significant differences in the ratio of [perc. cells polarized away / perc. cells polarized towards] between treatment groups (F: 2.4; p=0.14).

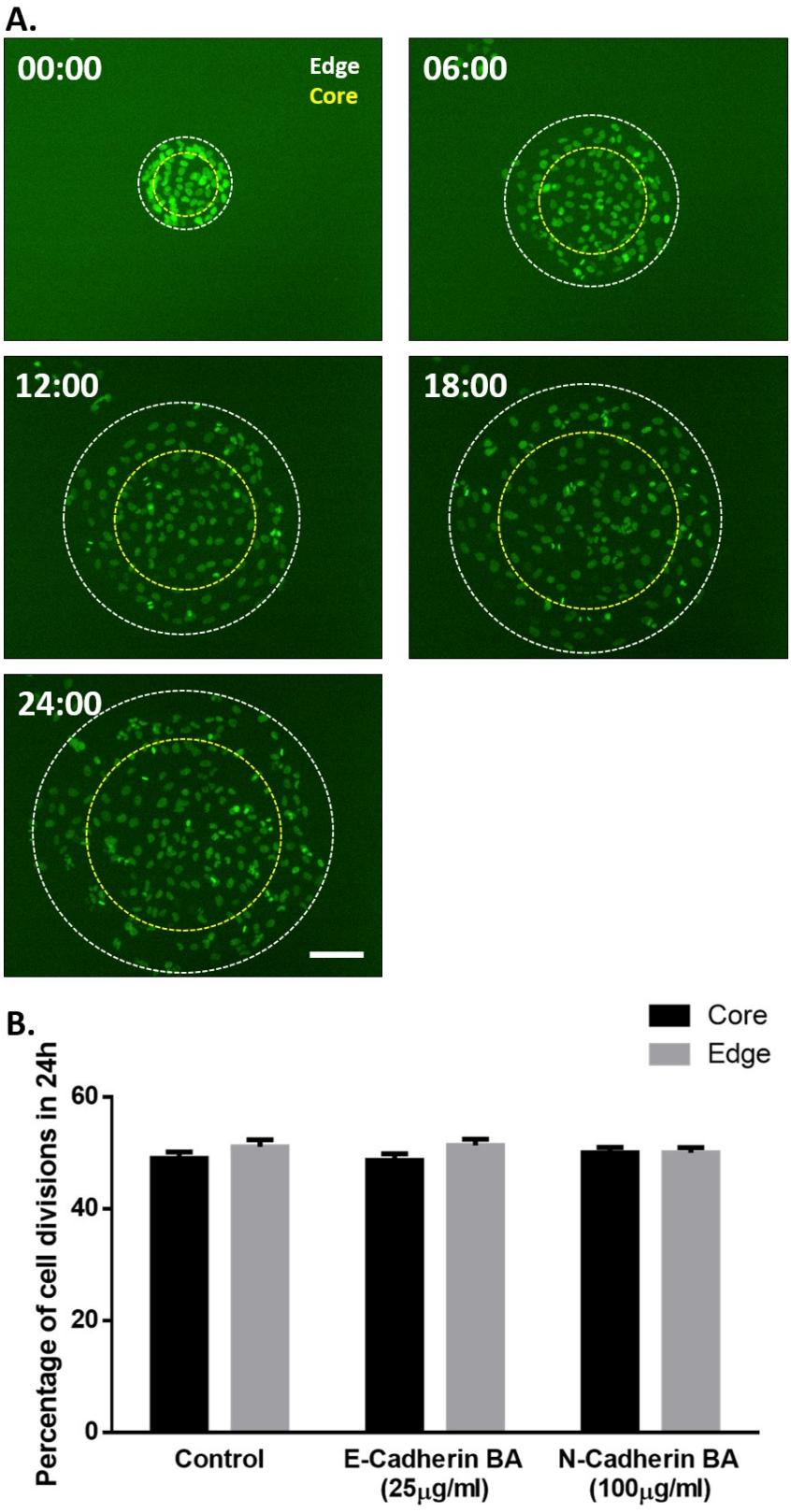

Supplementary Figure 8: Distribution of cell divisions in the different regions of the cluster

A) Representative time lapse showing cell spreading in the first 24h after surface activation. At each timepoint, the clusters are divided in two regions: The Edge of the cluster (white-dashed outer ring) and the Core of the cluster (yellow-dashed inner circular area). Scale bar: 100 μm. B) Evaluation of cell division in the different regions of the cluster at 24h after surface activation. In each area, the number of cell divisions counted was divided by the total number of cells in that area and expressed as a percentage of the total cell divisions. We find no significant difference between the percentage of cell divisions in the core vs edge area of the cluster in the control condition (mean diff.=-2.1 ±1.7; p=0.27), as well as in the E-Cadherin BA condition (mean diff.=-2.7 ±1.7; p= 0.18) and N-Cadherin BA condition (mean diff.=-0.02 ±1.4; p=0.99). Therefore, cell divisions seem to be evenly distributed in the cluster.

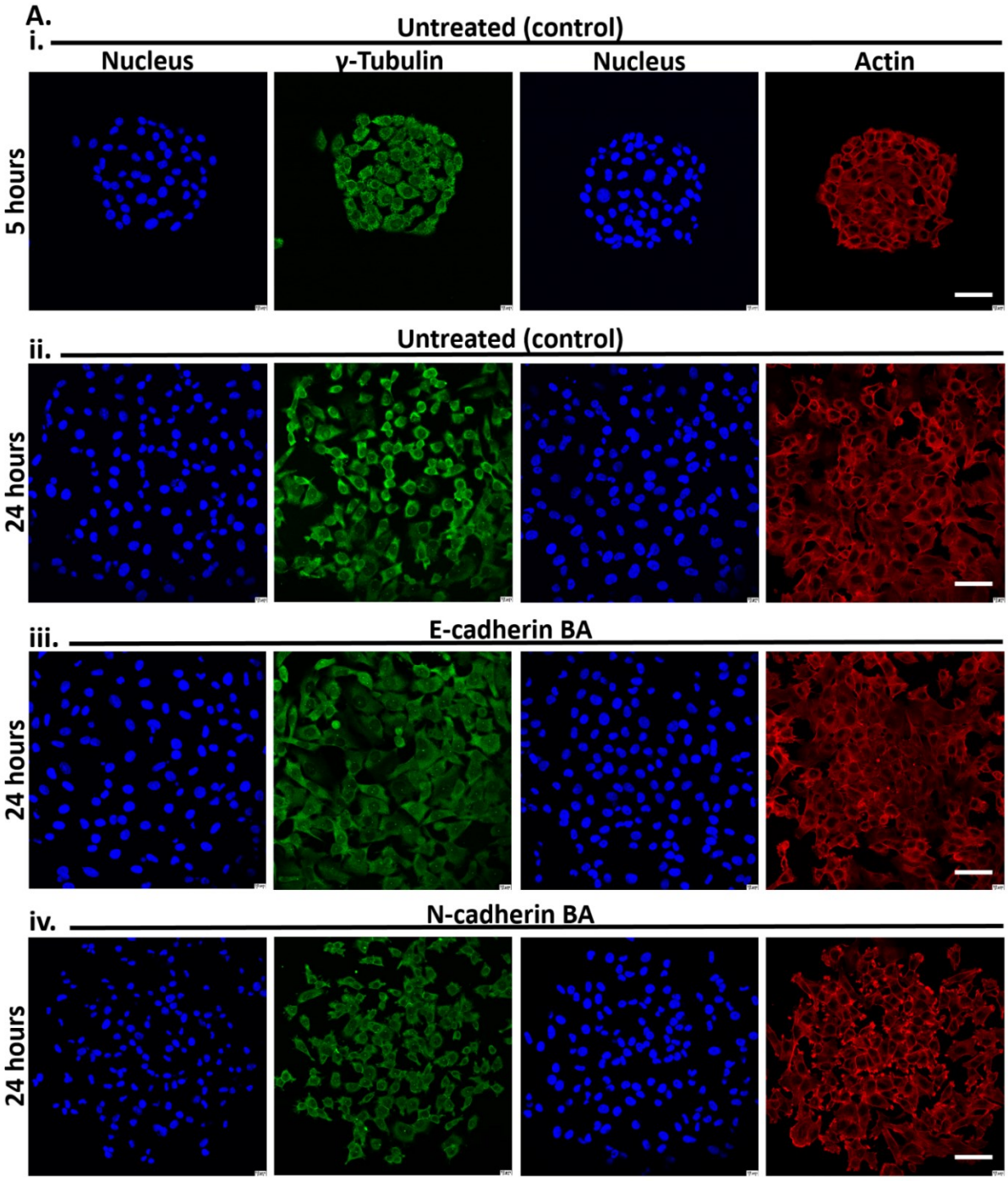

Supplementary Figure 9: Cytoskeletal staining of control and E- or N-Cadherin BA treated colonies

Representative confocal microscopy images of colonies with cytoskeletal (γ-Tubulin-green, actin-red) and nuclear-blue staining. i, ii) Untreated (control) colonies 5 and 24 hours after the start of migration. iii) Colonies treated with E-Cadherin blocking antibody, 24 h after treatment. iv) Colonies treated with N-Cadherin blocking antibody, 24 h after treatment. In general, cell clusters are not confluent and a high number of gaps between the cells can be observed. Scale bar: 50 μm.

2.6 References

1. Friedl, P. and D. Gilmour, *Collective cell migration in morphogenesis, regeneration and cancer.* Nature Reviews Molecular Cell Biology, 2009. **10**(7): p. 445-457.
2. Rey-Barroso, J., et al., *Switching between individual and collective motility in B lymphocytes is controlled by cell-matrix adhesion and inter-cellular interactions.* Scientific Reports, 2018. **8**(1): p. 5800.
3. Grada, A., et al., *Research Techniques Made Simple: Analysis of Collective Cell Migration Using the Wound Healing Assay.* Journal of Investigative Dermatology, 2017. **137**(2): p. e11-e16.
4. Wood, J.M. and M.F. Olson, *Collective migration: spatial tension relief.* Curr Biol, 2012. **22**(4): p. R125-7.
5. Trepat, X., Z. Chen, and K. Jacobson, *Cell migration.* Compr Physiol, 2012. **2**(4): p. 2369-92.
6. De Pascalis, C. and S. Etienne-Manneville, *Single and collective cell migration: the mechanics of adhesions.* Molecular biology of the cell, 2017. **28**(14): p. 1833-1846.
7. George, M., F. Bullo, and O. Campàs, *Connecting individual to collective cell migration.* Scientific Reports, 2017. **7**(1): p. 9720.
8. Ladoux, B. and R.M. Mège, *Mechanobiology of collective cell behaviours.* Nat Rev Mol Cell Biol, 2017. **18**(12): p. 743-757.
9. Etienne-Manneville, S., *Adherens junctions during cell migration.* Subcell Biochem, 2012. **60**: p. 225-49.
10. Gail, M.H. and C.W. Boone, *The locomotion of mouse fibroblasts in tissue culture.* Biophys J, 1970. **10**(10): p. 980-93.
11. Metzner, C., et al., *Superstatistical analysis and modelling of heterogeneous random walks.* Nature Communications, 2015. **6**(1): p. 7516.
12. Selmeczi, D., et al., *Cell Motility as Persistent Random Motion: Theories from Experiments.* Biophysical Journal, 2005. **89**(2): p. 912-931.
13. Brückner, D.B., et al., *Stochastic nonlinear dynamics of confined cell migration in two-state systems.* Nature Physics, 2019. **15**(6): p. 595-601.
14. Fink, A., et al., *Area and Geometry Dependence of Cell Migration in Asymmetric Two-State Micropatterns.* Biophysical Journal, 2020. **118**(3): p. 552-564.
15. Brückner, D.B., et al., *Disentangling the behavioural variability of confined cell migration.* Journal of The Royal Society Interface, 2020. **17**(163): p. 20190689.
16. Mitterwallner, B.G., et al., *Non-Markovian data-driven modeling of single-cell motility.* Physical Review E, 2020. **101**(3): p. 032408.
17. Dyson, L. and R.E. Baker, *The importance of volume exclusion in modelling cellular migration.* J Math Biol, 2015. **71**(3): p. 691-711.
18. Abercrombie, M. and J.E.M. Heaysman, *Observations on the social behaviour of cells in tissue culture: II. "Monolayering" of fibroblasts.* Experimental Cell Research, 1954. **6**(2): p. 293-306.
19. Carmona-Fontaine, C., et al., *Contact inhibition of locomotion in vivo controls neural crest directional migration.* Nature, 2008. **456**(7224): p. 957-961.
20. Camley, B.A. and W.-J. Rappel, *Physical models of collective cell motility: from cell to tissue.* Journal of physics D: Applied physics, 2017. **50**(11): p. 113002.
21. Giniūnaitė, R., et al., *Modelling collective cell migration: neural crest as a model paradigm.* Journal of Mathematical Biology, 2020. **80**(1): p. 481-504.
22. Alert, R. and X. Trepat, *Physical Models of Collective Cell Migration.* Annual Review of Condensed Matter Physics, 2020. **11**(1): p. 77-101.
23. Brückner DB, e.a., *Learning the dynamics of cell-cell interactions in confined cell migration. .* Arxiv:2008.03978, 2020.
24. Schnyder, S.K., J.J. Molina, and R. Yamamoto, *Control of cell colony growth by contact inhibition.* Scientific Reports, 2020. **10**(1): p. 6713.
25. Paulson, A., et al., *Regulation of cadherin expression in nervous system development.* Cell adhesion & migration, 2014. **8**: p. 19-28.
26. Halbleib, J.M. and W.J. Nelson, *Cadherins in development: cell adhesion, sorting, and tissue morphogenesis.* Genes Dev, 2006. **20**(23): p. 3199-214.

27. Shapiro, L. and W.I. Weis, *Structure and biochemistry of cadherins and catenins.* Cold Spring Harbor perspectives in biology, 2009. **1**(3): p. a003053-a003053.
28. Campbell, K. and J. Casanova, *A common framework for EMT and collective cell migration.* Development, 2016. **143**(23): p. 4291.
29. Loh, C.-Y., et al., *The E-Cadherin and N-Cadherin Switch in Epithelial-to-Mesenchymal Transition: Signaling, Therapeutic Implications, and Challenges.* Cells, 2019. **8**(10): p. 1118.
30. Yu, W., et al., *Cadherin Signaling in Cancer: Its Functions and Role as a Therapeutic Target.* Frontiers in Oncology, 2019. **9**(989).
31. Wheelock, M.J., et al., *Cadherin switching.* Journal of Cell Science, 2008. **121**(6): p. 727.
32. Pérez-González, C., et al., *Active wetting of epithelial tissues.* Nature Physics, 2019. **15**(1): p. 79-88.
33. Ilina, O., et al., *Cell–cell adhesion and 3D matrix confinement determine jamming transitions in breast cancer invasion.* Nature Cell Biology, 2020. **22**(9): p. 1103-1115.
34. Padmanaban, V., et al., *E-cadherin is required for metastasis in multiple models of breast cancer.* Nature, 2019. **573**(7774): p. 439-444.
35. Bindels, E.M.J., et al., *E-Cadherin Promotes Intraepithelial Expansion of Bladder Carcinoma Cells in an in Vitro Model of Carcinoma <em>in Situ</em&gt.* Cancer Research, 2000. **60**(1): p. 177.
36. Putzke, A.P., et al., *Metastatic progression of prostate cancer and e-cadherin regulation by zeb1 and SRC family kinases.* Am J Pathol, 2011. **179**(1): p. 400-10.
37. Reddy, P., et al., *Formation of E-cadherin-mediated cell-cell adhesion activates AKT and mitogen activated protein kinase via phosphatidylinositol 3 kinase and ligand-independent activation of epidermal growth factor receptor in ovarian cancer cells.* Mol Endocrinol, 2005. **19**(10): p. 2564-78.
38. Lewis-Tuffin, L.J., et al., *Misregulated E-cadherin expression associated with an aggressive brain tumor phenotype.* PloS one, 2010. **5**(10): p. e13665-e13665.
39. Su, Y., et al., *N-cadherin functions as a growth suppressor in a model of K-ras-induced PanIN.* Oncogene, 2016. **35**(25): p. 3335-41.
40. Lammens, T., et al., *N-cadherin in neuroblastoma disease: expression and clinical significance.* PLoS One, 2012. **7**(2): p. e31206.
41. Elie-Caille, C., et al., *Molecular and nanoscale evaluation of N-cadherin expression in invasive bladder cancer cells under control conditions or GW501516 exposure.* Molecular and Cellular Biochemistry, 2020. **471**.
42. Lascombe, I., et al., *N-Cadherin as a Novel Prognostic Marker of Progression in Superficial Urothelial Tumors.* Clinical Cancer Research, 2006. **12**(9): p. 2780.
43. Rebel, J.M., et al., *E-cadherin expression determines the mode of replacement of normal urothelium by human bladder carcinoma cells.* Cancer Res, 1994. **54**(20): p. 5488-92.
44. van Dongen, S.F.M., et al., *Triggering Cell Adhesion, Migration or Shape Change with a Dynamic Surface Coating.* Advanced Materials, 2013. **25**(12): p. 1687-1691.
45. d'Alessandro, J., et al., *Contact enhancement of locomotion in spreading cell colonies.* Nature Physics, 2017. **13**(10): p. 999-1005.
46. Maître, J.L. and C.P. Heisenberg, *Three functions of cadherins in cell adhesion.* Curr Biol, 2013. **23**(14): p. R626-33.
47. Fleige, S., et al., *Comparison of relative mRNA quantification models and the impact of RNA integrity in quantitative real-time RT-PCR.* Biotechnol Lett, 2006. **28**(19): p. 1601-13.
48. Chopra, A., W.G. Willmore, and K.K. Biggar, *Protein quantification and visualization via ultraviolet-dependent labeling with 2,2,2-trichloroethanol.* Scientific Reports, 2019. **9**(1): p. 13923.
49. Silverman-Gavrila, R., et al., *Rear polarization of the microtubule-organizing center in neointimal smooth muscle cells depends on PKCα, ARPC5, and RHAMM.* The American journal of pathology, 2011. **178**(2): p. 895-910.
50. Kaverina, I. and A. Straube, *Regulation of cell migration by dynamic microtubules.* Semin Cell Dev Biol, 2011. **22**(9): p. 968-74.
51. Attanasi, A., et al., *Collective Behaviour without Collective Order in Wild Swarms of Midges.* PLOS Computational Biology, 2014. **10**(7): p. e1003697.
52. Basan, M., et al., *Alignment of cellular motility forces with tissue flow as a mechanism for efficient wound healing.* Proceedings of the National Academy of Sciences, 2013. **110**(7): p. 2452.
53. Garcia, S., et al., *Physics of active jamming during collective cellular motion in a monolayer.* Proceedings of the National Academy of Sciences, 2015. **112**(50): p. 15314.

54. Sepúlveda, N., et al., *Collective Cell Motion in an Epithelial Sheet Can Be Quantitatively Described by a Stochastic Interacting Particle Model.* PLOS Computational Biology, 2013. **9**(3): p. e1002944.
55. Brückner, D.B., et al., *Learning the dynamics of cell–cell interactions in confined cell migration.* Proceedings of the National Academy of Sciences, 2021. **118**(7): p. e2016602118.
56. Manova, R., T.A. van Beek, and H. Zuilhof, *Surface functionalization by strain-promoted alkyne-azide click reactions.* Angew Chem Int Ed Engl, 2011. **50**(24): p. 5428-30.
57. Bubeník, J., et al., *Established cell line of urinary bladder carcinoma (T24) containing tumour-specific antigen.* International Journal of Cancer, 1973. **11**(3): p. 765-773.
58. Lang, K., et al., *Signal processing in migrating T24 human bladder carcinoma cells: role of the autocrine interleukin-8 loop.* Int J Cancer, 2002. **99**(5): p. 673-80.
59. Jin, H., et al., *Divergent behaviors and underlying mechanisms of cell migration and invasion in non-metastatic T24 and its metastatic derivative T24T bladder cancer cell lines.* Oncotarget, 2015. **6**(1): p. 522-536.
60. Luo, K.-W., et al., *EGCG inhibited bladder cancer T24 and 5637 cell proliferation and migration via PI3K/AKT pathway.* Oncotarget, 2018. **9**(15): p. 12261-12272.
61. McBeth, L., et al., *Glucocorticoid receptor beta increases migration of human bladder cancer cells.* Oncotarget, 2016. **7**(19): p. 27313-24.
62. Hakim, V. and P. Silberzan, *Collective cell migration: a physics perspective.* Rep Prog Phys, 2017. **80**(7): p. 076601.
63. Petitjean, L., et al., *Velocity fields in a collectively migrating epithelium.* Biophys J, 2010. **98**(9): p. 1790-800.
64. Yamaguchi, N., et al., *Leader cells regulate collective cell migration via Rac activation in the downstream signaling of integrin β1 and PI3K.* Scientific reports, 2015. **5**: p. 7656-7656.
65. Petrie, R.J. and K.M. Yamada, *At the leading edge of three-dimensional cell migration.* Journal of cell science, 2012. **125**(Pt 24): p. 5917-5926.
66. Theveneau, E. and C. Linker, *Leaders in collective migration: are front cells really endowed with a particular set of skills?* F1000Research, 2017. **6**: p. 1899-1899.
67. Brugués, A., et al., *Forces driving epithelial wound healing.* Nat Phys, 2014. **10**(9): p. 683-690.
68. Qin, L., et al., *Roles of leader and follower cells in collective cell migration.* Molecular biology of the cell, 2021. **32**(14): p. 1267-1272.
69. Zaritsky, A., et al., *Propagating Waves of Directionality and Coordination Orchestrate Collective Cell Migration.* PLOS Computational Biology, 2014. **10**(7): p. e1003747.
70. Farhadifar, R., et al., *The Influence of Cell Mechanics, Cell-Cell Interactions, and Proliferation on Epithelial Packing.* Current Biology, 2007. **17**(24): p. 2095-2104.
71. Serra-Picamal, X., et al., *Mechanical waves during tissue expansion.* Nature Physics, 2012. **8**(8): p. 628-634.
72. Sarkar, D., G. Gompper, and J. Elgeti, *A minimal model for structure, dynamics, and tension of monolayered cell colonies.* Communications Physics, 2021. **4**(1): p. 36.
73. Tarle, V., et al., *Modeling the finger instability in an expanding cell monolayer.* Integrative Biology, 2015. **7**(10): p. 1218-1227.
74. Cates, M.E. and J. Tailleur, *When are active Brownian particles and run-and-tumble particles equivalent? Consequences for motility-induced phase separation.* EPL (Europhysics Letters), 2013. **101**: p. 20010.
75. GM., C., *Cell-Cell Interactions.*, in *The Cell: A Molecular Approach*. 2000: Sunderland (MA).
76. Nieman, M.T., et al., *N-Cadherin Promotes Motility in Human Breast Cancer Cells Regardless of Their E-Cadherin Expression.* Journal of Cell Biology, 1999. **147**(3): p. 631-644.
77. Kuphal, S. and A.K. Bosserhoff, *Influence of the cytoplasmic domain of E-cadherin on endogenous N-cadherin expression in malignant melanoma.* Oncogene, 2006. **25**(2): p. 248-259.
78. Reckamp, K.L., et al., *Tumor response to combination celecoxib and erlotinib therapy in non-small cell lung cancer is associated with a low baseline matrix metalloproteinase-9 and a decline in serum-soluble E-cadherin.* J Thorac Oncol, 2008. **3**(2): p. 117-24.
79. Oh, D.Y., et al., *Phase II trial of dacomitinib in patients with HER2-positive gastric cancer.* Gastric Cancer, 2016. **19**(4): p. 1095-1103.
80. Bodnar, L., et al., *Role of WNT/β-Catenin Pathway as Potential Prognostic and Predictive Factors in Renal Cell Cancer Patients Treated With Everolimus in the Second and Subsequent Lines.* Clin Genitourin Cancer, 2018. **16**(4): p. 257-265.

81. Kuefer, R., et al., *The role of an 80 kDa fragment of E-cadherin in the metastatic progression of prostate cancer.* Clin Cancer Res, 2003. **9**(17): p. 6447-52.
82. Schmeiser, K. and R.J. Grand, *The fate of E- and P-cadherin during the early stages of apoptosis.* Cell Death Differ, 1999. **6**(4): p. 377-86.
83. Trillsch, F., et al., *E-Cadherin fragments as potential mediators for peritoneal metastasis in advanced epithelial ovarian cancer.* Br J Cancer, 2016. **114**(2): p. 213-20.
84. Tang, M.K.S., et al., *Soluble E-cadherin promotes tumor angiogenesis and localizes to exosome surface.* Nat Commun, 2018. **9**(1): p. 2270.
85. Grabowska, M.M. and M.L. Day, *Soluble E-cadherin: more than a symptom of disease.* Front Biosci (Landmark Ed), 2012. **17**: p. 1948-64.
86. Mialhe, A., et al., *Expression of E-, P-, n-cadherins and catenins in human bladder carcinoma cell lines.* J Urol, 2000. **164**(3 Pt 1): p. 826-35.
87. Elie-Caille, C., et al., *Molecular and nanoscale evaluation of N-cadherin expression in invasive bladder cancer cells under control conditions or GW501516 exposure.* Molecular and Cellular Biochemistry, 2020. **471**(1): p. 113-127.
88. Theveneau, E. and R. Mayor, *Integrating chemotaxis and contact-inhibition during collective cell migration: Small GTPases at work.* Small GTPases, 2010. **1**(2): p. 113-117.
89. Vedula, S.R.K., et al., *Emerging modes of collective cell migration induced by geometrical constraints.* Proceedings of the National Academy of Sciences, 2012. **109**(32): p. 12974.
90. Käfer, J., et al., *Cell adhesion and cortex contractility determine cell patterning in the Drosophilaretina.* Proceedings of the National Academy of Sciences, 2007. **104**(47): p. 18549.
91. Hayashi, T. and R.W. Carthew, *Surface mechanics mediate pattern formation in the developing retina.* Nature, 2004. **431**(7009): p. 647-652.
92. Chen, W.C. and B. Obrink, *Cell-cell contacts mediated by E-cadherin (uvomorulin) restrict invasive behavior of L-cells.* J Cell Biol, 1991. **114**(2): p. 319-27.
93. Ayollo, D.V., et al., *Rearrangements of the actin cytoskeleton and E-cadherin-based adherens junctions caused by neoplasic transformation change cell-cell interactions.* PLoS One, 2009. **4**(11): p. e8027.
94. Huttenlocher, A., et al., *Integrin and cadherin synergy regulates contact inhibition of migration and motile activity.* J Cell Biol, 1998. **141**(2): p. 515-26.
95. Bracke, M.E., et al., *Functional downregulation of the E-cadherin/catenin complex leads to loss of contact inhibition of motility and of mitochondrial activity, but not of growth in confluent epithelial cell cultures.* Eur J Cell Biol, 1997. **74**(4): p. 342-9.
96. Theveneau, E., et al., *Chase-and-run between adjacent cell populations promotes directional collective migration.* Nat Cell Biol, 2013. **15**(7): p. 763-72.
97. Tanaka, M., S. Kuriyama, and N. Aiba, *Nm23-H1 regulates contact inhibition of locomotion, which is affected by ephrin-B1.* J Cell Sci, 2012. **125**(Pt 18): p. 4343-53.
98. Scarpa, E., et al., *Cadherin Switch during EMT in Neural Crest Cells Leads to Contact Inhibition of Locomotion via Repolarization of Forces.* Dev Cell, 2015. **34**(4): p. 421-34.
99. Wrighton, K.H., *Cell migration: EMT promotes contact inhibition of locomotion.* Nat Rev Mol Cell Biol, 2015. **16**(9): p. 518.
100. Milano, D.F., et al., *Regulators of Metastasis Modulate the Migratory Response to Cell Contact under Spatial Confinement.* Biophys J, 2016. **110**(8): p. 1886-1895.
101. Sommers, C.L., et al., *Cell adhesion molecule uvomorulin expression in human breast cancer cell lines: relationship to morphology and invasive capacities.* Cell growth & differentiation : the molecular biology journal of the American Association for Cancer Research, 1991. **2**(8): p. 365-372.
102. Dietrich, M., et al., *Guiding 3D cell migration in deformed synthetic hydrogel microstructures.* Soft Matter, 2018. **14**(15): p. 2816-2826.
103. Reinhart-King, C.A., M. Dembo, and D.A. Hammer, *Cell-cell mechanical communication through compliant substrates.* Biophys J, 2008. **95**(12): p. 6044-51.
104. Humphries, D.L., J.A. Grogan, and E.A. Gaffney, *Mechanical Cell–Cell Communication in Fibrous Networks: The Importance of Network Geometry.* Bulletin of Mathematical Biology, 2017. **79**(3): p. 498-524.
105. Majumdar, R., M. Sixt, and C.A. Parent, *New paradigms in the establishment and maintenance of gradients during directed cell migration.* Current opinion in cell biology, 2014. **30**: p. 33-40.
106. Camley, B.A., *Collective gradient sensing and chemotaxis: modeling and recent developments.* J Phys Condens Matter, 2018. **30**(22): p. 223001.

CHAPTER 3

Sequential and switchable patterning for studying cellular processes under spatiotemporal control*

*This chapter is based on the published article: T. Zisis[+], J. Schwarz[+], M. Balles, M. Kretschmer, M. Nemethova, R. Chait, R. Hauschild, J. Lange, C. Guet, M. Sixt, S. Zahler, 'Sequential and switchable patterning for studying cellular processes under spatiotemporal control', *ACS applied materials and interfaces*, 2021, 13, 35545-35560

[+] These authors contributed equally to the manuscript.

T. Zisis, J. Schwarz, M. Sixt and S. Zahler designed the study. T. Zisis, J. Schwarz and M. Balles wrote the paper with feedback from all authors. T. Zisis, J. Schwarz, M. Balles and M. Kretschmer performed the experiments and analysed data. M. Nemethova, R. Chait, R. Hauschild, J. Lange and C. Guet contributed to the experiments.

Special thanks to Charlott Leu for the production of our chromium wafers, Louise Ritter for her contribution of the IF stainings in Figure 4, Shokoufeh Teymouri for her help with the bioinert coated slides and finally Prof. Dr. Joachim Rädler for his valuable scientific guidance.

3.1 Introduction

Spatially controlled deposition of extracellular signaling or adhesion molecules on cell culture surfaces (also described as micropatterning) became an essential tool in all experimental fields operating with cultured cells [1-6]. “Printing” molecules on surfaces to acquire spatial control over cell microenvironments is essential for understanding processes such as cell division, differentiation, adhesion [7-9] and migration [10, 11], which are highly dynamic.

The key challenges in such surface engineering are stability, precision, and specificity. This does not only demand minimal background deposition of the applied biomolecule, but ideally also avoidance of binding of unspecific bystander molecules (like serum-factors). This is usually achieved by employing inert (passivated) background chemistry. Precision demands the option to immobilize quantitatively and ideally with sub-micron resolution. This includes digital patterns with sub-micron resolution but also the generation of continuous gradients [12] [13]. Furthermore, surface immobilization is preferably based on covalent modifications so that deposition is stable and sustainable, thereby permitting long-term applications e.g. well-free cell-culture systems.

Using structured illumination for patterning not only provides a method to covalently bind adhesive peptides or other molecules but also enables high-throughput fabrication approaches, such as creating small adhesion spots for single cell screenings over large cell culture surfaces.

Microcontact printing [14] has provided a spatiotemporally controllable setup for understanding cell mechanosensing [15-17]. However, a significant disadvantage of the conventional microcontact printing techniques is the variability in the quality of protein transfer and requirement of bulky macromolecules (i.e. Extracellular Matrix- or ECM- proteins) to create the desired patterns. This limits the applicability of such methods to settings where one or more different biomolecules are added in the process, as unwanted non-specific interactions can take place, influencing the experimental outcome. Moreover, the stability of

proteins can be significantly reduced over time, making the whole setup time sensitive. Here, we introduce a covalent, building block-based, versatile photo-immobilization technique. It comprises a light-dose dependent patterning step, which is feasible on arbitrary surfaces enabling the production of sustainable patterns and gradients. We validate the method by photo-patterning of adhesive ligands on cell repellant surface coatings, thereby confining cell growth and migration to the designated areas and gradients. In a second step, we added a further layer of complexity by enabling spatiotemporal control over two distinct light-switchable surface patterns. This gives unprecedented access to studying time dependent cellular processes *in vitro*.

3.2 Materials & Methods

3.2.1 Patterning Methods

3.2.1.1 PVA coating

Glass bottom dishes (MaTek, USA) were polyvinyl alkohol (PVA) coated as described earlier [18]. Briefly, the glass surface of MaTek dishes was activated for 25 min at room temperature with 50 % nitric acid (Sigma Aldrich, St. Louis, Missouri). After activation, the dish was rinsed overnight in ddH_2O. Subsequently, the glass surface was deprotonated by incubation for 15 min at room temperature with 200 mM NaOH (Sigma Aldrich, St. Louis, Missouri). The deprotonated and washed glass surface (ddH_2O) was blow-dried using canned nitrogen. By incubation with 1 % aqueous solution of APTES (w/v, Sigma Aldrich, St. Louis, Missouri), the glass surface was amino-silanized for 5 min and carefully washed with ddH_2O for 10 min. The amino-silanized glass surface was then cured at 65 °C for 3 h. For aldehyde activation, surfaces were incubated with 0.5 % aqueous glutaraldehyde (Sigma Aldrich, St. Louis, Missouri) solution for 30 min at room temperature. A ~ 200 nm thick poly-vinyl alcohol (PVA,

6 % aqueous solution with 0.1 % 2N HCl) film was bound to the glutaraldehyde activated surface by spin coating (40 s at 7000 rpm; 550 rpm acceleration within 18 s). Prior to use, dishes were washed carefully with ddH_2O.

3.2.1.2 Photo-immobilization of 6-FAM-alkyne with Pulsed UV Laser

Approximately 20 µL 6-FAM-alkyne (Lumiprobe, Hannover, Germany) were placed in the middle of a PVA coated glass dish and patterns were written using a steerable, pulsed UV laser (λ = 355 nm) as described before [8]. Briefly, the UV laser was focused into the interface between the bottom of the PDMS coated glass slide and the 6-FAM-alkyne solution with a long working distance 20x objective (Zeiss LD Plan Neo 20x 0.4). A pair of high-speed galvanometric mirrors, controlled by a custom program, was moving the focal spot within the 6-FAM-alkyne droplet.

The gradient pattern was specified by an image whose pixel values determined the light dose used for bleaching. Careful calibration allowed compensating for the off-center drop-off of numerical aperture of the objective as well as the geometric distortions from the imperfect imaging of the scan mirrors into the back aperture of the objective. This allowed gradient writing in the full field of view of the objective. For each spot, the total light dose was split up into multiple laser pulses in order to average out the pulse-to-pulse power variability of the laser. The gradient was written one spot at a time with the scanning mirrors moving the laser focus by about half the diameter of the focus spot in order to create a continuous pattern. In this fashion, crosstalk between different locations in the pattern was minimized since the scattered light from one spot did not reach the threshold of bleaching elsewhere unlike projector based systems where the entire area is exposed simultaneously. The low wavelength of the UV laser lead to a high lateral resolution (~0.7 µm) and the low crosstalk to a high dynamic range (~100:1) of the gradient pattern. The writing speed was limited by the laser's pulse frequency of 1 kHz. A full description of the hardware employed can be found in Behrndt *et al.* [19].

3.2.1.3 Photo-immobilization of 6-FAM-alkyne with projector-based photopatterning

Projector-based photo patterning was accomplished using a microscope-coupled LCD projector similar to one designed by Stirman, *et al*. [20]. Briefly, the light source of an LCD-based overhead projector (Panasonic PT AE6000E; contrast ratio 297±1:1) is replaced by a 470 nm LED source (Thorlabs M470L3). The projection lens is removed and the projected image coupled by a relay lens (Thorlabs AC508-100-A-ML, f = 100 mm) into the rear port of an Olympus IX83 inverted microscope. A 50/50 beamsplitter (Thorlabs BSW10R) directs half of the incident light through a 20x objective (Olympus LUCPLFLN20XPh) to the substrate surface. The reflection of the projected pattern from the substrate-air interface is imaged on a digital camera (Hamamatsu Orca Flash4.0v2). With the microscope focused on the substrate surface, the projector is adjusted to bring the projected image and microscope focal planes into alignment. Custom software utilizing MATLAB and MicroManager [21] is used to generate and project patterns, and to control LED illumination and the microscope. When exposing patterns, a prepared substrate is washed and dried by aspiration before mounting securely on the microscope's stage. The microscope focus is then adjusted to bring a projected target pattern into focus at the substrate surface. When multiple patterns are to be exposed on a single substrate, focal offsets are manually determined at the extremities of the pattern array and offsets at intermediate locations estimated by least squares fitting of a plane through the measured points. The LED is extinguished and a small volume of 6-FAM-alkyne is carefully deposited onto the target surface without displacing the substrate. The system then automatically cycles sequentially through the pattern locations, at each exposing specified patterns for corresponding durations.

3.2.1.4 1,3 dipolar cycloaddition of RGD-HF555 in single photopatterning

Volume	Component	Concentration in reaction
2.2 µL	Click-it cell reaction buffer (Thermo)	-

19.8 µL	ddH_2O	-
2.5 µL	Reaction buffer additive (Thermo)	-
0.5 µL	$CuSO_4$	8.3 mM
5 µL	RGD-HF555 (stock 180 µM)	30 µM

Table 5: Click reaction mixture

GRGDS-HF555-Azide (RGD-HF555) was custom synthesized by Eurogentec (Serain, Belgium). Following laser writing or projector based patterning, the alkyne patterned PVA surfaces were washed with PBS and incubated for 30 min in the dark with the reaction mixture (Table 5). After washing with PBS, RGD-HF555 patterns can be stored for up to a month under PBS.

3.2.1.5 High-throughput Photopatterning with collimated LED

ibidi µ-Slides VI $^{0.4}$ Bioinert were used as cell repellent background for high-throughput patterning with a collimated LED. In each channel 24 µl of the linker solution (either 0.9 mM 6-FAM-Alkyne (Jena Bioscience, Germany) in PBS or 1.5 mM Diazirine-Alkyne (custom synthesis from Enamine, Ukraine) in MilliQ water) are injected. The slide is put on a chromium mask (Compugraphics, Germany) which contains the desired structures to shield the designated non-adherent areas from light exposure. The mask with the slide is put on an upwards facing collimated LED of fitting wavelength (for 6-FAM-Alkyne: 470 nm LED (Thorlabs, Germany); for Diazirine-Alkyne: 380 nm (Rapp OptoElectronic, Germany) and illuminated for 5 min at maximum intensity (6-FAM-Alkyne) or for 1 min at 40% intensity (Diazirine-Alkyne). After illumination channels are washed 6 times with Milli-Q water to get rid of unbound linker.

3.2.1.6 1,3 dipolar cycloaddition of cRGD or sulfo-Cy3 in high-throughput photopatterning

After immobilization of the linker as described in the previous chapter, the linker is either functionalized with a sulfo-Cy3-Azide (Lumiprobe, Germany) for pattern visualization, or with cyclic-RGD-Azide (cRGDfK, Peptides International, US) for cell adhesion studies. For both reactions the same conditions are used (Table 6). First, $CuSO_4$ (Jena Bioscience, Germany) is mixed with BTTAA (Jena Bioscience, Germany). Then the buffer, the Azide and Ascorbic Acid (Jena Bioscience, Germany) is added and mixed thoroughly. 25 µl of the reaction mixture is directly after mixing pipetted into each channel and incubated for 1 hour in the dark. The channels are afterwards washed multiple times with MilliQ water and after another washing step overnight the channels are emptied and dried by an air stream.

Volume	Component (stock concentration)	Assay concentration
15 µL	sulfo-Cy3-Azide or cRGD-Azide (2 mM)	200 µM
30 µL	BTTAA (50 mM)	10 mM
15 µL	Ascorbic Acid (1 M)	100 mM
3 µL	$CuSO_4$ (100 mM)	2 mM
87 µL	100 mM sodium phosphate buffer (pH 8.0)	

Table 6: Click reaction mixture for a µ-Slide $IV^{0.4}$, volume (25 µl/channel) used in the high-throughput photopatterning protocol

3.2.1.7 Fabrication of aluminum re-aligner

A custom-made aluminum re-aligner was designed by a drawing software, e.g., autocad (Autodesk) or circuitpro pl (LPKF Laser & Electronics, Germany) to the size and dimension necessary to accommodate the collimated LEDs and Bioinert foils used. The fabrication was done in the Chemistry and Pharmacy Precision Mechanics Workshop using a single slab of aluminum and the appropriate precision machines. The exact dimensions as well as a detailed visual representation is provided in Fig. S5.

3.2.1.8 Fabrication of chromium masks masters

The desired patterns can be designed by a drawing software, e.g., autocad (Autodesk) or circuitpro pl (LPKF Laser & Electronics, Germany). Masters for stamp preparation or masters for photopatterning experiments can then be created by following established protocols (such as those provided by photoresist producers like MicroChem) or the protocol provided in the supplementary methods. Note that labs that do not have the means to create stamp masters can order them online (from HTS Resources, for example). Once prepared, each master can be used to make multiple stamps or multiple surface photopatterning experiments.

3.2.1.9 Sequential Photopatterning

For the photopatterning of tip areas we used the first chromium mask produced as described above, etched in a line patterned-fashion, with cross-shaped alignment markers on either side of the main patterns. The mask was placed on the custom-made re-aligner and a 50 µl of 2 mM 6-FAM-Azide dye-linker (Lumiprobe Corporation, US) solution in PBS was added at the center of the mask and then carefully covered by the ibidi's Bioinert foil so that the liquid spreads homogeneously on the surface. Upon 7 min max illumination, from underneath, with a 470nm collimated LED (Thorlabs, Germany), the line pattern was produced on the foil's inner surface and the foil was removed from the re-aligner, as was the first chromium mask. The foil was then submerged for 5 min in a petri dish with PBS (pH 8.5) and the mask was submerged for 5 min in a separate petri dish with the same buffer. Then, the foil was submerged for 5 min in a new PBS (pH 8.5) solution and the mask for 5 min in a new Ethanol (99%, Sigma-Aldrich, US) solution. Finally, the foil was submerged one last time for 5 min in a MilliQ solution and then together with the mask dried in a nitrogen stream and left at room temperature for 30 min. For the photopatterning of the stalk areas, we used a second chromium mask etched in a square patterned-fashion, with square-shaped alignment markers on either side of the main patterns. The second mask was placed on the re-aligner and a 50 µl of 10 mM Diazirine-Alkyne dye-linker in PBS (Sigma-Aldrich, US) solution was added at the

center. As the tip-patterned foil was positioned on top, the cross over square alignment markers were used to precisely align the foil's existing line pattern with the square pattern of the second mask. In all cases, the precise alignment was performed under the microscope at 10X magnification (Evos fl Cell Imaging System, Life technologies, US). This second mask-dye-foil configuration was illuminated, from underneath, for 5 min with a 360nm collimated LED (RappOptoElectronic GmbH, Germany) resulting in the final line (tip) and square (stalk) photo-patterned surface on the Bioinert foil. Next, the foil and the second mask were washed again following the previously described multistep washing protocol. As a next step, an adhesive 8-well bottomless μ-Slide (sticky-Slide 8 Well, ibidi GmbH, Germany) was attached on the patterned surface of the foil. We continued with the addition of click reaction solutions starting with 15 μl of the click reaction solution (Table 7) containing Azide-RGD peptides were added at the center of each well, with an 8 x 8 mm glass coverslip (H. Saur Laborbedarf, Reutlingen, Germany) above them and allowed to react for 2 hours. During this time the azide groups on the RGDs formed triazole links with the Alkyne groups of the Diazirine-Alkyne conjugates that were already attached to the square areas. As a result, these areas were now activated with RGD and therefore adhesive to cells. At this point, HMEC cells were trypsinized after reaching confluency, diluted to the desired density (170.000 cell/ml) in endothelial cell growth medium and 250 μl of this cell suspension were added in each well and allowed to settle overnight at 37^{o}C, forming the initial stalk cell population on the square areas. Following that, cells were gently washed 1x with the medium and 200 μl of new medium were added in each well. Then, for the second click reaction solution, 5 μl of 100μM BCN-cRGDfk (Synaffix, Netherlands) in PBS were added in the medium of each well to a final concentration of 10 μM. The BCN groups formed a link with the Azide groups of the 6-FAM-Azide conjugates that were already attached to the line areas and as a result, these areas were now also activated with RGD and thus adhesive to cells (timepoint 0).

Volume	Component (stock concentration)	Assay concentration
36 µL	cRGD-Azide (2 mM) or DBCO-Sulfo-Cy5 dye (1 mM)	600 µM cRGD-Azide or 70 µM DBCO-Sulfo-Cy5 dye
20 µL	BTTAA (50 mM)	10 mM
14 µL	Ascorbic Acid (1 M)	100 mM
6 µL	$CuSO_4$ (100 mM)	2 mM
44 µL	100 mM sodium phosphate buffer (pH 8.0)	

Table 7: Click reaction mixture for an 8-well slide volume (15 µl/well) used in the sequential photopatterning protocol

3.2.2 Cell culture and primary cells

Swiss 3T3 mouse fibroblasts were maintained in high-glucose Dulbecco's modified eagle medium (DMEM+GlutaMAX) supplemented with 1% penicillin, 1% streptomycin, 1% glutamine and 10% fetal bovine serum (Gibco Life Technologies) at 37 °C.

Zebrafish used in this study were bred and maintained according to the Austrian law for animal experiments ("Österreichisches Tierschutzgesetz"). For preparation of keratocytes, scales from wild type zebrafish (strain AB) were transferred to plastic cell culture dishes containing start medium as described previously (Anderson, K. S. & Small, J. V. Preparation and fixation of fish keratocytes. Cell Biology: A laboratory Handbook, Vol. 2, 372–376 (Academic, 1998). After 1-day incubation at 28 °C monolayers of cells were treated with 1 mM EDTA in running buffer for 45-60 min to release individual cells.

NIH-3T3 mouse fibroblasts were maintained in DMEM (Gibco Life Technologies) supplemented with 4 mM L-Glutamine (Gibco Life Technologies) and 10% bovine calve serum (Gibco Life Technologies) at 37°C and 5% CO_2.

RCC26 renal cell carcinoma cells are maintained in RPMI (Gibco Life Technologies) supplemented with 10% FCS (Gibco Life Technologies), 1% MEM (Non-essential Amino Acid

solution, Sigma-Aldrich) and 1% sodium pyruvate (Gibco Life Technologies) at 37°C and 5% CO_2.

Human Microvascular Endothelial Cells (HMECs) were purchased from ATCC and maintained in endothelial cell growth medium containing 10% fetal calf serum (FCS), 10.000 U/ml penicillin/streptomycin and 250 mg/ml amphotericin B under constant humidity at 37°C and 5% CO_2. Experiments were performed using cells at passage 6.

3.2.3 Adhesion assays and migration assays

3.2.3.1 3T3 Fibroblasts

Confluent 3T3 fibroblasts were detached with 0.05 % trypsin-EDTA. Depending on the experiment, 10^4-10^5 cells were plated onto GRGDS functionalized coverslip and incubated 3-4h at 37 °C to allow for attachment. Prior to recording on the microscope, unattached cells were removed by gentle washing with medium.

3.2.3.2 Zebrafish keratocytes

EDTA released zebrafish keratocytes were washed with PBS, detached with 0.05 % trypsin-EDTA and replated on GRGDS functionalized coverslips. After 30 min incubation at RT nonattached cells were washed away.

3.2.3.3 RCC cells and NIH-3T3

Subconfluent cells were detached using trypsin/EDTA solution. Depending on the experiment 2.5-4x10^5 cells/ml in culture medium were flushed into the channels of a µ-Slide VI $^{0.4}$. Excess solution was removed, leaving only the channels filled. The reservoirs were directly filled with culture medium and the slide was incubated overnight at 37°C. The next day, the cell culture medium was carefully exchanged to wash away unattached cells. For long-term cultivation

cells were incubated at 37°C and cell culture medium was exchanged every 2-3 days.

3.2.4 Immunohistochemistry

3.2.4.1 Antibody and staining reagents for high-throughput patterning experiments

Antibodies used to stain RCC26 cells were mouse anti-alpha-tubulin antibody (diluted 1:1000, Sigma-Aldrich) in combination with anti-mouse IgG-Atto594 (end concentration 2 µg/ml, Sigma-Aldrich). To stain for actin and the nucleus DY-490-Phalloidin (1:500, Dyomics) and DAPI (1µg/ml, Sigma-Aldrich) were used, respectively.

Cells were fixed by exchanging the cell culture medium with 10% neutral buffered formalin solution (Sigma-Aldrich, Germany) and incubate for 10 min at room temperature. Channels were washed 6x with PBS and subsequently incubated with 0.5% Triton X-100 in PBS (Sigma-Aldrich) for 15 min at room temperature. After washing with PBS 30 µl of primary antibody solution was pipetted in each channel and incubated overnight at 4°C. After washing 6x with PBS for 5 min a mixture of secondary anti-mouse antibody, phalloidin and DAPI in PBS was injected in the channels and incubated for 3 h at room temperature in the dark. After a final washing step with 6x PBS for 5 min cells were ready for imaging.

Fluorescence imaging of stained cells was performed on a Nikon Eclipse Ti, fluorescence microscope (Nikon, Germany) equipped with a Plan Apo 60X/1.4 oil objective (Nikon, Germany) and an Orca Flash 4.0 LT camera (Hamamatsu Photonics, Japan)

3.2.4.2 Antibodies and staining reagents for tip/stalk experiment

The primary antibodies used in this study were raised against, ADAMTS1 (3C8F4) mouse mAb IgG_{1k}, sc-47727 (Santa Cruz Biotechnology, Dallas, TX); Dll4 (G-12) mouse mAb IgG_{2a}, sc-365429 (Santa Cruz Biotechnology, Dallas, TX); HEY1 rabbit pAb, ab22614 (Abcam, Cambridge, UK); Jagged1 rabbit pAb, ab7771 (Abcam, Cambridge, UK).

The following secondary antibodies were used for this study, Alexa Fluor 488-conjugated goat anti-mouse IgG (H+L), A-11001; Alexa Fluor 647-conjugated chicken anti-rabbit IgG (H+L), A-21443. Hoechst 33342 (Sigma-Aldrich, St. Louis, MO) was applied in a dilution of 1:100 with an end concentration of 5 µg/ml. The FluorSave Reagent mounting medium was purchased from Merck Millipore (Darmstadt, Germany).

3.2.4.3 Immunofluorescence staining of tip/stalk experiment

The immunofluorescence staining was performed 16 h after activation of the pattern. For immunofluorescence staining, cells were briefly washed with PBS with Ca^{2+} and Mg^{2+}. Subsequently, cells were fixed with 4% methanol-free formaldehyde solution (Themo Fisher, Waltham, MA) for 10 min, washed with PBS, permeabilized with 0.2% Triton X-100 (Roth, Karlsruhe, Germany) in PBS for 10 min and again washed with PBS. Unspecific binding sites were blocked with 1% BSA (Sigma-Aldrich, St. Louis, MO) in PBS for 30 min at room temperature. For double staining, cells were incubated with the primary antibodies diluted in 0.2% BSA in PBS (1:200) over night at 4°C. After 3x10 min washing with 0.2% BSA in PBS, cells were incubated with the secondary antibodies (1:400) plus Hoechst 33342 (1:100) diluted in PBS for 1 h at room temperature. After 2x10 min washing with 0.2% BSA in PBS and 1x10 min washing with PBS, samples were sealed with one drop of mounting medium.

3.2.5 Microscopy

3.2.5.1 Single photopatterning experiments

Adhesion and migration assays were recorded on a Leica DMIL LED with 10x/0.22 High Plan I objective. For RGD-HF555 imaging and quantification, images were obtained using 20x/0.8 air and 63x/1.4 oil immersion objectives on a Zeiss Axio Observer microscope equipped with an external light source (Leica).

3.2.5.2 High-throughput photopatterning with collimated LED

To compare the immobilization of Diazirne-Alkyne and 6-FAM-Alkyne, patterns were functionalized with sulfo-Cy3-Azide and imaged on a Nikon Eclipse Ti fluorescence microscope (Nikon, Germany) equipped with a 10x/0.3 objective (Nikon, Germany) and an Orca Flash 4.0 LT camera (Hamamatsu Photonics, Japan).

To evaluate the autofluorescence of the pattern generated with the two different linkers, patterns that were functionalized with cRGD-Azide were imaged on the Nikon Eclipse Ti fluorescence microscope equipped with a 10x/0.3 objective with identical illumination settings.

Images of cells were taken on the Nikon Eclipse Ti fluorescence microscope equipped with a 4x/0.13 or 10x/0.3 objective.

3.2.5.3 Sequential photopatterning experiments

Live cell imaging was performed using the HMEC seeded 8-well photopatterned Bioinert slides with an Eclipse Ti inverted microscope (Nikon, Dusseldorf, Germany) with a 4x/10x phase contrast objective and a CCD camera ([DS-Qi1Mc] Nikon, Dusseldorf, Germany). The slides were inserted into a 37 °C heating and incubation system that was flushed with actively mixed 5% CO_2 at a rate of 10 l/h, and the humidity was kept at 80% to prevent dehydration. The cells were imaged in bright-field and the line patterns were detected at a 488 nm wavelength using the integrated fluorescence LED. Time-lapse video microscopy was performed with a time interval of 5 min between images over 24 h.

3.2.5.4 Imaging of immunofluorescence staining in the tip/stalk experiments

Imaging was performed using the Leica TCS SP8 confocal microscope with the LAS X Core software. A HC PL APO CS2 40x/1.30 NA oil objective as well as hybrid detectors (Leica HyD) and photomultipliers (PMT) were applied. In sequential scanning mode pinhole size was positioned to 1.0 airy units and the pixel size was set to 2048x2048. Two frames were obtained

for every channel with a frame rate of 0.582 per second. Following lasers and excitation sources were employed: 405 nm (diode), 488 nm (argon) and 647 nm (argon).

3.2.5.5 Evaluation of dye-linker immobilization efficiency

To visualize both patterns and evaluate the immobilization efficiency of the sequential photopatterning we used, for the line patterns, the residual intensity of the 6-FAM-Azide dye and for the squares, a DBCO-Sulfo-Cy5 dye (Jena Bioscience, Germany) to label the azides on the Diazerin-azide-bleached dye via click chemistry (Table 7). Images were taken using a Leica TCS SP8 confocal microscope with HC PL Fluotar CS2 10x/0.3 NA DRY (Leica, Wetzlar, Germany) using LAS X Core Software. The argon laser with a wavelength of 488 nm or 647 was used and the wavelength range of the detector was set between 480-530 nm or 640-680 respectively. All images were analyzed using ImageJ version 1.53c [22] software tool.

3.2.6 Cell tracking and image quantification

3.2.6.1 Single photopatterning experiments

For image processing and cell tracking, Fiji [23] and a plugin for manual tracking ("Manual Tracking", [24]) were used. Images and tracking data were analyzed using Matlab 2013 (MathWorks Inc., US). Brightfield movies were preprocessed by normalizing the brightness of each frame. Then the time averaged median was subtracted to remove non-motile particles such as dirt, dead cells etc. from the images. Subsequently a pixel classifier (Ilastik [25]) was manually trained on one data set to distinguish cell from non-cell pixels. The time projection of cell pixels was used to visualize the printed area and the RGD-HF555 gradient was manually added to the movies as an extra channel. All cells were manually tracked using ImageJ version 1.53c [23] and its plugin for manual tracking (TrackMate). The position of the cells' center was used to determine the concentration by means of the extra channel. The

probability density was defined as the number of localizations obtained through the tracking at a specific concentration divided by the total number of localizations.

Quantification of immobilization efficiency of RGD-HF555

Fluorescence intensities of a dilution series of RGD-HF555 (0.8 ng/mL, 0.16 ng/mL and 0.08 ng/mL) were measured in a defined volume of a 12.87 µm high PDMS chamber ($4.2x10^{-8}$ mL; 57.1 µm x 57.1 x 12.87 µm) (see Supplementary Methods part for chamber production) and a standard curve was calculated (Fluorescence intensity = 3.309±0.1144 molecules/μm^2). Fluorescence intensities of patches of surface immobilized RGD-HF555-Azide were measured using the same imaging settings as for the dilution series. Immobilized RGD-HF555 concentrations were calculated from measured fluorescence intensities using the obtained standard curve.

Comparison of Diazirine-Alkyne and 6-FAM-Alkyne immobilization with high-throughput patterning using a collimated LED

To evaluate the signal-to-noise-ratio (S/N ratio) between the patterned area and the non-illuminated background, images were analyzed using ImageJ version 1.52i [22] software tool. A line profile in ImageJ across a pattern was normalized to the maximum intensity detected to compare patterns generated with the two different linkers.

3.2.6.2 Quantification of immunofluorescence staining in tip/stalk experiments

Images of immunofluorescence stained patterns were processed and analyzed using ImageJ version 1.53c software tool. After images were segmented (Trainable Weka Segmentation tool), the intensities were determined.

3.2.7 Statistical analysis

Statistical analysis was performed using GraphPad Prism 8. The type of analysis as well as significant differences are indicated in the corresponding Figures except for a detailed SmartFlares statistical analysis which is presented in Table S1, S2.

3.3 Results & Discussion

3.3.1 Overview of the building block based photopatterning technique and its components

Building block based patterning can be used for 2D surface modification in various applications, from generation of adhesion cue gradients, to single cell adhesion grids and spatiotemporally-controlled cell adhesion patterns (Fig. 1A i-iii). This photopatterning technique combines two orthogonal reaction steps in order to surface immobilize molecules in a bioactive monolayer. In a first step, a linker molecule labeled with a photoreactive tag and an adapter group is covalently immobilized on any surface by structured illumination (Fig. 1B i) [26, 27]. In a second step, the relevant ligand for the desired biological set-up is covalently attached to the surface bound linker via an adaptor system (Fig. 1B ii)). Separation of the photoimmobilization and the ligand binding step hereby prevents degradation of the ligand during illumination. Thus, only active and accessible ligands are presented on the surface. An established patterning process can easily be adapted to another biological system, making the building block based photo-patterning method very versatile. We test several photoreactive molecules, adapter systems, cell-adhesive ligands, surface passivation agents and illumination methods for building block based photopatterning. Different combinations of the aforementioned components are implemented for different biological applications and their compatibility and efficacy is discussed.

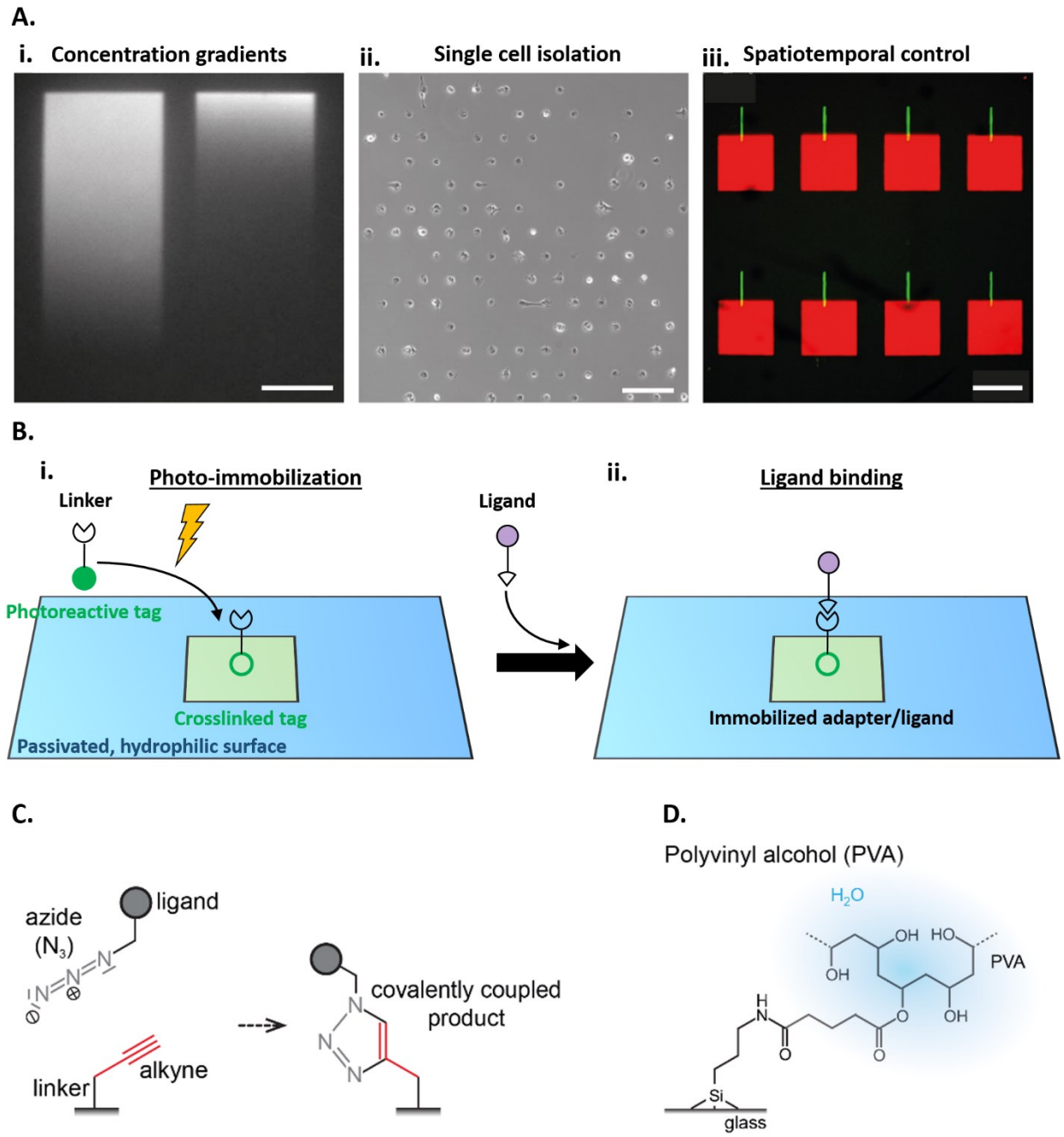

Figure 1: Covalent ligand patterning by photobleaching

A) Application examples for 2D surface modification by micropatterning. i) Control on adhesion influenced, haptotactic cell migration on gradients of adhesion cues. Scale bar 100 µm ii) Control on cell number, shape and density by single cell adhesion grids. Scale bar 200 µm. iii) spatiotemporal control of cell migration by 2 step surface adhesion. Scale bar 250 µm. B) Schematic of building block based photo-patterning. i) Surface immobilization of photocrosslinker labeled linker molecules by photo-immobilization. ii) Immobilization of ligands via adapter system. C) Cu(I) catalyzed 1,3 dipolar cycloaddition as adapter system of soluble, ligand bearing azides (N3) and photo-immobilized alkynes for covalent ligand binding. Small, ~70 Da triazole adapter between surface and immobilized dye. D)

Passivating hydrogel layer (polyvinyl alcohol, PVA). PVA polymer covalently bound to amino-silanized glass surface, forming a hydrated, passivating layer.

3.3.2 Photoreactive molecules

Photoreactive subunits can be selected from a plethora of photoreactive molecules (Table 1) which, in their activated state, form highly reactive intermediates, such as radicals, carbenes and nitrenes. Fluorescent dyes represent a very easily accessible class of photoreactive molecules. Activated at their specific absorption maximum, fluorescent dyes can fragment and form unspecific and often long lived radicals [26] which in turn are able to react with many surfaces. This “photobleaching” process leads to an effective immobilization of the fluorescently tagged linker. Bleaching-prone dyes, such as 6-FAM thereby bind with higher efficiency than modern, bleaching-resistant ones [28]. Due to slow kinetics and the possibility of unspecific dye-fragmentation and multimerization, fluorescent dyes are prone to produce high unspecific background binding and are often excitable by the full fluorescent spectrum, leading to detectable background auto fluorescence after immobilization.

Norrish Type II photoinitiators, such as 4-Benzoylbenzoic acid are widely used as photocrosslinking molecules [29, 30] due to their crosslinking capabilities and fast reaction kinetics. However, with absorption maxima around 300 nm, activation necessitates light sources with high intensities in the UV-B range and therefore special optics and filters. Additionally, solubility in aqueous solution is rather poor, limiting the available working concentrations. Diazirine-based photoreactive molecules can be activated at wavelengths in the UV-A range, show fast reaction kinetics and no autofluorescence after reaction. Due to their small size, solubility of the linker molecule in aqueous solution is not hampered by the addition of a Diazirine [31-33].

	AbsMAX	kinetics	Auto-fluorescence	commercial availability
Fluorescent Dye				
e.g. 6-FAM	470 nm	slow	yes, full spectrum	yes
Norrish Type II Photoinitiators				
e.g. 4-Benzoylbenzoic acid based	~300 nm	slow	yes, blue spectrum	yes
Diazirine based	~360 nm	fast	no	used in commercial crosslinkers [33]

Table 1: Photoreactive Subunits

3.3.3 Click chemistry of the adaptor system adapter

Due to their covalent character, versatility and specificity, we chose 3+2 cycloadditions such as the alkyne/azide 'click' system serving as a chemical adapter system to connect a surface immobilized linker with a biologically relevant ligand (Fig. 1C and Table 2) [34]. Here, azide-conjugated molecules or proteins are covalently attached to photo-immobilized alkynes or vice versa. Azide- or alkyne-modified dyes, amino acids, proteins and nucleic acids as well as labeling reagents and kits are commercially available and inexpensive due to the rising importance of click-chemistry related techniques. Using strain aided cycloaddition reactions [35], reactions can be carried out without the use of catalysts such as copper(I) salts. Replacing the terminal alkyne by BCN (bicyclo[6.1.0]nonyne) for example, allows the ligand immobilization in cell culture medium at physiological conditions. Therefore, through sequential photopatterning, two step adhesion experiments, where certain areas are functionalized with the binding motif in the presence of cells, are possible.

Crosslinker	Ligand	Catalyst necessary	catalyst	side reactions
terminal Alkyne	Azides	yes	Na-Ascorbate, CuSO4, BTTAA	orthogonal in physiological millieu
strained Alkyne				
DBCO	Azides	no	-	orthogonal in physiological millieu
BCN	Azides	no	-	orthogonal in physiological millieu
terminal Azide	Alkynes (strained and terminal)	depending on Alkynes used; see above	-	orthogonal in physiological millieu

Table 2: Adapter chemistry

3.3.4 Ligand

In contrast to micro contact printing, photopatterning does not necessarily require the use of bulky proteins for cell adhesion, although it is still an option [29, 36, 37], but can implement adhesive components such as Small Binding Motifs (SBMs) [38]. SBMs are short amino-acid sequences of large ECM proteins, which are high-affinity integrin-ligands and therefore cell adhesive. One of the most commonly used SBMs is the RGD (arginine-glycine-aspartic acid) motif, found in many well-characterized ECM proteins like fibronectin or collagen. RGD peptides or similar SBMs are often preferred over complete ECM proteins, in regards to cell adhesion, due to their higher solubility and lower sensitivity to denaturation [39-41]. However, not all integrins are adhesive to RGDs, including laminin-binding, collagen-binding and Leukocyte integrins [42]. Furthermore, RGD-binding integrin subtypes exhibit different affinities for RGDs. For example, integrins αvβ3 and α5β1 are high-affinity RGD targets while αvβ6, αvβ8 and αIIbβ3 integrins show lower binding to RGDs [43, 44]. Moreover, integrin expression is highly variable according to the cell and tissue type, for example platelets primarily express αIIbβ3 integrins or leukocytes express leukocyte integrins and are therefore less likely to bind to RGDs [44]. In the current study we test cells with high RGD affinity such

as 3T3 fibroblasts, zebrafish keratocytes, and renal cell carcinoma (RCC) cells that adhere to our RGD-coated surface very efficiently. We also use Human Microvascular Endothelial Cells (HMEC), which exhibit lower RGD affinity but increasing the RGD density on the surface significantly improves attachment. Furthermore, for cells types expressing integrins that are not adhesive to RGDs there are multiple other ligand options, i.e. GFOGER sequence from collagen 1 [45], A5G81 and YGISR sequences from laminin [46], that are still compatible with this photopatterning process. Thus, the applicability of this method is not limited to the cell lines tested here or to cell lines highly adhesive to RGDs but can incorporate a wide variety of cell types.

In this study we chose different commercially available RGD versions to induce cell adhesion on passivated, cell repellant surfaces (Table 3). Linear RGD sequences, such as GRGDS (glycine-arginine-glycine-aspartic acid-serine) motif, are commercially available and can easily be fluorescently tagged (Hilyte555-GRGDS). The integrin activation capability however was shown to be increased if not only motif sequence, but also motif structure of the native ECM protein is mimicked [41, 47]. Therefore, a cyclic RGD motif variant (cRGD) was used as well.

	Matrix protein	**Sequence**	**Fluorescence**	**commercial availability**
GRGDS*	Fibronectin	Integrin binding sequence	no	yes
Hilyte555-GRGDS	Fibronectin	Integrin binding sequence; dye coupled	λ_{MAX} 566 nm	no
cRGD**	Fibronectin	cyclic integrin binding sequence	no	yes

Table 3: Adhesion Ligands. * glycine-arginine-glycine-aspartic acid-serine, ** cyclic arginine-glycine-aspartic acid

3.3.5 Passivation

Especially for surface immobilization of adhesive ligands, covalent attachment is crucial to enable proper force transduction of the cells onto the substrate. Similarly, sustainable passivation is necessary to avoid uncontrolled background adhesiveness. For surface passivation, highly hydrophilic and passivating polyol-based hydrogels which can be bound covalently to the underlying surface are favored. Thin polyol films are offering excellent anti-adhesive properties over long time periods and, in contrast to passivating monolayers, such as PEG based self-assembled monolayers or Block polymers [48-50], can be efficiently modified by photo-bleaching [18, 51]. Furthermore, polyol films do not alter imaging properties of the underlying imaging bottom. In this study we use commercially available polyol coated 8 Well- and channel slides (µ-Slide VI $^{0.4}$ Bioinert and µ-Slide 8 Well ^{high} Bioinert, ibidi GmbH) as well as polyvinyl alcohol (PVA) coated, aminosilanized glass coverslips. (Fig. 1D, [52]) as cell repellant base material.

3.3.6 Illumination

In order to create 2D patterns, the photoreactive crosslinker needs to be illuminated and therefore excited locally on the passivated surface. Illumination can be carried out by different devices depending on the application, technical adaptivity, resolution and throughput requirements (Table 4). While microscope based illumination allows for high resolution due to the microscope optics, collimated light sources like LEDs can illuminate large areas and therefore allow for high throughput illumination. For structuring the illumination, microscope based approaches use scanning lasers or Spatial Light Modulators (SLMs, e.g. LCD projectors). Both allow for gradual tuning of illumination intensities, which result in immobilized ligand concentration gradients.

The power of the presented building block based micropatterning approach is the versatility regarding applications and substrates. In the following sections, different combinations of photoreactive linkers, coupling chemistry and illumination setups are used to create micropatterns for very specific applications.

Collimated LED (Photomask based)	Scanning Laser	LCD Projector
collimated lense	advanced optics	advanced optics
any lightsource possible	Laser	any lightsource
cheap and simple setup	expensive setup	expensive setup
high throughput	low throughput	low throughput
fast	slow	Slow
low resolution	high resolution	medium resolution
no intensity gradient possible	intensity gradient possible	intensity gradient possible

Table 4: Illumination devices

3.3.7 Development and assessment of single photopatterning technique using different cell lines

3.3.7.1 Generation of concentration gradients to study haptotactic cell migration

Haptotactic cell migration is a crucial biological process, for example in immunology and development [53-55]. Cellular mechanisms underlying haptotactic cell migration are still not fully understood. In order to understand those mechanisms, we sought to create concentration gradients of cell adhesive ECM Ligands offering defined shapes and local concentrations. As passivated, cell repellant surface we coated glass coverslips with a thin layer of PVA Hydrogel [18]. 6-FAM-alkyne was used as photocrosslinker which was immobilized on the PVA coated glass via structured illumination (Fig. S1A). Patterns and gradients were generated by a 470 nm LED light source and a controllable LCD panel of a commercially available projector inserted into the light-path of an epi-fluorescence microscope [56]. The photocrosslinker 6-FAM-alkyne with its absorption maximum at approximately 470 nm allowed us to use blue light instead of UV light for photopatterning. Thus, expensive UV light compatible SLMs and optics

could be avoided. In order to visualize and quantify the generated pattern and gradients during the experiment, azide-conjugated linear fibronectin-SBM-GRGDS carrying a fluorescent tag (HilyteFluor555) was used as cell adhesion ligand (Fig. S1A, B).

In a first step we tested different illumination times and analyzed the amount of surface-bound SMB. Increasing the duration of illumination at maximal power showed a surface saturation of 6-FAM-alkyne at high illumination times, and subsequently GRGDS-HilyteFluor555 (referred to as RGD-HF-555 for simplicity) and a simultaneous increase in background fluorescence. This results in an optimal illumination time of 10 min where the contrast between fluorescent signal in the illuminated regions and the background is at its maximum (Fig. S1C). With this set-up a maximal concentration of 653±24 molecules/μm^2 could be achieved at 10 min of illumination (Fig. S1D).

Next, we tested the bioactivity of immobilized RGD-HF555 and the effectivity of the cell repellant PVA coating. Therefore, we printed RGD-HF555 patches offering ideal adhesiveness for migrating zebrafish keratocytes and adhesive growing 3T3 mouse embryonic fibroblasts (3T3 fibroblasts) respectively (Fig. 2A). Zebrafish keratocytes and 3T3 fibroblasts only adhered in the RGD-HF555 patterned areas (100 % relative light intensity). Adhesion in non-patterned areas (0 % relative light intensity) was only rarely observed (Fig. 2B). Similar to adhesion, zebrafish keratocyte migration was confined to RGD-HF555 patterned regions, as illustrated by cell trajectories (Fig. 2C). Although highly motile, the cells were not able to cross the RGD-HF555/PVA interface and were forced to repolarize and change direction (Supplementary movie SM1). 3T3 fibroblast growth within the patterned regions was stable also in long-term cultures grown beyond confluency (Fig. 2C). This verifies the long-term stability of the covalent PVA surface passivation and, accordingly, the RGD-HF555 immobilization on PVA, making this set-up suitable for long-term experiments.

Fish keratocytes show an oval, fan-shaped morphology when migrating. To Influence their cell spreading and eccentricity, the available adhesion area can be changed. To illustrate this, we spatially confined migration of fish keratocytes on alternating wide and narrow regions of RGD-

HF555 (Fig. 2D-F). In 35 µm wide areas, cells showed a fan like lamellipodium that collapsed in narrow, 15 µm wide constrictions (Fig. 2E and Supplementary movie SM2). In 15 µm wide areas with 5 µm constrictions (corresponding to half a cell diameter), parts of the lamellipodium protruded along the constriction, trailing the bigger cell body to the next, wide area (Fig. 2F and Supplementary movie SM3). For both geometries, cells moved only on patterned areas, avoiding passivated background areas.

By using an SLM modified microscope as illumination system gradients of different shape and intensity can easily be patterned. The precise control of concentration gradient properties, such as shape and steepness of signaling or adhesive cue gradients is essential for understanding processes like haptotaxis [10, 57]. To illustrate the ability to generate arbitrary homogenous gradients, we patterned concentration gradients of RGD-HF555 differing in maximal concentration and steepness by changing the illumination time (Fig. 3A). The ability to create gradients of different shape is illustrated by patterning squares with linearly and exponentially decreasing concentrations of surface bound RGD-HF555 (Fig. 3B). This is a big advantage of the presented photo-patterning approach as forming such gradients within a protein coating set-up is very demanding and hard to achieve.

3T3 fibroblasts adhering to linear and exponential RGD-HF555 gradients migrated and grew in a polarized fashion in direction of maximal RGD-concentration (Fig. 3C and Supplementary movie SM4). Similarly, highly motile zebrafish keratocytes migrated preferentially in areas of a linear RGD-HF555 gradient where adhesiveness was highest for the assayed concentration range (Fig. 3D and Supplementary movie SM5). Hereby, cell trajectories shifted to highest RGD-HF555 concentrations over time (Fig. 3E) demonstrating haptotactic behavior of zebrafish keratocytes on gradients of RGD-HF555.

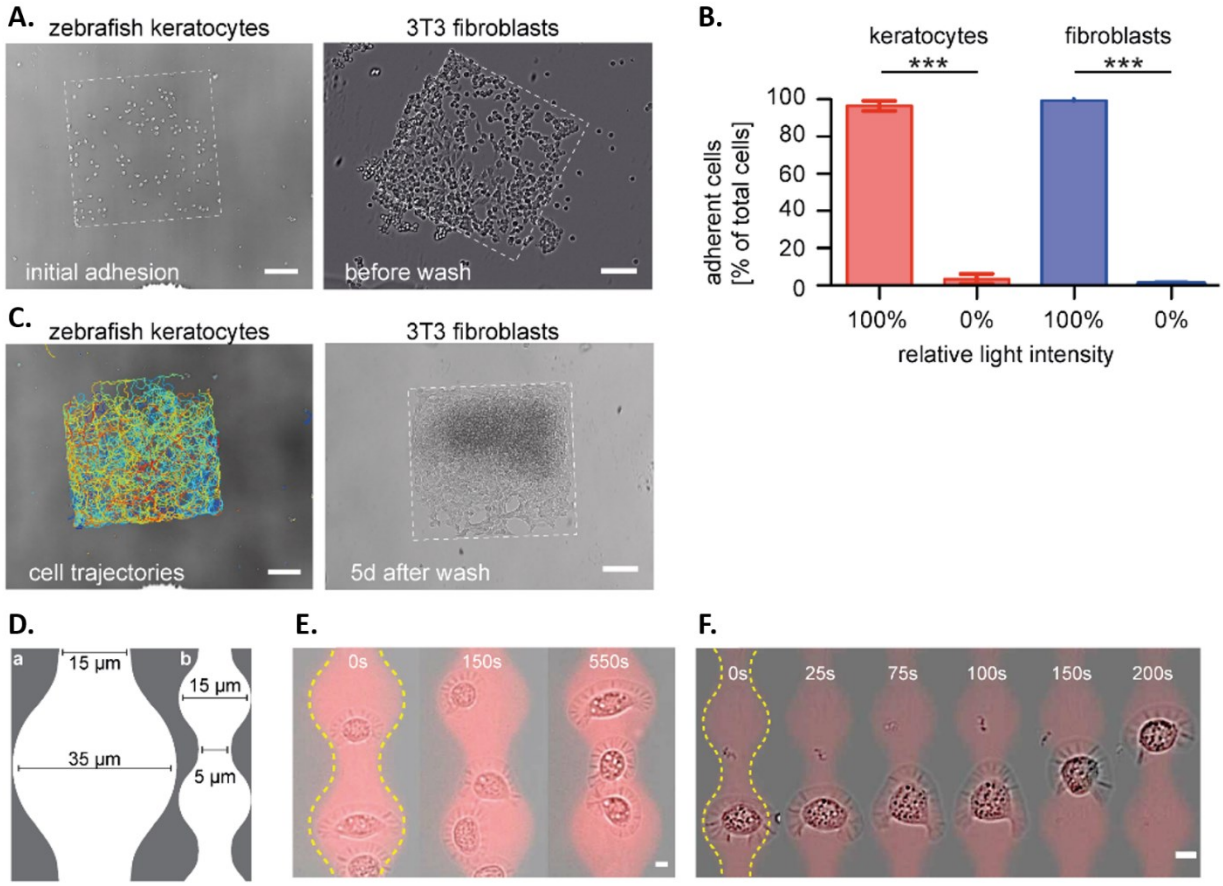

Figure 2: Characterization of RGD-HF555 photopatterning on passivating PVA coating as tool for probing cell migration

A) Brightfield images of zebrafish keratocytes and 3T3 fibroblasts (t = 3h after seeding (before wash)) adhering and growing on square patches of RGD-HF555. Scale bar 100 µm B) Fraction of zebrafish keratocytes (red bars, $p < 0.0001$) or 3T3 fibroblasts (blue bars, $p < 0.0001$) adhering on (100 % Intensity) or next to (0 % Intensity) 450 µm x 450 µm square patches of RGD-HF555. C) Zebrafish keratocytes migrating on a patch of RGD-HF555 printed on PVA background. Cell trajectories after t = 2 h. Scale bar 100 µm. D) Brightfield image of 3T3 fibroblasts on square patches of RGD-HF555 grown for 5 days. Scale bar 100 µm E) Template for alternating wide and narrow adhesive areas influencing cell shape changes during migration. F) Zebrafish keratocyte migrating on 35 µm wide areas of RGD-HF555 with 15 µm constrictions. Scale bar 5 µm. G) Zebrafish keratocyte migrating on 15 µm wide areas of RGD-HF555 with 5 µm constrictions. Scale bar 5 µm.

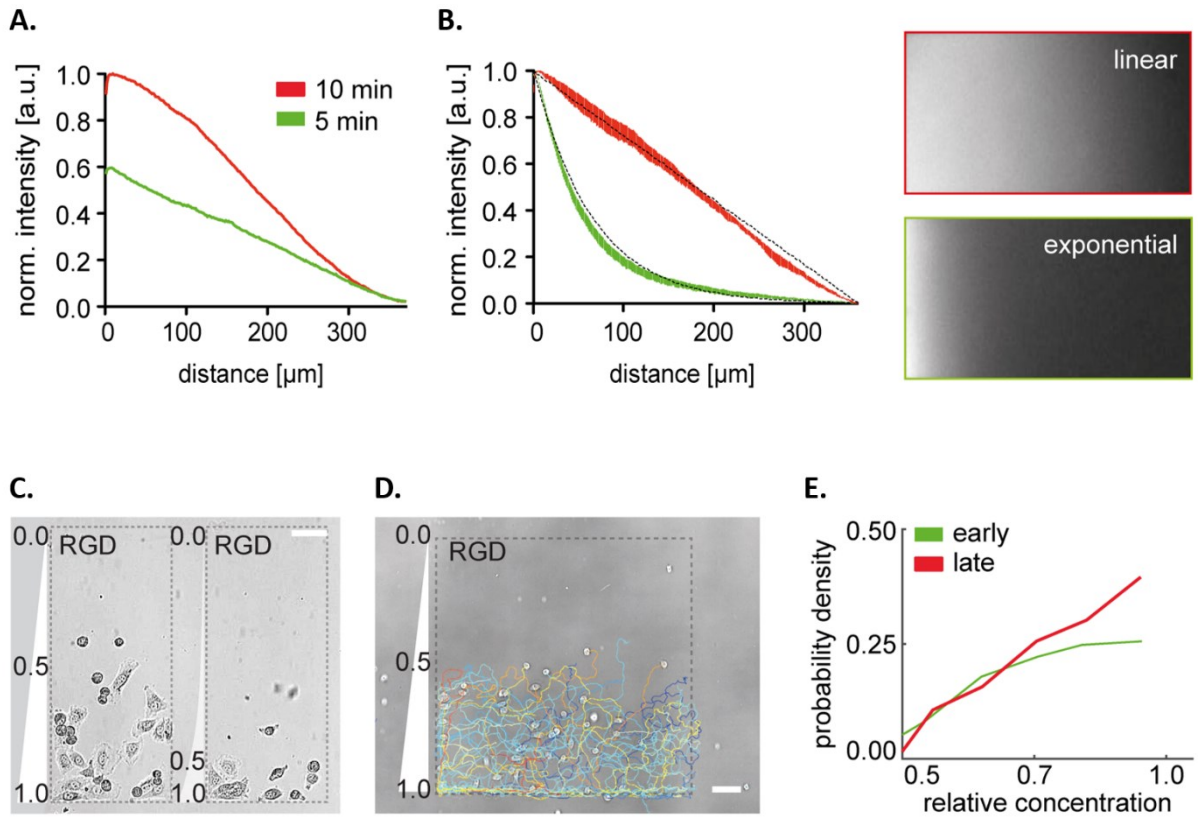

Figure 3: Photo-patterning of concentration gradients of surface immobilized RGD-HF555 on passivating PVA coating as tool for probing haptotactic cell migration

A) Normalized intensity profiles of linear gradients of RGD-HF555. Gradient steepness dependent on 470 nm LED exposure time. Green profile: 5 min exposure time. Red profile: 10 min exposure time. B) Normalized intensity profiles of linear and exponential like gradients of RGD-HF555. Green profile: 5 min exposure time, exponential mask. Red profile: 5 min exposure time, linear mask. For (C)-(E) Relative RGD-HF555 concentration is given as relative light intensity. C) Brightfield image of 3T3 fibroblasts adhering and migrating on linear (left) and exponential (right) gradients of RGD-HF555. Scale bar 50 µm. D) Brightfield image of zebrafish keratocytes migrating on a linear gradient of RGD-HF555. Scale bar 50 µm. E) Time dependent zebrafish keratocyte trajectory distribution within a linear gradient of RGD-HF555. Early: t = 0 - 60 min and late: t = 61 - 120 min (n = 5 independent experiments).

3.3.7.2 Use of collimated LED for high-throughput photopatterning

Microscope objective-based illumination systems like the one used above are flexible but rely on sequential illumination, thereby limiting the throughput in generating photopatterns. In biological and pharmaceutical applications, including screenings on 3D cell cultures or single

cells, multiple parallel measurements are often desirable [58-61]. For these applications large areas need to be structured in a short time period. For such purpose we devised a simplified structured illumination setup, consisting only of a collimated LED light source and a photomask (Fig. S2A). Here a whole Microslide, or even Microplate can be illuminated simultaneously. The optics of the SLM / microscopy setup are also not compatible with UV excitable photoinitiators. Instead, collimated LEDs with emission at 360 nm are commercially available for very low prices. Thereby, the use of collimated LEDs allows the implementation of non-fluorescent photocrosslinking subunits with high activity in the UV range, such as diazirine derivatives. In the following pattering approach, we photo-immobilized a diazirine-alkyne linker on commercially available, hydrogel passivated µ-Slides (µ-Slide IV $^{0.4}$ Bioinert, ibidi GmbH) and subsequently functionalized the linker with a cyclic RGD-Azide (Fig. S2B and C).

With this set-up, the patterning of large areas is feasible and was used to generate adhesion-arrays of single cell sized (35 µm) and multicell sized (200 µm) adhesion pads within a passivated flow-channel (Fig. 4A). Cell seeding in the channel system results in a very homogenous distribution of cells on the pattern due to the laminar flow conditions within the microchannel. The high reactivity and short lifetime of the activated Diazirine-Alkyne linker in combination with a photomask based illumination allows for a patterning with very low unspecific binding of the linker molecule in the non-illuminated areas. This restricts cell adhesion to the patterned spots, even if grown beyond confluency to grow spheroids (Fig. 4A, large spots) or if cultured over more than two weeks on complex pattern geometries (Fig. S2D).

To quantify the patterning contrast we used a Cy3-Azide ligand to visualize the structures and compare the Diazirine immobilization with patterns generated with a 6-FAM linker and illumination with a 470 nm collimated LED (Fig. 4B). Very high signal-to-noise ratios can be generated with the Diazirine setup with a more than 3-fold increase of the signal-to-background ratio compared to the 6-FAM pattern. (Fig. 4C). The Diazirine not only produces lower background but also shows a distinct drop of Cy3- fluorescence intensity at the edge of

the pattern in contrast to the 6-FAM linker (Fig. 4D). Due to the absence of a conjugated pi-electron system within the Diazirine-Alkyne linker, the pattern does not have any inherent fluorescence (Fig. 4E) and therefore background free fluorescent live-cell imaging or Immunofluorescence readouts are possible (Fig. 4F).

This high-throughput photopatterning approach has several advantages compared to existing photopatterning methods that implement microfluidics (i.e. [62]). First of all, it allows for single-cell as well as cell colony experiments, providing the ability of performing multiple tests at a time. Secondly, the current setup has the capacity to be extended in order to generate areas of different geometry that can be treated independently, offering spatiotemporal control to the experimenter. This extension of the method is described in the following paragraphs.

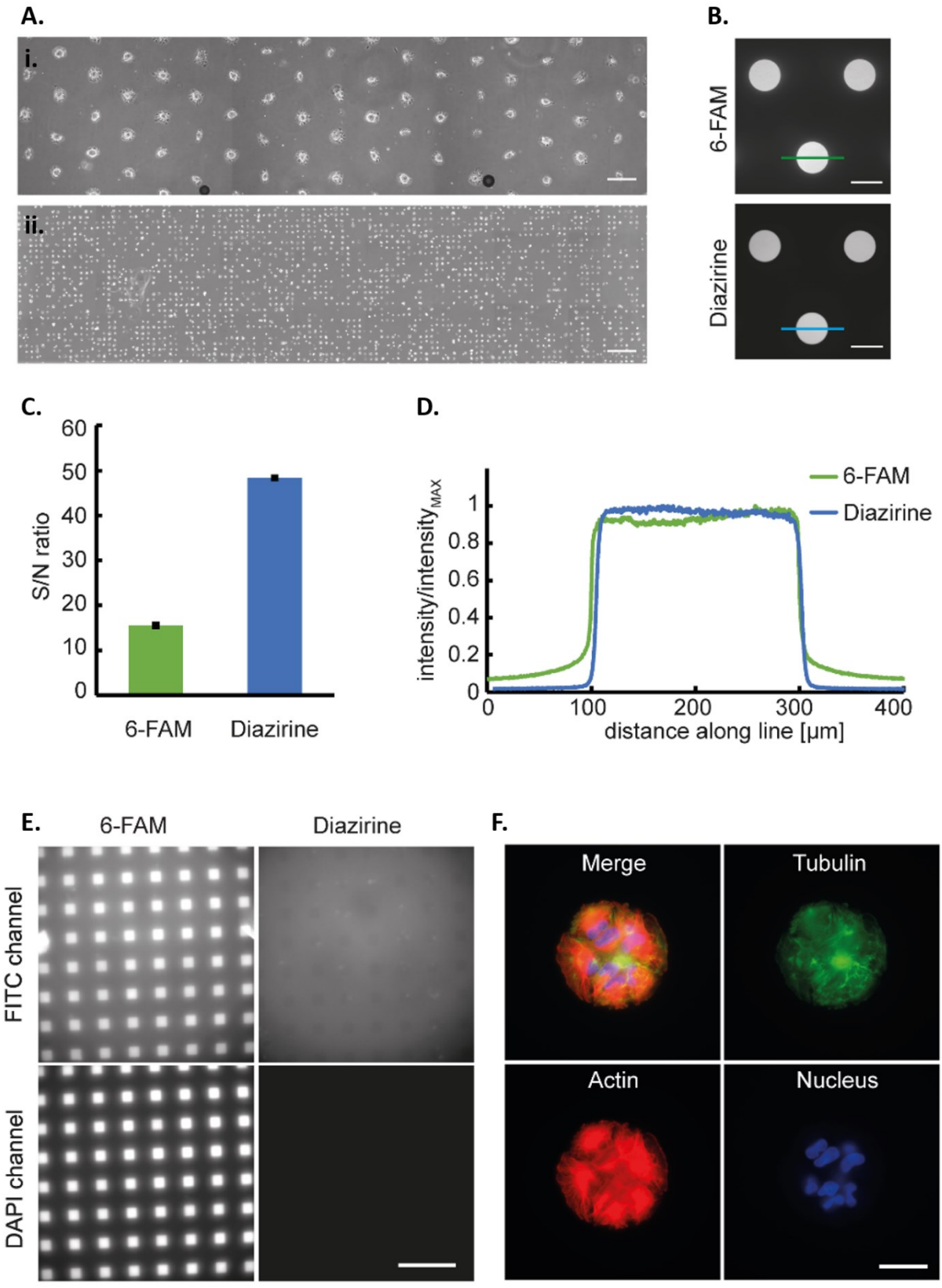

Figure 4: Use of a Diazirine-linker to generate large patterned areas with very low background immobilization and advanced fluorescent properties

A) Cells ((i) RCC, (ii) NIH 3T3)) seeded in a microchannel of an ibidi µ-Slide VI $^{0.4}$ Bioinert where the whole channel is patterned with adhesion spots of (i) 200 µm and (ii) 35 µm diameter using a collimated LED and a photomask. Images where taken (i) 3 days and (ii) 4h after seeding. Scale bar 400 µm. B) Fluorescence images of sulfo-Cy3-Azide coupled to either a photo-patterned 6-FAM Alkyne or a Diazirine-Alkyne spot. Green and blue line indicate the position of the fluorescence intensity profile from subfigure D. Scale bar 200 µm. C) Signal-to-noise ratio of 200 µm pattern generated either with 6-FAM-Alkyne or Diazirine-Alkyne and visualized by functionalizing the pattern with a sulfo-Cy3-Azide. D) Sulfo-Cy3-Azide intensity profile across a 200 µm wide pattern spot generated by structured illumination of either 6-FAM-Alkyne or Diazirine-Alkyne (profile along green/blue line indicated in Figure 3B). E) Auto-fluorescence in the FITC or DAPI channel of pattern of 30 µm wide squares generated by either structured illumination of 6-FAM-Alkyne or Diazirine-Alkyne. Scale bar 200 µm. F) Immunofluorescent staining of RCC cells on 100 µm circular pattern. Green phalloidin staining, red tubulin staining and blue DAPI staining. Scale bar 50 µm.

3.3.8 Transition from single to sequential photopatterning to generate a ‘‘dynamic‘‘ system for studying tip/stalk phenotype switch in angiogenesis

After the successful application of our building block-based single photopatterning method to confine growth and migration of cells to designated areas and gradients, this technique was further developed to allow sequential patterning. An important requirement was to temporal control to the spatial patterning. We thus introduced the capacity to pattern neighboring geometries with different functionalities. We then added the feature of activating the patterns at defined times during the experiment. We refer to this expanded method as sequential photopatterning. We assessed the applicability of our sequential photopatterning by employing a more complex cellular process, namely the tip/stalk cell phenotype switch of endothelial cells during angiogenesis. During this process (the production of new blood vessels from preexisting ones) endothelial cells differentiate into two different populations, the tip and the stalk cells [63], which are characterized by specific marker proteins. The tip cells act as guides of the sprouting blood vessel while the stalk cells follow the leading tip cells, comprising the base of the sprout [64]. Two main factors are considered responsible for inducing the tip/stalk phenotype switch: the shape-change that endothelial cells undergo during relocation, and the process of directed migration towards a target area. Our sequential photopatterning system

can control both features, as the time-controlled activation (chemically-induced cell adhesiveness) of the narrower patterned areas enables directed cell migration from the wider to the narrower adhesive areas. This we refer to as a ‘‘dynamic’’ system.

The selected pattern geometries of our "dynamic" system comprised of large 2500 µm squares and narrow 10µm wide, 150µm long lines (Fig. 5, Fig. 6, Fig. 7 A). We started the process of photopatterning by utilizing the previously discussed hydrogel-coated bioinert foil from ibidi, (Fig. 1C, Fig. 5 A iv) which prevents the adhesion of proteins or cells. Similar to our single-photopatterning process, we produced the adhesive areas by photobleaching and click chemistry, this time using a photo-sensitive fluorescent dye conjugated with an azide functional group (6-FAM-Azide, ex. 488 nm, Fig. 5 A iii and 6 A i). A custom-made chromium mask (Fig. 5 A i) left defined areas in a line-patterned fashion exposed, allowing the selective photo-bleaching of the 6-FAM dye through the exposed line areas upon strong illumination with a collimated 470 nm LED (Fig. 5 A v). The resulting pattern of Azide-covered lines will be referred to as tip areas. Following that, a second chromium mask (Fig. 5 B i) was used on the line-patterned surface which left defined 2500 µm square areas exposed. This allowed the selective photobleaching of a different dye-linker (Diazirine-Alkyne, ex. 350 nm, Fig. 5 B iii and 6 A ii) through the exposed square areas upon illumination with a 360nm collimated LED, resulting in a pattern of Alkyne-covered squares (will be referred to as stalk areas) (Fig. 5 C i). The use of a custom-made re-aligner that includes cross over square alignment markers (Fig. 5 A ii5 B ii, Fig. S3) was essential in order to precisely align the line and square patterns during illumination (Fig. 5 B v) with micrometer accuracy. This ensures that each line is connected to the middle of the right side of each square, resulting in the desired stalk/tip pattern (Fig. 5 C , 7 B). High accuracy in alignment was not trivial, as misaligned patterns could alter the outcome of our experiment.

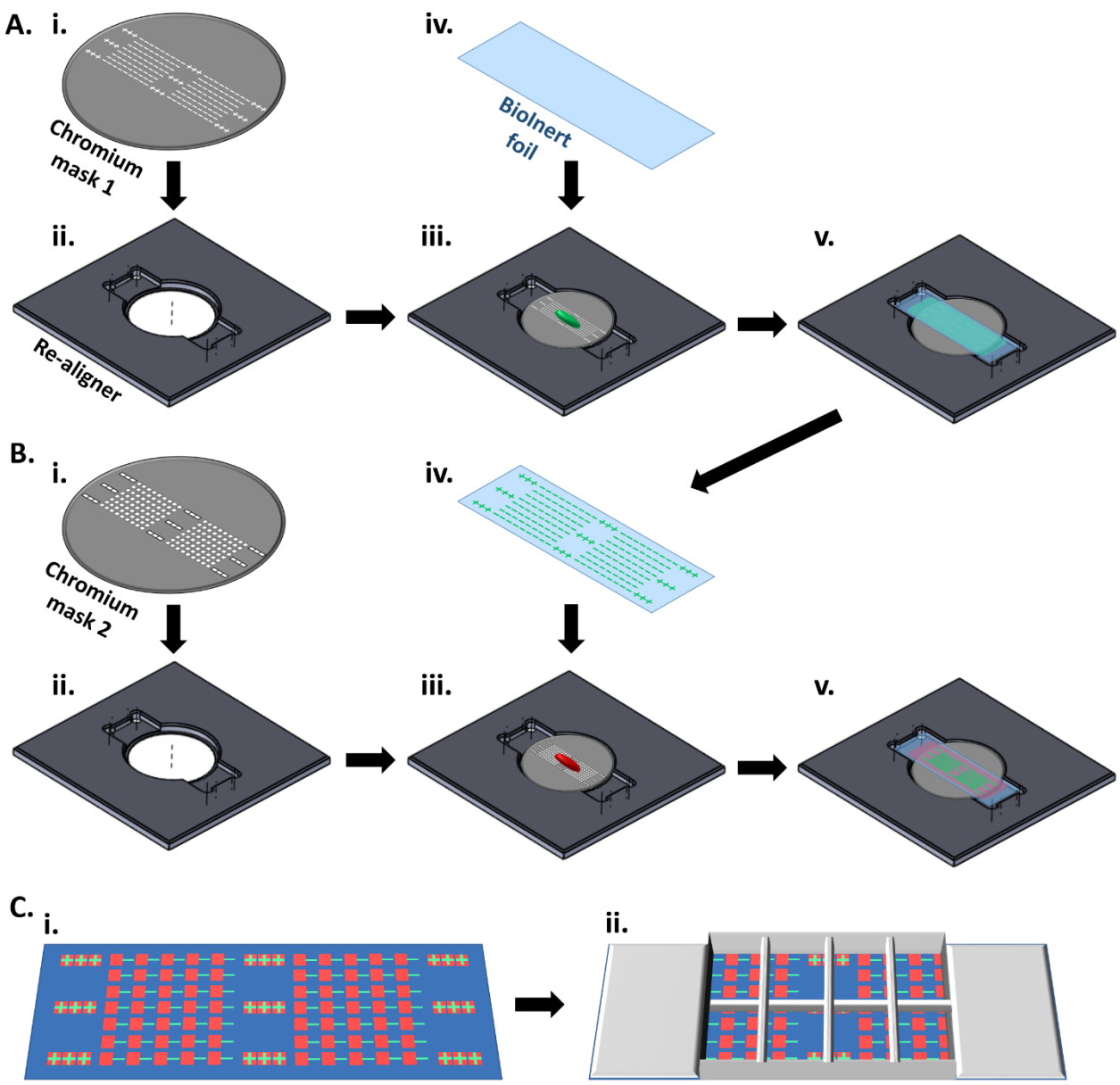

Figure 5: Schematic illustration of the sequential photo-patterning process of the "dynamic" system

A) Photo-patterning of tip area. i) Chromium mask etched in a line patterned-fashion, with cross-shaped alignment markers on either side of the main patterns. ii) Custom-made re-aligner designed to coordinate the two masks. iii) Added dye-linker (6-FAM-Azide) solution, here shown in green and iv) ibidi's Bioinert foil. v) Configuration of first mask-dye-foil, illuminated from underneath, producing the desired pattern on the foil. B) Photo-patterning of stalk area. i) Second chromium mask etched in a square patterned-fashion, with square-shaped alignment markers on either side of the main patterns. ii) Custom-made re-aligner coordinating the two masks. iii) Second added dye-linker (Diazirine-Alkyne) solution, here shown in red. iv) Line-patterned foil resulting from illumination through the first mask v) Final configuration of second mask-dye-foil, illuminated from underneath. Cross over square alignment markers were used to precisely align the foil's existing pattern with the pattern of the second mask. C) i) Resulting final line (tip) and square (stalk) photo-patterned surface on the Bioinert foil, shown in green

and red, respectively. Cross over square alignment markers shown on either side of the mail patterns. ii) Attachment of adhesive 8-well bottomless µ-Slide on the patterned surface of the foil, enabling later addition of click reaction solutions and cell seeding.

This photolithography process was followed by two different sequential click chemistry reactions that finally rendered the aforementioned patterned areas cell adhesive. For the addition of the click chemistry reaction solutions as well as the subsequent cell seeding on our foils, the attachment of an 8-well bottomless µ-Slide to the patterned surface was required (Fig. 5 C ii). The first functionalization step was the copper-catalyzed reaction between the Alkyne groups on the square areas and the Azide groups of RGD-Azide peptides that were added to the click-reaction solution (Fig. 6 B i). This enabled the following selective adhesion of HMECs only on those RGD-containing square areas, forming the initial stalk cell population (Fig. 6 B ii, 7 C). At timepoint 0, the copper-free click reaction between the Azide linker groups on the line areas and the BCN groups of the newly added RGD-BCN peptides took place (Fig. 6 C i). This resulted in the activation of the tip areas (Fig. 6 C ii), as they became cell adhesive and was considered the starting point of cell differentiation.

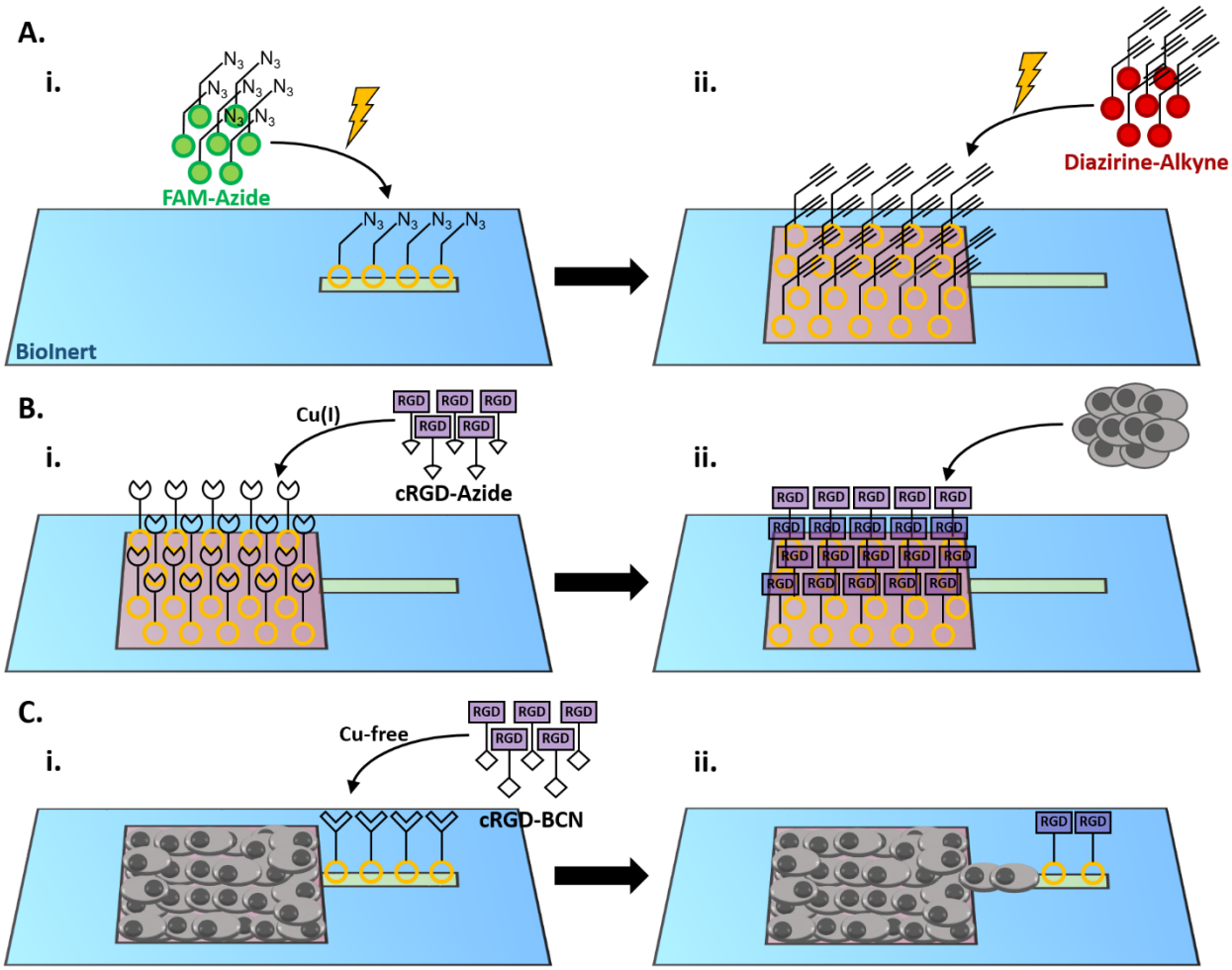

Figure 6: Detailed illustration of the photo-bleaching process and click chemistry reactions to produce sequentially cell-adhesive areas

A) Photo-bleaching for creating the tip and stalk area i) 6-FAM-Azide conjugates (left) which, upon illumination through the lines left uncovered by the first mask, attach to the surface (right). ii) Diazirine-Alkyne conjugates (right) which, upon illumination through the squares left uncovered by the second mask, attach to the surface (left). B) Click chemistry reaction for activation of the stalk areas. i) Addition of the first click reaction solution containing RGD peptides with Azide functional groups. The Azide groups form triazole links with the Alkyne groups of the Diazirine-Alkyne conjugates that are already attached to the square areas. These areas are now activated with RGD and adhesive to cells. ii) HMEC endothelial cells are seeded on the square areas forming the initial stalk cell population. C) Click chemistry reaction for activation of the tip areas. i) Addition of the second click reaction solution containing RGD peptides with BCN functional groups. The BCN groups link to the Azide groups of the 6-FAM-Azide conjugates that are already attached to the line areas. These areas are now also activated with RGD and adhesive to cells (timepoint 0). ii) endothelial cells from the stalk areas migrate to the tip areas.

According to our observations, approximately 16 hours after the tip area activation the cells in most of the patterns had already migrated halfway along the tip (representative time-lapse in Fig. 7 D). Eventually, at 24 hours after activation, all patterns had fully covered tip areas and the migration was complete (Fig. 7 E). As expected, cells were confined in the patterned areas throughout the experiment, verifying the spatial control of our method. More importantly, the ability to initiate migration at a chosen timepoint verified the temporal control provided by our approach.

In order to assess whether a phenotypic switch took place between cells in the tip and stalk areas, we fixed the cells at 16h post-activation and used immunohistochemistry to visualize the levels of protein markers corresponding to each phenotype. More specifically, we visualized proteins that are known components of the Notch signaling pathway, namely Hey1/ Jagged1 associated with stalk phenotype and Dll4/ ADAMTS1 related to tip phenotype [65]. For each of the aforementioned markers we calculated the fluorescence intensity ratio between the tip (line) and stalk (upper or lower square) compartments (Fig. 7 F). The upper half of the square was considered as an intermediate compartment where some cells might transition from stalk to tip phenotype. Regarding the known tip cell markers Dll4 (Fig. 7 F i) and ADAMTS1 (Fig. 7 F ii), we found that their fluorescence intensity was 4.21 and 5.03 times higher, respectively, in the line compartment compared to the lower square compartment, ($p<0.05$). Moreover, the intensity of ADAMTS1 also showed a 4.74- fold increase in the line compartment compared to the upper square compartment ($p<0.05$), which was not the case for Dll4. However, for both tip markers there was no significant difference in the fluorescence intensity between the upper and lower square or line+ upper to lower square compartments, as shown by the corresponding calculated ratios (Fig. 7 F i, ii). Therefore, the expression of the tip markers Dll4 and ADAMTS1 is strongly associated with our designated tip area. On the other hand, for the stalk marker Jagged1 (Fig. 7 F iii), fluorescence intensity was 2.04 and 2.17 -fold lower in the line compartment compared to the upper and lower square compartments, respectively ($p< 0.0001$). In addition, this marker showed a 1.4- fold intensity

reduction in the line+ upper square compared to the lower square compartment ($p < 0.0001$). Our fluorescence intensity measurements of the Hey1 stalk marker (Fig. 7 F iv) exhibited similarities with the Jagged 1. More specifically, Hey1 fluorescence intensity was 2.5 and 2.4 times lower in the line compartment compared to the upper and lower square compartments, respectively ($p < 0.0001$). Moreover, Hey1 had a 1.38-fold drop in the fluorescence intensity inside the line+ upper square areas compared to the lower square compartment ($p < 0.0001$). For both stalk markers, fluorescence intensity comparisons between the upper and lower square compartments showed no significant differences. Thus, the expression of the stalk markers Jagged1 and Hey1 is associated with our designated stalk areas and even more so to the lower square compartment, which is more clearly a ‘stalk’ compartment, being further away from the tip area. These findings show that our "dynamic" system was efficient in inducing a predominance of tip cell phenotype in the tip area and stalk cell phenotype in the stalk area, verifying its applicability in studying dynamic cellular behavior.

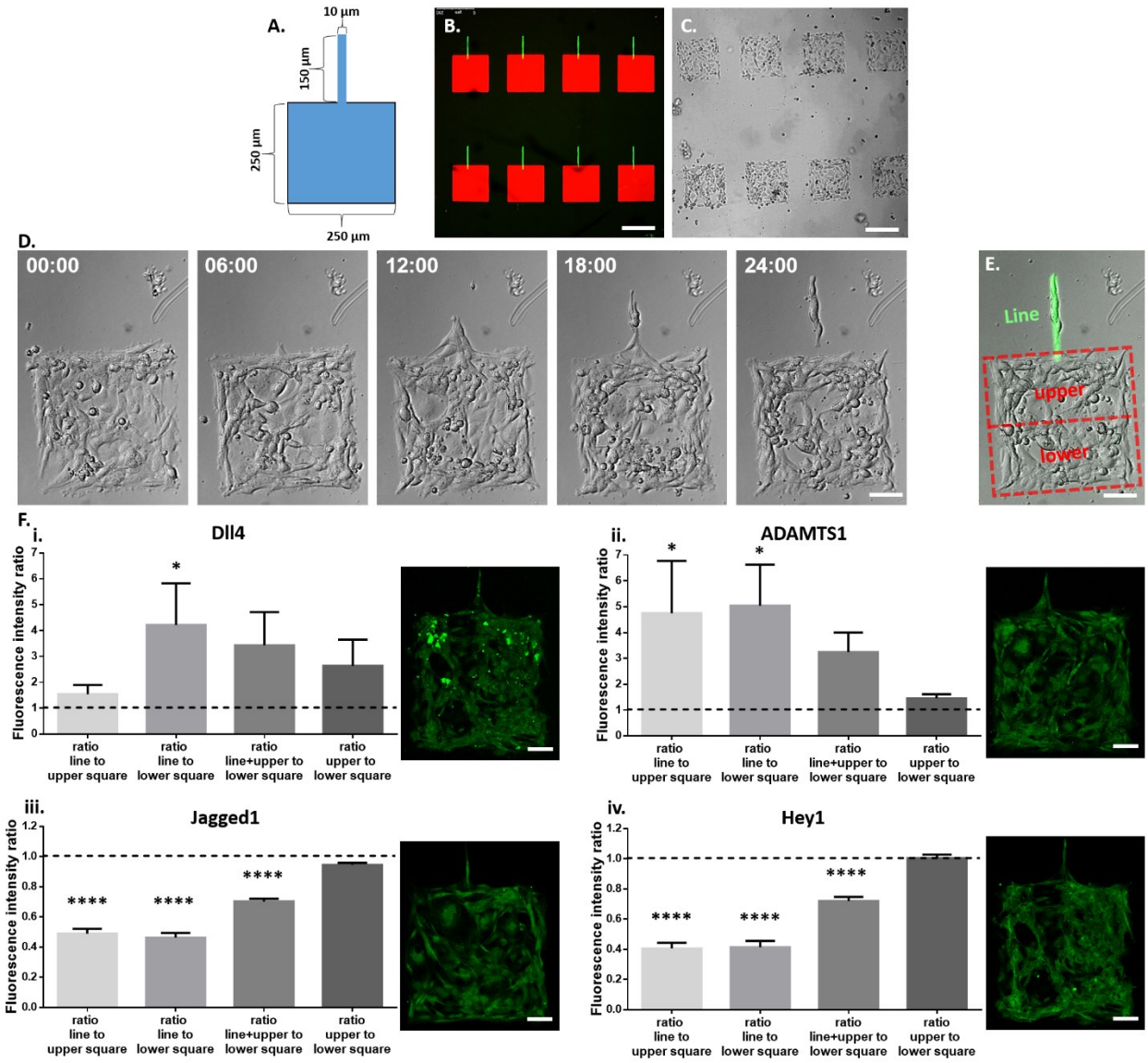

Figure 7: Cell adhesion on the "dynamic" system created by sequential photopatterning and evaluation of tip/stalk protein marker expression

A) Schematic illustration of the geometry and dimensions of the "dynamic" system generated using sequential photopatterning. B) Confocal images of Diazirine- patterned square areas labeled with DBCO-Sulfo-Cy5 (red) and residual intensity of 6-FAM-patterned line areas (green). Scale bar: 250 µm. C) Bright-field microscopy image of HMECs adhering on the patterned surfaces D) Time-lapse of cell migration to the tip. E) Overlay of bright-field microscopy image and fluorescence microscopy image showing the residual fluorescence of the line area (green). Red dashed outline shows the upper and lower square (stalk) compartments and green fluorescent line shows the line (tip) compartment. F) Left panels: Quantitative analysis of expression of the tip-related markers Dll4 (i), ADAMTS1 (ii) and the stalk-related markers Jagged1 (iii), Hey1 (iv). Here, for each marker the fluorescence intensity ratios between the different compartments of the patterned area (line, upper square, line+upper square, lower square) were determined. Bars represent the mean ratios of the "dynamic" system +SEM. Statistical

significance was assessed using 1-way ANOVA followed by Uncorrected Fisher's LSD test. i) Dll4: line/upper $_{mean}$ = 1.54, p= 0.71; line/ lower $_{mean}$ = 4.2. p=0.03; line+upper/ lower $_{mean}$ = 3.42, p=0.1; upper/ lower $_{mean}$ = 2.63, p=0.27 (n=9) ii) ADAMTS1: line/upper $_{mean}$ = 4.74, p= 0.03; line/ lower $_{mean}$ = 5.03. p=0.02; line+upper/ lower $_{mean}$ = 3.24, p=0.19; upper/ lower $_{mean}$ = 1.44, p=0.79 (n=7). iii) Jagged1: line/upper $_{mean}$ = 0.49, p<0.0001; line/ lower $_{mean}$ = 0.46, p<0.0001; line+upper/ lower $_{mean}$ = 0.70, p<0.0001; upper/ lower $_{mean}$ = 0.94, p=0.08 (n=15). iv) Hey1: line/upper $_{mean}$ = 0.40, p<0.0001; line/ lower $_{mean}$ = 0.41, p<0.0001; line+upper/ lower $_{mean}$ = 0.72, p<0.0001; upper/ lower $_{mean}$ = 1.00, p=0.90 (n=24). n.s.: non-significant, * p<0.05, **** p<0.0001. Right panels: Exemplary fluorescence microscopy images of cells stained for the corresponding marker that is quantified in the left panel. Scale bar: 50 µm.

3.3.9 Comparison between "dynamic" and a control "static" system

We then moved on to comparing the "dynamic" system to a control "static" system that can induce a similar shape change but does not allow for time-controlled directed migration. This ‘‘static’’ system, was generated using standard microcontact printing as described previously [15, 66] and involved the same patterned geometries as the “dynamic“ system (SI and Fig. S4). We found that the “static“ system was able to induce an increase in the Hey1 mRNA expression in the square compared to the line compartment (SI and Fig. S4, detailed description of mean differences and p values in the table S1, S2) This was a first indication that the cell-shape change induced by the different surface geometries affected the tip-stalk ‘’status’’ of the endothelial cells on the level of gene expression. To further investigate a possible phenotypic switch, we calculated the tip and stalk protein marker fluorescence intensity ratios between the line and the square compartments, as we did for our "dynamic" system. In the case of the tip marker Dll4 (Fig. S5 D i), its fluorescence intensity was 1.21-fold higher in the upper compared to the lower square compartment (p< 0.01) but no significant differences in intensity were observed between the other compartments. With regards to the tip marker ADAMTS1, the intensity was 1.38 times higher in the line compared to the lower square compartment (p<0.05) while no significant difference between the other compartments was observed (Fig. S5 D ii). On the contrary, for the stalk markers Jagged1 and Hey1 there was no significant variation in their intensity between the different compartments (Fig. S5 D iii-

iv). The small increase in the ADAMTS1 marker expression in the line compared to the lower square compartment shows that the shape change factor alone can slightly promote a tip phenotype in the tip area. The Dll4 marker was less specific for the designated tip area, being slightly increased in the upper square, proximal to the line compartment but not inside it. Furthermore, the lack of significant difference in both stalk marker expression between the tip and stalk designated areas suggests that the cell-shape change factor is less efficient in inducing a robust and complete tip-stalk phenotype switch when the directed migration component is missing.

Direct comparison between the two systems revealed that the “dynamic” system was significantly more sensitive compared to the “static” system in identifying differences in the expression levels of all markers between the different compartments, here expressed as the ratios of their fluorescence intensities (Fig. S6). The increased sensitivity of the “dynamic” system in detecting such differences compared to the “static” system can be attributed to the factor of directed migration, which only the "dynamic" system provides in addition to the shape change factor that both systems incorporate. Such a "dynamic" system that allows time-controlled directed migration is required to fully and reliably model "dynamic" processes.

3.4 Conclusion

In this study we introduce a building block based covalent photopatterning technique that stands out due to its robustness and versatility in using different linkers, ligands and illumination systems, tailored to the biological application needed. Using sequential illumination steps with different linkers and functionalization of the created structures in the presence of cells, complex dynamic cell processes, like e.g. tip/stalk cell switch in angiogenesis, can be mimicked. The efficacy of our system in imitating such a process underscores the experimental advantage of achieving temporal as well as spatial control over

the cell microenvironment *in vitro*, suggesting that this setup could be adapted to answer various biological questions.

3.5 Supplementary Information

3.5.1 Supplementary Methods:

3.5.1.1 Classic microcontact printing process to generate a ‘‘static’’ system as control

For the generation of the ‘‘static’’ system we designed four types of patterns with different geometries that provided cell shape change-inducing conditions. Two of them were composed of large 2500μm² squares (stalk areas) directly connected to narrow 10μm-wide lines (tip areas), either 150 μm- or 300μm- long, as illustrated in Fig. S4 A, B. The other two types involved the same squares and lines as mentioned above, but connected through an intermediate triangular area, as shown in Fig. S4 C, D.

In all cases, aμ-Slide 8 Well uncoated (ibidi, Martinsried, Germany) underwent 3 min of oxygen plasma treatment (Plasma cleaner typ ‘‘ZEPTO,’’ Diener electronic, Ebhausen, Germany) at 0.3 mbar for activation (generation of OH-hydroxyl bonds). Then, 250 μl/well of 0.05 mg/ml fibronectin (R&D Systems, US) solution in MilliQ were added to the now highly reactive surface and incubated at room temp for 2 hours. After washing 2 times with 500 μl of milliQ H2O the surface was allowed to dry. Following that, we used standard microcontact printing techniques to create PDMS stamps with 4 different patterns (square with short line, square with long line, square with short line + intermediate area and square with long line + intermediate area). One stamp was placed at the center of each well and the surface was plasma treated one last time at the same conditions as before. This step removes all fibronectin from the surface except the areas that are protected by the stamp, so all the unprotected areas on the surface become hydroxylated and highly reactive again. Without removing the stamps, a 7 μl drop of 1mg/ml

PLL(20)-g[3.5]- PEG(2) (Susos AG, Switzerland) solution in MilliQ was added right next to each stamp allowing surface tension to absorb the liquid underneath the stamp. The above condition was allowed to settle for 45 min. The stamp was gently removed and washed 2 times with 500 µl of MilliQ. Now the aforementioned patterned areas contain fibronectin and are highly cell-adhesive while the surrounding areas are cell repellent. At this point, HMEC cells were trypsinized after reaching confluency, diluted to the desired density (70.000 cell/ml) in endothelial cell growth medium and 250 µl of this cell suspension were added in each well and allowed to settle overnight at 37 °C.

After seeding of the HMEC cells on the adhesive patterns, the cells simultaneously attached to both stalk and tip areas. As there was no unoccupied area for the cells to migrate towards, only random relocation from one area to the other occurred but no directional migration was possible (Fig S5 B, C). The cell shape transition upon passage through the line areas in this experiment mimics shape changes endothelial cells undergo as they squeeze through tight spaces during angiogenesis. We evaluated the tip/stalk cell phenotype switch in this “static” setup using the same protein markers as described in the "dynamic" system. Moreover, SmartFlares (Merck Millipore, Germany) was used as biosensor for Hey1 expression, which is a known Notch target gene related to stalk-cell phenotype. We observed a significant increase in Hey1 mRNA levels inside the stalk area compared to the tip area for both tip lengths, starting at about 20h after addition of the biosensor. The difference was more pronounced in the absence of intermediate areas for both short and long lines and was maximal at the 40h timepoint

3.5.1.2 SmartFlare live cell imaging on the “static” system

The process followed was according to the manufacturer’s manual (Merck Millipore, Germany). Before the start of the experiment, custom-made SmartFlare Hey1 Cyanine 5, RNA Detection Probe (Merck Millipore, Germany) stock solution was added to 200 µl medium of each well of HMEC seeded 8-well microcontact printed slides to reach a final concentration of

400pM. In each experiment, together with the Hey1 probe 3 types of controls were used (Uptake Control Cyanine 5, RNA Detection Probe | SmartFlare, SF-137; Scramble Control Cyanine 5, RNA Detection Probe | SmartFlare, SF-102; GAPDH; Human, Cyanine 5, RNA Detection Probe | SmartFlare, SF-136; Merck Millipore, Germany) in the same final concentration. After SmartFlare addition, live cell imaging was performed using the aformentioned slides with an Eclipse Ti inverted microscope (Nikon, Dusseldorf, Germany) with a 4x/10x phase contrast objective and a CCD camera ([DS-Qi1Mc] Nikon, Dusseldorf, Germany). The slides were inserted into a 37 °C heating and incubation system that was flushed with actively mixed 5% CO2 at a rate of 10 l/h, and the humidity was kept at 80% to prevent dehydration. The cells were imaged in bright-field and the SmartFlares were detected at a 650 nm wavelength using the integrated fluorescence LED. Time-lapse video microscopy was performed with a time interval of 10 min between images over 40 h.

3.5.1.3 Image analysis of SmartFlares on the "static" system

All images of cell incubated with SmartFlares on microcontact printed patterns were processed and analyzed using ImageJ version 1.53c software tool. After images were segmented (Trainable Weka Segmentation tool), the intensities were determined.

	Short line			Long line		
	square (stalk)	line (tip)	p value	square (stalk)	line (tip)	p value
0 hours	252,0	249,4	ns	175,7	172,8	ns
2 hours	175,5	171,8	ns	169,1	167,4	ns
4 hours	189,4	184,2	ns	189,7	183,6	ns
6 hours	210,8	198,2	ns	215,9	198,6	ns
8 hours	233,9	218,1	ns	249,1	218,7	ns
12 hours	276,8	226,0	ns	309,0	238,8	ns

16 hours	348,3	234,2	ns	403,4	267,2	ns
20 hours	424,1	251,4	p<0.05	501,0	303,2	p<0.05
22 hours	454,6	259,4	p<0.01	539,3	306,5	p<0.01
24 hours	495,6	264,4	p<0.001	599,8	325,6	p<0.001
26 hours	491,0	225,6	p<0.0001	590,8	304,8	p<0.001
28 hours	522,8	226,8	p<0.0001	621,2	303,6	p<0.0001
32 hours	578,8	264,0	p<0.0001	655,8	342,4	p<0.001
36 hours	613,3	263,7	p<0.0001	708,8	349,9	p<0.0001
40 hours	679,9	237,5	p<0.0001	744,0	366,2	p<0.0001

Table S1: SmartFlares statistical analysis, Mean ± SEM and p values of SmartFlares intensity of square (stalk) or line (tip) cells in 2 different patterns without intermediate compartment at 15 different timepoints. Statistical analysis: 2-way ANOVA followed by Sidak's multiple comparisons.

	Short line + intermediate area			Long line + intermediate area		
	square (stalk)	line (tip)	p value	square (stalk)	line (tip)	p value
0 hours	231,0	233,2	ns	202,7	202,2	ns
2 hours	184,0	184,9	ns	173,3	168,9	ns
4 hours	201,8	200,3	ns	196,1	183,8	ns
6 hours	217,7	209,5	ns	223,2	196,7	ns
8 hours	235,5	218,5	ns	257,0	208,1	ns
12 hours	254,8	222,5	ns	318,2	223,9	ns
16 hours	289,4	232,4	p<0.05	411,0	245,3	ns
20 hours	320,1	248,3	p<0.01	503,9	266,3	p<0.05
22 hours	334,4	241,5	p<0.0001	528,7	261,4	p<0.01
24 hours	351,3	253,3	p<0.0001	566,6	274,7	p<0.001
26 hours	356,2	231,8	p<0.0001	559,2	262,4	p<0.001
28 hours	381,7	241,3	p<0.0001	570,0	279,3	p<0.001
32 hours	393,0	254,1	p<0.0001	595,6	283,2	p<0.001
36 hours	393,6	271,2	p<0.0001	585,8	308,7	p<0.01
40 hours	401,7	289,2	p<0.0001	597,8	319,9	p<0.01

Table S2: SmartFlares statistical analysis, Mean ± SEM and p values of SmartFlares intensity of square (stalk) or line (tip) cells in 2 different patterns with intermediate compartment at 15 different timepoints. Statistical analysis: 2-way ANOVA followed by Sidak's multiple comparisons.

3.5.1.4 Fabrication of chromium masks masters

As for conventional µCP, a master of the desired pattern was prepared on silicone using photolithography. The accuracy of the pattern depends on the material of the photo mask: PET masks are cheap in production but have only an accuracy of some micrometers, chrome masks are more expensive but can provide accuracies in submicrometer range. For the master preparation, an adhesion promoter (TI-Prime, MicroChemicals GmbH) was applied to a silicon wafer (Si-Mat) by spincoating, first at 500 rpm for 5 s and then accelerating to 5000 rpm for 30 s. The wafer was baked for 2 min at 120°C on a hot plate. Then, a 15 µm thick layer of negative photoresist (SU-8 100, micro resist technology GmbH) was applied by spin-coating first at 500 rpm for 5 s and then accelerating to 2000 rpm for 35 s. Next, the wafer was soft baked at 65°C for 2 min and then at 95°C for 5 min. In the following step, the wafer was exposed to UV light (wavelength peaks: 365 nm, 405 nm, 436 nm) which was passed through a photo mask (e.g. Zitzmann GmbH) of the desired pattern (alternatively, a laser lithography device can be used to write the desired pattern directly in the photoresist). A 5 min post-exposure baking step was performed at 95°C in order to selectively crosslink the UV-exposed portions of the resist. Afterwards, the wafer was placed in a developer bath (mr-Dev 600, micro resist technology GmbH) for approximately 2 min. To inhibit crack formation in the photoresist layer, the wafer was baked again for 5 min at 95°C. Finally, the surface was silanized with perfluorotrichlorosilane (Sigma Aldrich) by silane evaporation.

3.5.1.5 Stamp preparation for microcontact printing

Poly(dimethylsiloxane) (PDMS) was prepared by mixing ten parts silicone elastomer with one part crosslinker (Sylgard Elastomer Kit, Dow Corning, US), and poured as a 1–3 mm thick layer onto the master and degassed in a desiccator. The coated master was then cured overnight at a temperature of 60 °C.

3.5.1.6 Design and fabrication of the PDMS chamber

The photomask design for the polydimethylsiloxane (PDMS) chamber was drawn with Coreldraw X6 (Corel corporation, US) and printed on an emulsion film transparency at a resolution of 8 µm (JD Photo Data & Photo Tools, UK). A mold of the chamber was produced by photo-lithography on a silicon wafer as described earlier with minor modification [67]. In brief, the chamber mold was spin-coated with hexamethyldisiloxane (HMDS) at 3000 rpm for 30 s and then baked at 110 °C for 1 min. Following this, the wafer was spin-coated with SU 8 GM1040 (Gersteltec, Switzerland) at 450 rpm for 45 s. The wafer was soft baked at 110 °C for 5 min. Photoresist was then exposed to ultra violet (UV) light for 15 min using a beam expanded 365 nm UV LED, (M365L2-C1–UV, Thorlabs GmbH, Germany). After UV exposure, the wafer was post-baked for 2 min at 110 °C. The wafer was developed in AZ-726-MIF developer for 5-7 min and then rinsed in water.

The chamber was fabricated by soft-lithography as described previously [67, 68]. In brief, a PDMS mixture (RTV615, Momentive, US) of 10:1 (potting-agent:cross-linking agent) was mixed and degassed by using a mixing machine (Thinky ARE-250, Japan). Next, the PDMS mixture (70 g) was poured over the wafer, degased for 20 min in a desiccator, and cured for 1 h at 80 °C. Following this, PDMS was peeled off the mold and holes were punched for fluidic inlets using a 22-gauge mechanical puncher. The PDMS chamber and a glass slide were exposed to air plasma for 30 s for bonding and were then baked at 80 °C for at least 12 h. The 300 µm wide chamber had a height of 12.87 µm as measured by confocal microscopy.

3.5.2 Supplementary Figures

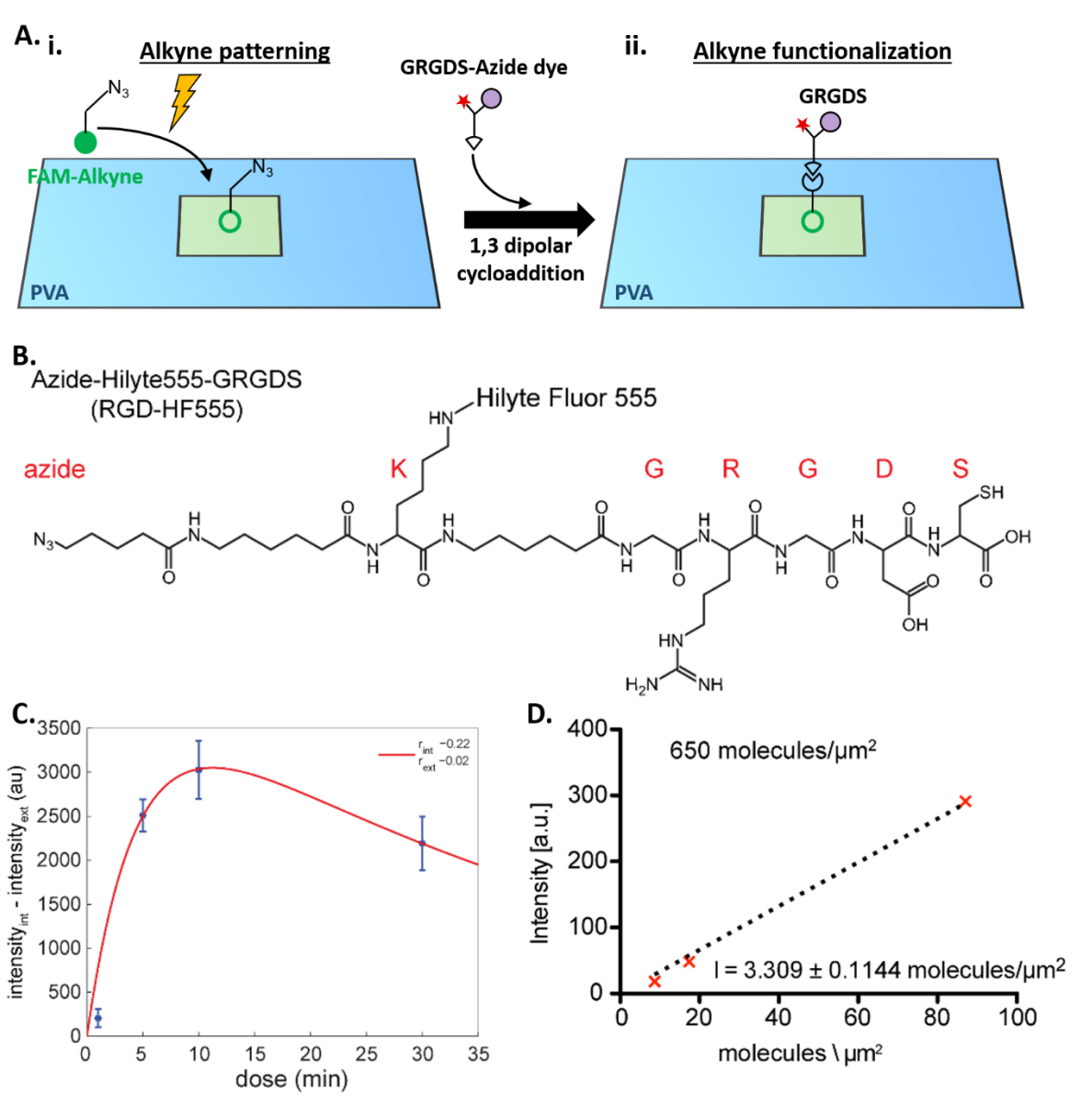

Supplementary Figure 1: Photo-patterning with a controllable LCD panel of a commercially available projector in the lightpath of a microscope.

A) Schematic overview of the patterning process. After photo-bleaching of the 6-FAM-Alkyne-linker onto the PVA passivated surface, the alkyne is used to covalently bind a dye-labeled RGD-Azide to the pattern through a 1,3 dipolar cycloaddition. B) Chemical structure of azide-Hilyte555-GRGDS (RGD-HF555). Amino acids indicated in red as single letter code. C) Functionalization rates within and near the pattern (rint, rext, respectively) are determined by fitting the difference in average internal and external intensity (Intensityint - Intensityext) over increasing exposures using the model, Iim = Ibg + Imx (1-edose*rate), where Iim, Ibg, Imx are the profile image intensity, background image intensity, and maximum achievable fluorescence intensity, respectively. This analysis finds a fitted functionalization rate due to light scatter and LCD dark pixel light leakage just outside of the pattern (rext = -0.02) that is about an order of magnitude slower than that at the pattern center (rext = -0.02). D) Quantification of

RGD-HF555 immobilization efficiency by comparison with a RGD-HF555 fluorescence intensity standard curve. n ≧ 6 images for each condition.

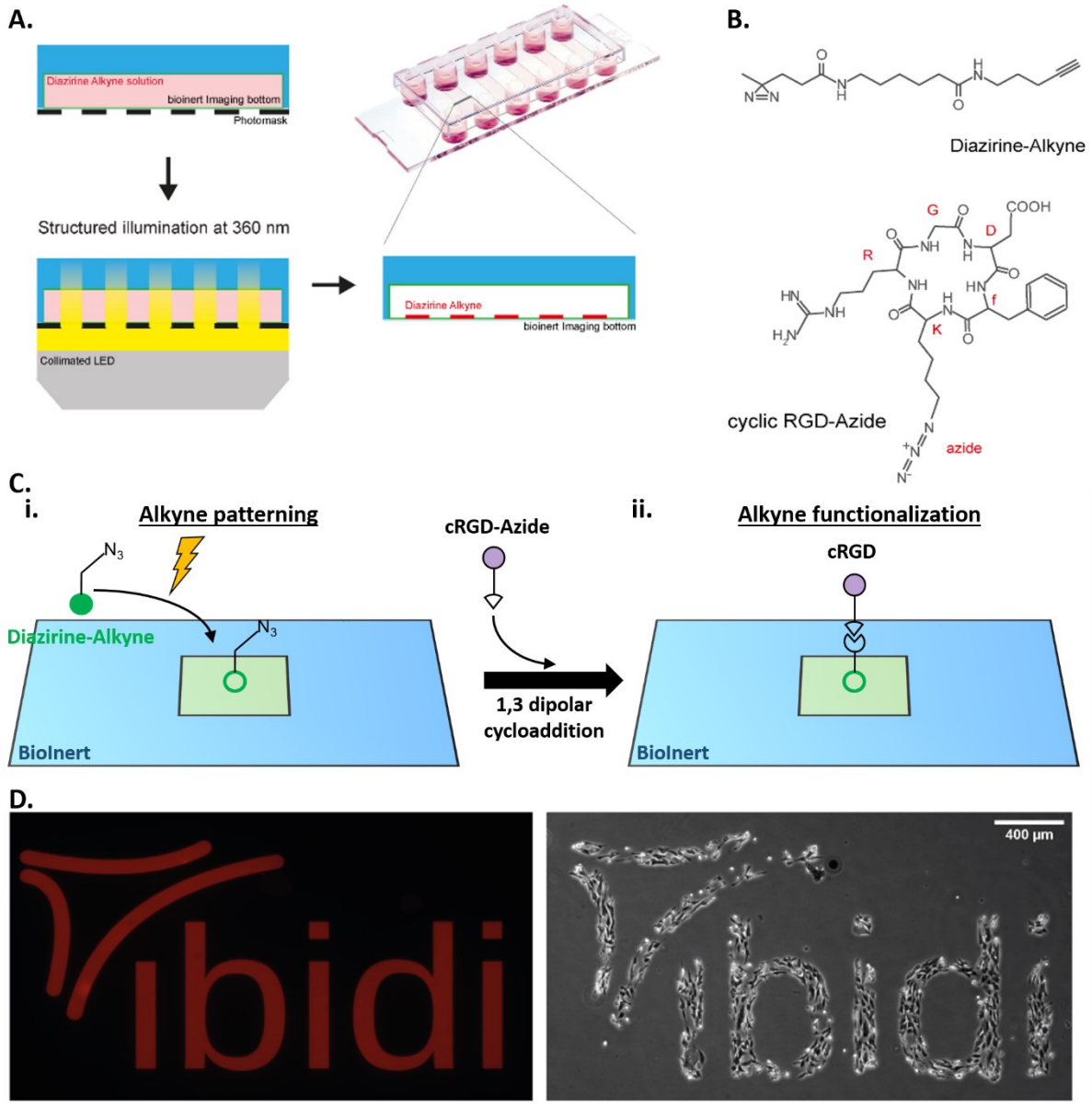

Supplementary Figure 2: Photo-patterning with collimated LED and chromium mask using Diazirine-Alkyne as linker

A) Illumination procedure. DIazirine-Alkyne solution is filled in a Bioinert coated µ-Slide VI channel. The bottom of the slide is covered with a mask containing the desired patterning geometries. Upon illumination with collimated light from a 360 nm LED, light passes through the chromium mask and illuminates only certain areas of the channel. After washing the channel with water, the Diazirine-Alkyne linker is successfully immobilized in the illuminated areas and the slide can be further processed by click chemistry to bind the desired ligand. B) Structure of the Diazirine-Alkyne linker as well as of the

cyclic RGD-Azide used to render the pattern cell adhesive. C) Schematic overview of the patterning process. After photo-immobilization of the Alkyne-linker (i) the alkyne is used to covalently bind a cyclic RGD-Azide to the pattern through a 1,3 dipolar cycloaddition (ii). D) Pattern functionalized with a mixture of sulfo-Cy3-Azide and cRGD-Azide to visualize the pattern as well as to render it cell adhesive. RCC cells on the pattern were imaged 19 days after seeding.

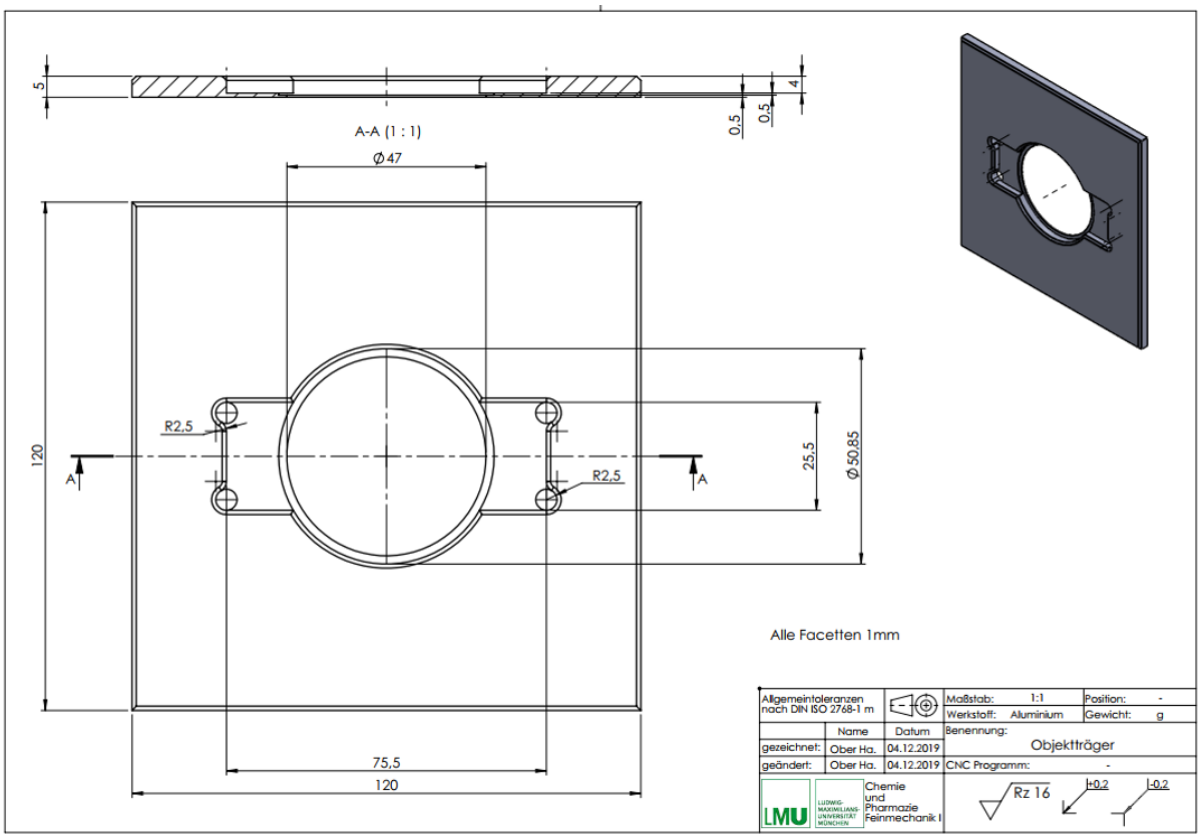

Supplementary Figure 3: Fabrication of aluminum re-aligner

Exact dimensions and detailed visual representation of aluminum re-aligner.

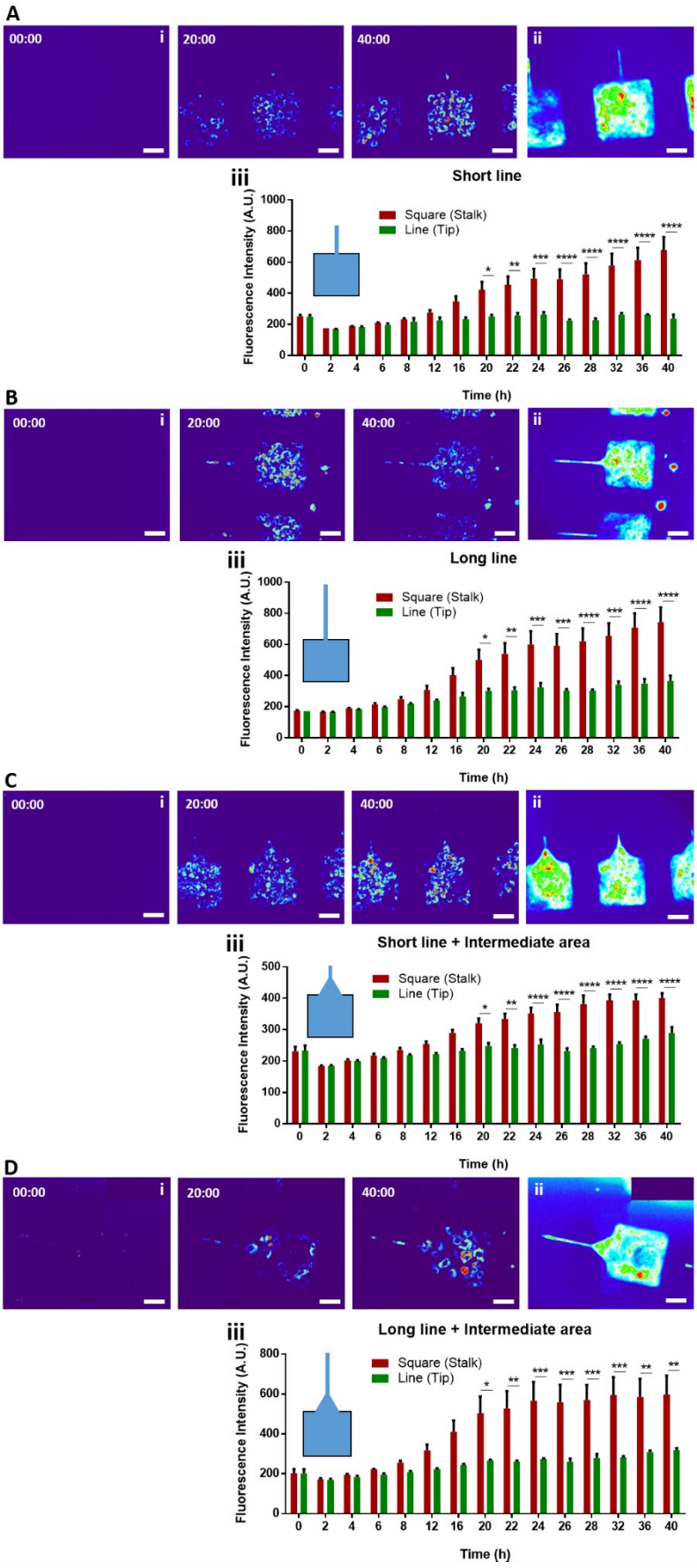
A
00:00
i
20:00
40:00
ii
iii
Short line
Square (Stalk)
Line (Tip)
Fluorescence Intensity (A.U.)
Time (h)
B
00:00
i
20:00
40:00
ii
iii
Long line
Square (Stalk)
Line (Tip)
Fluorescence Intensity (A.U.)
Time (h)
C
00:00
i
20:00
40:00
ii
iii
Short line + Intermediate area
Square (Stalk)
Line (Tip)
Fluorescence Intensity (A.U.)
Time (h)
D
00:00
i
20:00
40:00
ii
iii
Long line + Intermediate area
Square (Stalk)
Line (Tip)
Fluorescence Intensity (A.U.)
Time (h)

Supplementary Figure 4: Fluorescence microscopy images of SmartFlares Hey1 mRNA biosensor-labeled cells, attached to the “static” system and evaluation of the Hey1 mRNA expression over time in the tip/stalk areas

Hey1 mRNA expression in patterns with short line (A), long line (B), short line + intermediate area (C) and long line + intermediate area (D). i) Example heatmaps showing Hey1 mRNA levels, timelapse snapshots at 0, 20h and 40h after addition of the biosensor. ii) Average intensity projection of timelapse. Scale bar: 80 μm iii) Quantitative analysis of Hey1 fluorescence intensity in the square and the line areas. Bars represent the mean+SEM of the fluorescence intensity values, with n=3. Statistical analysis was performed using 2-way ANOVA followed by Sidak's multiple comparisons test; n.s.: non-significant, * $p<0.05$, ** $p<0.01$, *** $p<0.001$, **** $p<0.0001$.

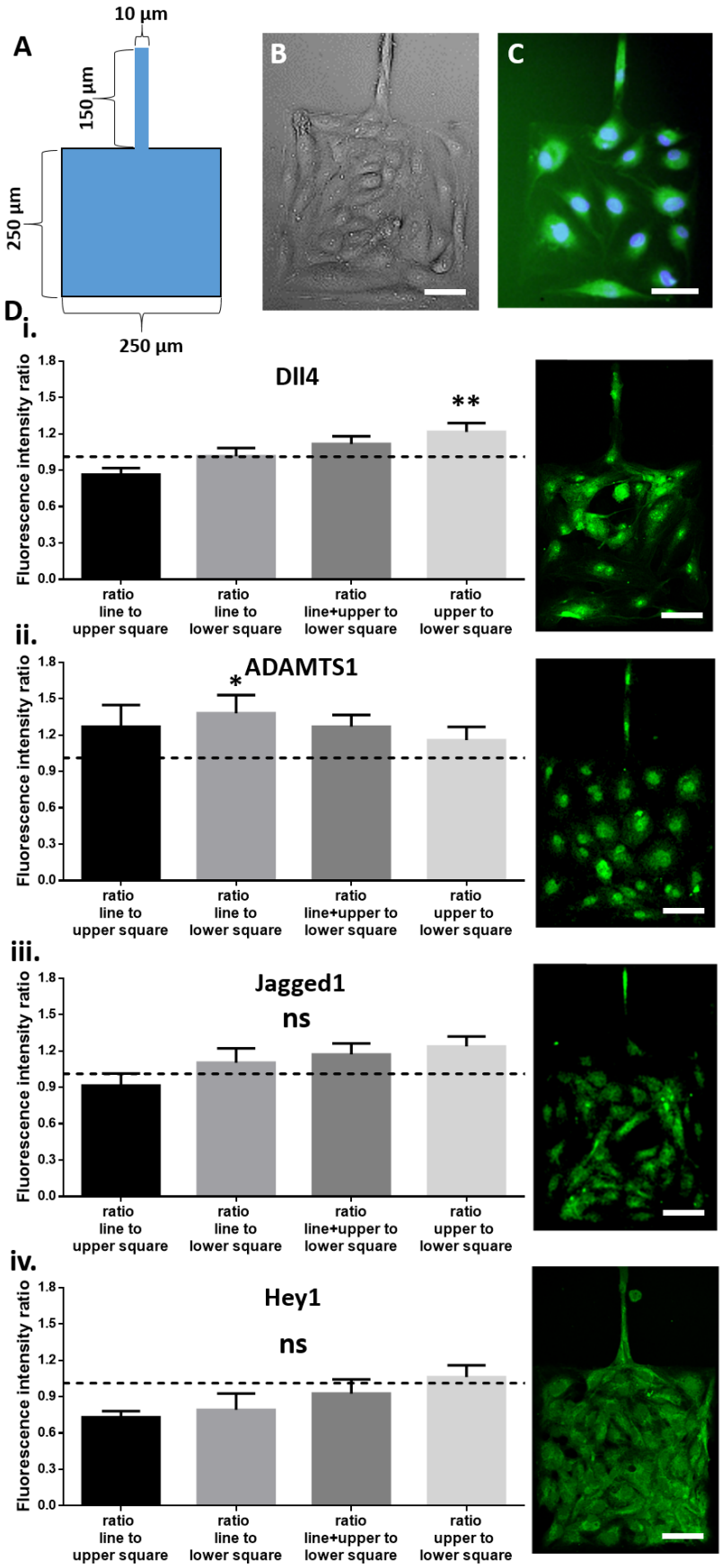
A
10 µm
150 µm
250 µm
250 µm
B
C
D
i.
Dll4
**
Fluorescence intensity ratio
1.8
1.5
1.2
0.9
0.6
0.3
0.0
ratio line to upper square
ratio line to lower square
ratio line+upper to lower square
ratio upper to lower square
ii.
ADAMTS1
*
iii.
Jagged1
ns
iv.
Hey1
ns

Supplementary Figure 5: Cell adhesion on the “static” system created by classic microcontact printing and evaluation of tip/stalk protein marker expression

A) Schematic illustration of the “static” system generated using classic microcontact printing. Example bright-field microscopy image (B) and fluorescence microscopy image (C) of adherent HMECs on the specific square/ line pattern, labeled with 6-FAM dye for the cytosol and Hoechst for the nucleus. D) Left panel: Quantitative analysis of expression of the tip-related markers Dll4 (i), ADAMTS1 (ii) and the stalk-related markers Jagged1 (iii) and Hey1 (iv). Here, for each marker the fluorescence intensity ratios between the different compartments of the patterned area (line, upper square, line+upper square, lower square) were determined. Bars represent the mean ratios of the “static” system +SEM. Statistical significance was assessed using 1-way ANOVA followed by Uncorrected Fisher’s LSD test. i) Dll4: line/upper mean = 0.86, p= 0.10; line/ lower mean = 1.01, p=0.84; line+upper/ lower mean = 1.11, p=0.15; upper/ lower mean = 1.21, p=0.009 (n=20) ii) ADAMTS1: line/upper mean = 1.27, p= 0.12; line/ lower mean = 1.38, p=0.03; line+upper/ lower mean = 1.27, p=0.12; upper/ lower mean = 1.15, p=0.36 (n=9). iii) Jagged1: line/upper mean = 0.91, p=0.49; line/ lower mean = 1.10, p=0.40; line+upper/ lower mean = 1.17, p=0.16; upper/ lower mean =1.23, p=0.059 (n=20). iv) Hey1: line/upper mean = 0.73, p=0.055; line/ lower mean = 0.79, p=0.13; line+upper/ lower mean = 0.92, p=0.58; upper/ lower mean = 1.06, p=0.64 (n=5). n.s.: non-significant, * $p<0.05$, ** $p<0.01$. Right panel: Exemplary fluorescence microscopy images of cells stained for the corresponding marker that is quantified in the left panel. Scale bar: 60 µm.

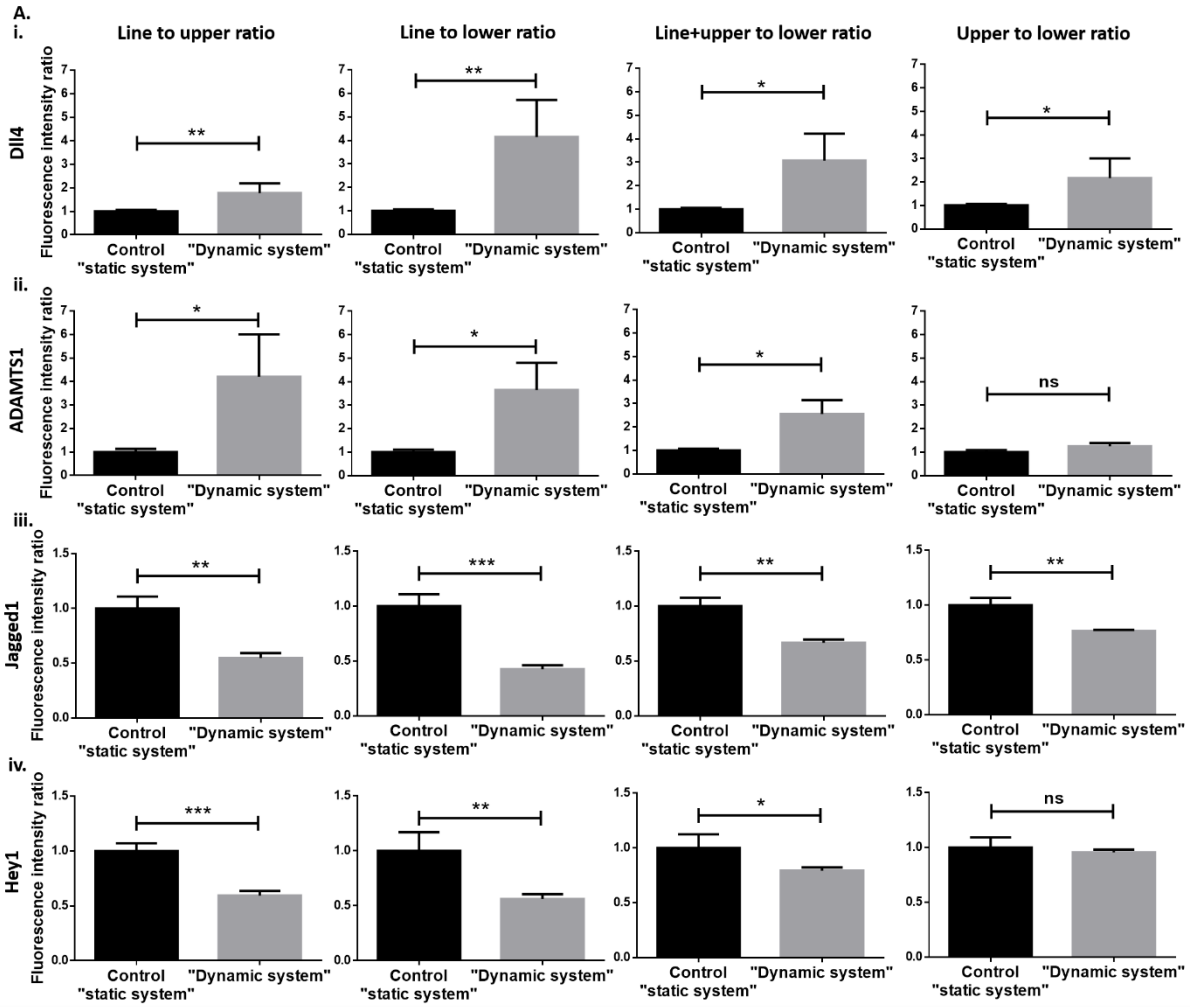

Supplementary Figure 6: Comparison between the control “static“ and “dynamic“ system in tip/stalk marker expression

A) Quantitative analysis of expression of the tip-related markers Dll4 (i), ADAMTS1 (ii) and the stalk-related markers Jagged1 (iii), Hey1 (iv). Here, the fluorescence intensity ratios between the different compartments of the patterned area (line, upper square, line+upper square, lower square) were determined for the “static“ and the “dynamic“ system. The ratios in the control “static“ system were then used for normalization and the direct comparison between the two systems is presented. i) Dll4 “static“ vs “dynamic“: line/upper mean diff= 0,7818 ± 0,2835, p= 0.005; line/lower mean diff= 3,149 ± 1,039, p=0.0053; line+upper/lower mean diff= 2,070 ± 0,7598, p= 0.011; upper/lower mean diff= 1,168 ± 0,5537, p= 0.044 (nstatic=20, ndynamic= 9) ii) ADAMTS1 “static“ vs “dynamic“: line/upper mean diff= 3,196 ± 1,458, p=0.047; line/lower mean diff= 2,652 ± 1,012, p=0.020; line+upper/lower mean diff= 1,555 ± 0,5259, p=0.0104, upper/lower mean diff= 0,2499 ± 0,1638, p=0.149 (nstatic=9, ndynamic= 7). iii) Jagged1 “stati“c vs “dynamic“: line/upper mean diff= 0,4522 ± 0,1522, p=0.0059; line/lower mean diff= 0,5748 ± 0,1483, p=0.0006; line+upper/lower mean diff= 0,3347 ± 0,1065, p=0.0038; upper/lower mean diff= 0,2371 ± 0,07718, p= 0.0042 (nstatic=20, ndynamic= 11). iv) Hey1 “static“ vs “dynamic“: line/upper mean diff= 0,4060 ± 0,08619, p=0.0002; line/lower mean diff= 0,4379 ± 0,1201, p= 0.0017;

line+upper/lower mean diff= 0,2068 ± 0,08549, p=0.0258; upper/lower mean diff=0,04495 ± 0,06700, p= 0.5090 (nstatic=5, ndynamic= 16). Bars represent the mean ratios of the “dynamic” system normalized to the corresponding mean ratios of the control “static” system, +SEM. Statistical significance was assessed using unpaired t-test, *p<0.05, **p<0.01, ***p<0.001, p****<0.0001.

3.6 References

1. Ricoult, S.G., T.E. Kennedy, and D. Juncker, *Substrate-Bound Protein Gradients to Study Haptotaxis.* Frontiers in Bioengineering and Biotechnology, 2015. **3**(40).
2. Segerer, F.J., et al., *Emergence and Persistence of Collective Cell Migration on Small Circular Micropatterns.* Physical Review Letters, 2015. **114**(22): p. 228102.
3. Yoon, S.H., et al., *Passive control of cell locomotion using micropatterns: the effect of micropattern geometry on the migratory behavior of adherent cells.* Lab Chip, 2012. **12**(13): p. 2391-402.
4. Jiang, X., et al., *Directing cell migration with asymmetric micropatterns.* Proc Natl Acad Sci U S A, 2005. **102**(4): p. 975-8.
5. Parker, K.K., et al., *Directional control of lamellipodia extension by constraining cell shape and orienting cell tractional forces.* The FASEB Journal, 2002. **16**(10): p. 1195-1204.
6. Théry, M., et al., *Anisotropy of cell adhesive microenvironment governs cell internal organization and orientation of polarity.* Proceedings of the National Academy of Sciences of the United States of America, 2006. **103**(52): p. 19771-19776.
7. Schiller, H.B. and R. Fässler, *Mechanosensitivity and compositional dynamics of cell-matrix adhesions.* EMBO reports, 2013. **14**(6): p. 509-519.
8. Bélisle, J.M., et al., *Patterning protein concentration using laser-assisted adsorption by photobleaching, LAPAP.* Lab Chip, 2008. **8**(12): p. 2164-7.
9. Gray, D.S., et al., *Engineering amount of cell-cell contact demonstrates biphasic proliferative regulation through RhoA and the actin cytoskeleton.* Exp Cell Res, 2008. **314**(15): p. 2846-54.
10. Brandley, B.K. and R.L. Schnaar, *Cell-Surface Carbohydrates in Cell Recognition and Response.* Journal of Leukocyte Biology, 1986. **40**(1): p. 97-111.
11. Schwarz, J. and M. Sixt, *Chapter Twenty-Four - Quantitative Analysis of Dendritic Cell Haptotaxis*, in *Methods in Enzymology*, T.M. Handel, Editor. 2016, Academic Press. p. 567-581.
12. Wu, J., et al., *Gradient biomaterials and their influences on cell migration.* Interface Focus, 2012. **2**(3): p. 337-355.
13. Azioune, A., et al., *Simple and rapid process for single cell micro-patterning.* Lab on a Chip, 2009. **9**(11): p. 1640-1642.
14. Whitesides, G.M., et al., *Soft lithography in biology and biochemistry.* Annu Rev Biomed Eng, 2001. **3**: p. 335-73.
15. Gegenfurtner, F.A., et al., *Micropatterning as a tool to identify regulatory triggers and kinetics of actin-mediated endothelial mechanosensing.* Journal of Cell Science, 2018. **131**(10): p. jcs212886.
16. Mohammed, D., et al., *Substrate area confinement is a key determinant of cell velocity in collective migration.* Nature Physics, 2019. **15**(8): p. 858-866.
17. Chen, T., et al., *Large-scale curvature sensing by directional actin flow drives cellular migration mode switching.* Nat Phys, 2019. **15**: p. 393-402.
18. Doyle, A.D., *Generation of Micropatterned Substrates Using Micro Photopatterning*, in *European publication server*, I. John Wiley & Sons, Editor. 2001: Hoboken, NJ, USA.
19. Behrndt, M., et al., *Forces driving epithelial spreading in zebrafish gastrulation.* Science, 2012. **338**(6104): p. 257-60.
20. Stirman, J.N., et al., *Real-time multimodal optical control of neurons and muscles in freely behaving Caenorhabditis elegans.* Nature methods, 2011. **8**(2): p. 153-158.
21. Edelstein, A., et al., *Computer control of microscopes using μManager.* Curr Protoc Mol Biol, 2010. **Chapter 14**: p. Unit14.20.
22. Schneider, C.A., W.S. Rasband, and K.W. Eliceiri, *NIH Image to ImageJ: 25 years of image analysis.* Nat Methods, 2012. **9**(7): p. 671-5.

23. Schindelin, J., et al., *Fiji: an open-source platform for biological-image analysis.* Nat Methods, 2012. **9**(7): p. 676-82.
24. Fabrice P. Cordelières. *Manuel tracking image j*. 2005 21 April 2021]; Available from: https://imagej.nih.gov/ij/plugins/manual-tracking.html.
25. Sommer, C., et al. *Ilastik: Interactive learning and segmentation toolkit*. in *2011 IEEE International Symposium on Biomedical Imaging: From Nano to Macro*. 2011.
26. Holden, M.A. and P.S. Cremer, *Light activated patterning of dye-labeled molecules on surfaces.* J Am Chem Soc, 2003. **125**(27): p. 8074-5.
27. Shirai, K., et al., *Graft linker immobilization for spatial control of protein immobilization inside fused microchips.* Electrophoresis, 2009. **30**(24): p. 4251-5.
28. Strale, P.O., et al., *Multiprotein Printing by Light-Induced Molecular Adsorption.* Adv Mater, 2016. **28**(10): p. 2024-9.
29. Martin, T.A., et al., *Quantitative photochemical immobilization of biomolecules on planar and corrugated substrates: a versatile strategy for creating functional biointerfaces.* ACS applied materials & interfaces, 2011. **3**(9): p. 3762-3771.
30. Larsen, E.K.U., M.B.L. Mikkelsen, and N.B. Larsen, *Protein and cell patterning in closed polymer channels by photoimmobilizing proteins on photografted poly(ethylene glycol) diacrylate.* Biomicrofluidics, 2014. **8**(6): p. 064127.
31. Preston, G.W. and A.J. Wilson, *Photo-induced covalent cross-linking for the analysis of biomolecular interactions.* Chemical Society Reviews, 2013. **42**(8): p. 3289-3301.
32. Yamamoto, N., et al., *Mechanism of Carbene Formation from the Excited States of Diazirine and Diazomethane: An MC-SCF Study.* Journal of the American Chemical Society, 1994. **116**(5): p. 2064-2074.
33. Gomes, A.F. and F.C. Gozzo, *Chemical cross-linking with a diazirine photoactivatable cross-linker investigated by MALDI- and ESI-MS/MS.* J Mass Spectrom, 2010. **45**(8): p. 892-9.
34. Rostovtsev, V.V., et al., *A Stepwise Huisgen Cycloaddition Process: Copper(I)-Catalyzed Regioselective "Ligation" of Azides and Terminal Alkynes.* Angewandte Chemie International Edition, 2002. **41**(14): p. 2596-2599.
35. Jewett, J.C. and C.R. Bertozzi, *Cu-free click cycloaddition reactions in chemical biology.* Chemical Society Reviews, 2010. **39**(4): p. 1272-1279.
36. Carrico, I.S., et al., *Lithographic patterning of photoreactive cell-adhesive proteins.* J Am Chem Soc, 2007. **129**(16): p. 4874-5.
37. Larsen, E.K., M.B. Mikkelsen, and N.B. Larsen, *Protein and cell patterning in closed polymer channels by photoimmobilizing proteins on photografted poly(ethylene glycol) diacrylate.* Biomicrofluidics, 2014. **8**(6): p. 064127.
38. Wirkner, M., et al., *Photoactivatable caged cyclic RGD peptide for triggering integrin binding and cell adhesion to surfaces.* Chembiochem, 2011. **12**(17): p. 2623-9.
39. Rosch, J.C., E.K. Hollmann, and E.S. Lippmann, *In vitro selection technologies to enhance biomaterial functionality.* Exp Biol Med (Maywood), 2016. **241**(9): p. 962-71.
40. Bellis, S.L., *Advantages of RGD peptides for directing cell association with biomaterials.* Biomaterials, 2011. **32**(18): p. 4205-10.
41. Hersel, U., C. Dahmen, and H. Kessler, *RGD modified polymers: biomaterials for stimulated cell adhesion and beyond.* Biomaterials, 2003. **24**(24): p. 4385-415.
42. Takada, Y., X. Ye, and S. Simon, *The integrins.* Genome Biology, 2007. **8**(5): p. 215.
43. Ruoslahti, E., *FIBRONECTIN AND ITS RECEPTORS.* Annual Review of Biochemistry, 1988. **57**(1): p. 375-413.
44. Kapp, T.G., et al., *A Comprehensive Evaluation of the Activity and Selectivity Profile of Ligands for RGD-binding Integrins.* Scientific Reports, 2017. **7**(1): p. 39805.
45. Knight, C.G., et al., *The collagen-binding A-domains of integrins alpha(1)beta(1) and alpha(2)beta(1) recognize the same specific amino acid sequence, GFOGER, in native (triple-helical) collagens.* Journal of Biological Chemistry, 2000. **275**(1): p. 35-40.
46. Boateng, S.Y., et al., *RGD and YIGSR synthetic peptides facilitate cellular adhesion identical to that of laminin and fibronectin but alter the physiology of neonatal cardiac myocytes.* American Journal of Physiology-Cell Physiology, 2005. **288**(1): p. C30-C38.
47. Ruoslahti, E., *RGD and other recognition sequences for integrins.* Annu Rev Cell Dev Biol, 1996. **12**: p. 697-715.

48. Mrksich, M. and G.M. Whitesides, *Using self-assembled monolayers to understand the interactions of man-made surfaces with proteins and cells.* Annu Rev Biophys Biomol Struct, 1996. **25**: p. 55-78.
49. Lussi, J.W., et al., *Pattern stability under cell culture conditions—A comparative study of patterning methods based on PLL-g-PEG background passivation.* Biomaterials, 2006. **27**(12): p. 2534-2541.
50. Nelson, C.M., et al., *Degradation of Micropatterned Surfaces by Cell-Dependent and -Independent Processes.* Langmuir, 2003. **19**(5): p. 1493-1499.
51. Sugawara, T. and T. Matsuda, *Photochemical surface derivatization of a peptide containing Arg–Gly–Asp (RGD).* Journal of Biomedical Materials Research, 1995. **29**(9): p. 1047-1052.
52. Doyle, A.D., et al., *One-dimensional topography underlies three-dimensional fibrillar cell migration.* Journal of Cell Biology, 2009. **184**(4): p. 481-490.
53. Weber, M. and M. Sixt, *Live cell imaging of chemotactic dendritic cell migration in explanted mouse ear preparations.* Methods Mol Biol, 2013. **1013**: p. 215-26.
54. Schwarz, J. and M. Sixt, *Quantitative Analysis of Dendritic Cell Haptotaxis.* Methods Enzymol, 2016. **570**: p. 567-81.
55. Middleton, J., et al., *Transcytosis and surface presentation of IL-8 by venular endothelial cells.* Cell, 1997. **91**(3): p. 385-95.
56. Stirman, J.N., et al., *A multispectral optical illumination system with precise spatiotemporal control for the manipulation of optogenetic reagents.* Nature Protocols, 2012. **7**(2): p. 207-220.
57. Wu, Y.I., et al., *A genetically encoded photoactivatable Rac controls the motility of living cells.* Nature, 2009. **461**(7260): p. 104-108.
58. Friedrich, J., et al., *Spheroid-based drug screen: considerations and practical approach.* Nature Protocols, 2009. **4**(3): p. 309-324.
59. Moffat, J.G., J. Rudolph, and D. Bailey, *Phenotypic screening in cancer drug discovery — past, present and future.* Nature Reviews Drug Discovery, 2014. **13**(8): p. 588-602.
60. Schreiber, C., et al., *Ring-Shaped Microlanes and Chemical Barriers as a Platform for Probing Single-Cell Migration.* Scientific Reports, 2016. **6**(1): p. 26858.
61. Murschhauser, A., et al., *A high-throughput microscopy method for single-cell analysis of event-time correlations in nanoparticle-induced cell death.* Communications Biology, 2019. **2**(1): p. 35.
62. Jang, K., et al., *Single-cell attachment and culture method using a photochemical reaction in a closed microfluidic system.* Biomicrofluidics, 2010. **4**(3): p. 032208.
63. Siekmann, A.F., M. Affolter, and H.G. Belting, *The tip cell concept 10 years after: new players tune in for a common theme.* Exp Cell Res, 2013. **319**(9): p. 1255-63.
64. Kurz, H., et al., *First blood vessels in the avian neural tube are formed by a combination of dorsal angioblast immigration and ventral sprouting of endothelial cells.* Dev Biol, 1996. **173**(1): p. 133-47.
65. Mack, J.J. and M.L. Iruela-Arispe, *NOTCH regulation of the endothelial cell phenotype.* Current Opinion in Hematology, 2018. **25**(3).
66. Schuster, S.L., et al., *Contractility as a global regulator of cellular morphology, velocity, and directionality in low-adhesive fibrillary micro-environments.* Biomaterials, 2016. **102**: p. 137-47.
67. Mehling, M., et al., *Real-time tracking, retrieval and gene expression analysis of migrating human T cells.* Lab on a Chip, 2015. **15**(5): p. 1276-1283.
68. Kellogg, R.A., et al., *High-throughput microfluidic single-cell analysis pipeline for studies of signaling dynamics.* Nat Protoc, 2014. **9**(7): p. 1713-26.

CHAPTER 4

4. General Conclusion

Application of surface engineering methods in the field of *in vitro* biology has revolutionized our understanding of how cells interact with their environment. Spatially controlling surface properties such as roughness and wettability and introducing defined micro- or nanoscale textures such as grooves, ridges, pores, pits, etc (topographical patterning) can strongly affect cell adhesion, spreading, proliferation and survival in cell culture. Moreover, chemical patterning of surfaces (often in an ECM-mimicking fashion) allows spatially-controlled cell adhesion, at any wished geometry which is also pivotal in studying cell-matrix and cell-cell interactions and the mechanics of cell adhesion and movement.

In the first part of this study, we implemented standard microcontact printing methods followed by click-chemistry reactions to generate circular isles of cells that are later allowed to spread out. This way, we were able to study the collective migratory behaviour of urothelial bladder carcinoma T24 cells in normal conditions and upon blocking their intercellular contacts. E- and N-Cadherins are central components of cell-cell adhesions, which play a critical role in cell migration during cancer metastasis. However, their distinct contribution to collective cell migration remains poorly understood, and quantitative frameworks to rigorously determine their impact on migration are currently lacking. Here, we combine the above-mentioned *in vitro* approach to investigate collective spreading of cell clusters with quantitative biophysical predictions to show that disrupting Cadherin junctions has an unexpected, non-trivial effect on the repulsive excluded volume interactions of cells.

First, we show that disruption of either E- or N-Cadherin junctions in urothelial bladder carcinoma T24 colonies reduces their spreading efficiency while, surprisingly, the correlations in the velocity fields of the cell sheet remain unaffected. To elucidate these findings, we develop a biophysical simulation model for collective cell migration that includes persistent

single-cell migration, cell proliferation, and cell-cell interactions. By systematically varying the types of cell-cell interactions included, we show that blocking either of the Cadherins has an effect akin to reducing repulsive excluded volume interactions in the model. In contrast, polarity interactions such as contact inhibition of locomotion, which control the velocity correlations, remain unaffected. Conceptually, our findings indicate that E- and N-Cadherins promote cell-cell repulsion by sharpening cellular boundaries. Our results thus identify cell-cell repulsion as a decisive control parameter of collective cell migration.

This study provides a novel perspective on the role of cell-cell adhesions in collective migration, based on rigorous quantitative data analysis combined with biophysical modelling. We here report a surprising observation: Although intercellular adhesion intuitively implies cell-cell cohesion, we show that it rather promotes repulsive excluded volume-like interactions for the migratory dynamics of cells, increasing the efficiency of collective cell spreading. These findings may have physiological relevance in cell spreading and cell invasion phenomena in cancer metastasis, where intercellular contacts based on different Cadherin types are potential pharmacological targets. Our study has the potential to provide a paradigm for future research aiming to elucidate the role of different cellular components or the effects of different pharmacological agents on the dynamics of cancer cell migration.

In the second part of this study, a novel building block-based photopatterning technique is introduced. Using a light- dose dependent first patterning step, which is feasible on arbitrary surfaces, highly sustainable and precise patterns are generated in high-throughput. In a subsequent functionalization step, click chemistry is used to covalently bind biologically relevant adhesion molecules to the pattern. This method is further adapted by addition of a second pattering step, allowing spatiotemporal control over two distinct surface patterns. As proof of principle, we apply this “sequential photopatterning”, to study the well-known dynamic process of tip/stalk endothelial cell phenotype switch during angiogenesis.

Spatially controlled ‘’printing’’ of adhesion ligands on cell culture surfaces, also known as micropatterning, became vital in all research fields implementing cultured cells. Stability, precision, specificity, spatiotemporal control and high-throughput outcome are highly desired properties in surface engineering but achieving their combination is a challenge. Although microcontact printing has provided a spatiotemporally controllable setup for studying dynamic cell processes, it has important limitations such as the requirement of bulky macromolecules (i.e. Extracellular Matrix proteins) leading to non-specific interactions and reduced stability over time. Therefore, we establish a covalent single photopatterning technique that provides high stability and versatility as it can be used with a variety of different illumination setups and photo-chemistries tailored to the specific biological set-up needed. We assess the specificity and efficacy of our photopatterning system by generating concentration gradients to investigate haptotactic cell migration using different cell lines. In order to be able to ‘’switch on’’ distinct areas at any selected timepoint, we include another photopatterning step and confirm the efficacy of this sequential photopatterning setup in inducing a tip/stalk phenotype switch in migrating endothelial cells.

The photopatterning technique introduced in this study is highly adaptable to serve different experimental purposes. Moreover, although challenging, the acquisition of spatiotemporal control is a key factor in studying dynamic processes. Thus, our advanced setup can be used in a broad spectrum of research applications and prove to be an important surface engineering paradigm for future studies.

To conclude, this thesis as a whole provides two novel paradigms of surface patterning for studying various aspects of cell behaviour in different cell types. Our combined experimental and quantitative theoretical findings challenge the conventional idea that cell-cell adhesions always enhance cohesion in a migrating colony. Moreover, the innovative character and confirmed efficacy of our sequential photopatterning process, allowing spatiotemporal control over the cell behaviour, makes this setup a highly reliable choice for a large scope of future *in vitro* applications.

5. APPENDIX

5.1 List of publications

First authorship publications:

1) E- and N-Cadherin-mediated intercellular contacts enhance collective spreading of migrating cancer cells. **Zisis T**., David B. Brückner, Tom Brandstätter, Joseph d'Alessandro, Angelika Vollmar, Chase P. Broedersz, Stefan Zahler., *Biophysical Journal*, 2022

2) Sequential and switchable patterning for studying cellular processes under spatiotemporal control. **Zisis T**., Schwarz J., Kretschmer M., Balles M., Nemethova M., Chait R., Hauschild R., Lange J., Guet C., Joachim Rädler, Sixt M., Zahler S., *ACS applied materials & interfaces*, 2021

3) Interfacial activation of Candida antarctica lipase B: combined evidence from experiment and simulation. **Zisis T**, Freddolino PL, Turunen P, van Teeseling MC, Rowan AE, Blank KG., *Biochemistry*, 2015

4) (In preparation) Cytoskeleton-mimicing Polyisocyanide hydrogel droplets: Permanent network deformation linked to critical stress. **Zisis T.**, Hammink R., Chokkalingam V., Nijemeisland M., Blank KG, Wilhelm T. S. Huck, Rowan AE

Co-authorship publications:

1) Tetrapyrrolic pigments from heme- and chlorophyll breakdown are actin-targeting compounds. Karg C., Wang S., Al Danaf N., Pemberton R., Bernard D., Kretschmer M., Schneider S., **Zisis T.**, Vollmar A., Lamb D., Zahler S., Moser S., *Cell Chemical Biology*, 2021

2) Gene editing and synthetically accessible inhibitors reveal role for TPC2 in HCC cell proliferation and tumor growth. Müller M, Gerndt S, Chao YK, **Zisis T**, OngNam Phuong Nguyen1, Aaron Gerwien4, Urban N, Müller C, Gegenfurtner F, Geisslinger F, Ortler C, Zahler S, Biel M, Schäfer M, Grimm C, Bracher F, Vollmar AM, Bartel K., *Cell Chemical Biology*, 2021

3) Targeting actin inhibits repair of doxorubicin-induced DNA damage: a novel therapeutic approach for combination therapy. Pfitzer L, Moser C, Gegenfurtner F, Arner A, Foerster F, Atzberger C, **Zisis T**, Kubisch-Dohmen R, Busse J, Smith R, Timinszky G, Kalinina OV, Müller R, Wagner E, Vollmar AM, Zahler S., *Cell Death Dis.*, 2019

4) Targeting the endoplasmic reticulum-mitochondria interface sensitizes leukemia cells to cytostatics, Koczian F, Nagło O, Vomacka J, Vick B, Servatius P, **Zisis T**, Hettich B, Kazmaier U, Sieber SA, Jeremias I, Zahler S, Braig S., *Haematologica*, 2019

5) Transcriptional effects of actin-binding compounds: the cytoplasm sets the tone. Gegenfurtner FA, **Zisis T**, Al Danaf N, Schrimpf W, Kliesmete Z, Ziegenhain C, Enard W, Kazmaier U, Lamb DC, Vollmar AM, Zahler S., *Cell Mol Life Sci*., 2018

6) Affinity-Based Purification of Polyisocyanopeptide Bioconjugates. Hammink R, Eggermont LJ, **Zisis T**, Tel J, Figdor CG, Rowan AE, Blank KG., *Bioconjug Chem*., 2017

5.2 List of presentations

25-27.02.2019: Successful proposal submission and reviewer committee defense for 4-year extension funding in SFB1032, Munich, Germany (oral presentation)

2011-2014: Dutch Meeting for Molecular and Cellular Biophysics, Veldhoven, The Netherlands (poster presentations)

2011-2014: NWO study group meeting “Biomolecular Chemistry”, Lunteren, The Netherlands (poster presentations)

5.3 Funding

The study presented in CHAPTER 2 was funded by the Deutsche Forschungsgemeinschaft (DFG, German Research Foundation) - Project-ID 201269156 - SFB 1032 (Projects B8 and B12). D.B.B. is a NOMIS Fellow supported by the NOMIS Foundation and was supported in part by a DFG fellowship within the Graduate School of Quantitative Biosciences Munich (QBM) and by the Joachim Herz Stiftung.

The study presented in CHAPTER 3 was funded by the Deutsche Forschungsgemeinschaft (DFG, German Research Foundation) - Project-ID 201269156 - SFB 1032 (Projects B8 and B12). This work was also supported by the Boehringer Ingelheim Fonds and the European Research Council (ERC CoG 724373) and ibidi GmbH.

5.4 Acknowledgements

First of all, I want to thank Prof. Dr. Stefan Zahler and Prof. Dr. Angelika Vollmar for the opportunity to write and defend my dissertation at the Chair of Pharmaceutical Biology. Their proficient and inspiring supervision empowered me to transform interesting scientific ideas into well-thought experiments and meaningful results.

My sincere thanks go also to the examination board members, Prof. Dr. Stefan Zahler, Prof. Dr. Angelika Vollmar, Prof. Dr. Olivia Merkel, Prof. Dr. Franz Paintner, PD Dr. Stylianos Michalakis and Prof. Dr. Susanne Koch for their willingness to evaluate my work and their valuable time.

I would further like to thank Prof. Dr. Joachim Rädler for the conception and organisational management of the SFB 1032 Nanoagents.

I would like to sincerely thank my colleagues Maibritt Kretschmer and Lucas Siow for their motivated participation and the outstanding work carried out within the framework of my dissertation. I also want to thank my collaborators from ibidi, Miriam Balles and Jan Schwarz for their significant contribution to the project in Chapter 3. Of course, many thanks to Jana Peliskova for all the technical support in my projects.

A big thank you goes to the entire working group of Prof. Zahler for making my days of working in Grosshadern very enjoyable. In this context I would like to especially thank my lab mates and neighbours Lucas, Ling, Mehak, Yudong and Pengyu as well as Lisa, Florian and Daniel for the friendship that goes beyond the lab and the great memories we now share.

Furthermore, I want to give a huge thank you to my parents for their constant support and guidance in all aspects of my life and for their confidence in me. I wouldn’t be the person I am today without you.

Επίσης, ευχαριστώ πολύ γιαγιά και παππού! Εχετε κι εσείς με τον τρόπο σας συνδράμει σε αυτό το διδακτορικό!

Last but not least, I want to thank my life partner Dr. Alexandra Chovsepian, aka the Armenian master of disaster. You are the gentlest and hardest working person I know. Together we have embarked on a long journey that still continues today and I am looking forward to everything that comes next. Thank you for always being there for me, helping and supporting me and for making each and every day beautiful.